POLITECNICO DI MILANO
School of Industrial and Information Engineering
Master of Science in Materials Engineering and Nanotechnology

PULSED LASER DEPOSITION AND SCANNING TUNNELING MICROSCOPY OF ZnO/MoS_2 TWO-DIMENSIONAL STRUCTURES AND HETEROSTRUCTURES

Supervisor:
Prof. Andrea Li Bassi

Co-supervisor:
Dr. Francesco Tumino

Graduation thesis of:
Alessia Rubino
875240

Academic year 2017 - 2018

Abstract

Two-dimensional (2D) semiconductors are materials of increasing scientific interest as they may exhibit completely different structures and properties with respect to their bulk counterparts and as they could be promisingly exploited for future applications in the field of nanotechnology. This thesis describes an experimental investigation of heterostructures consisting of molybdenum disulphide (MoS_2) and zinc oxide (ZnO) produced onto a metallic Au(111) substrate and of 2D MoS_2 nanostructures composed by one or few atomic layers and supported by an Ag(111) substrate. The production of these 2D structures has been achieved by means of pulsed laser deposition (PLD), while scanning tunneling microscopy (STM) and spectroscopy (STS) have been employed in order to characterize *in situ* their structural, morphological and electronic properties at the nanometer and atomic scale. This work also reports a preliminary experimental activity aimed at exploiting PLD to grow silicon at the two-dimensional limit and at investigating the obtained structures using a scanning tunneling microscope.

Sommario

Grande interesse è dedicato, oggigiorno, alle nanostrutture bidimensionali (2D) prodotte tramite il confinamento di materiali semiconduttori lungo una delle tre dimensioni dello spazio. Queste strutture 2D sono oggetto di molte attività di ricerca (teorica e sperimentale) per il fatto che possono essere caratterizzate da strutture e proprietà completamente diverse da quelle mostrate nella loro forma bulk e dal momento che il loro utilizzo in applicazioni future (per esempio, nel campo delle nanotecnologie) sembra molto promettente. Il lavoro di tesi riporta l'analisi sperimentale di eterostrutture di disolfuro di molibdeno (MoS_2) e ossido di zinco (ZnO) supportate da una superficie di Au(111) e lo studio di nanostrutture 2D di MoS_2 formate da uno o qualche strato atomico e realizzate su un substrato di Ag(111). Queste strutture bidimensionali sono state prodotte tramite una tecnica nota come Deposizione a Laser Pulsato (PLD, *Pulsed Laser Deposition*) e, successivamente, le tecniche di microscopia a effetto tunnel (STM, *Scanning Tunneling Microscopy*) e spettroscopia a effetto tunnel (STS, *Scanning Tunneling Spectroscopy*) sono state utilizzate per lo studio delle proprietà strutturali, morfologiche ed elettroniche dei materiali depositati. Questo lavoro di tesi riporta anche un'attività di ricerca preliminare che è stata condotta con lo scopo di utilizzare la tecnica PLD per crescere strutture bidimensionali di silicio – silicene – e di studiare poi le nanostrutture ottenute con un microscopio a effetto tunnel.

Estratto

I materiali bidimensionali (2D) hanno iniziato ad attrarre un grande interesse scientifico a partire dal 2004, anno in cui le proprietà del grafene – un materiale bidimensionale costituito da un reticolo esagonale di atomi di carbonio ibridizzati sp^2 – sono state scoperte e studiate. Infatti, il confinamento di un materiale lungo una delle tre dimensioni dello spazio può portare alla luce strutture e proprietà (elettroniche, ottiche, magnetiche, meccaniche, ecc.) diverse da quelle tipiche dello stesso materiale nella sua forma bulk (3D) e che possono essere sfruttate per nuove applicazioni (come, per esempio, nel campo dell'elettronica e della catalisi) o per il miglioramento di dispositivi già esistenti, come nel caso dei transistor a effetto di campo (FET, *Field Effect Transistors)* e dei pannelli fotovoltaici.
Per la realizzazione di dispositivi nuovi o più efficienti, i materiali 2D sono quindi molto promettenti e, in particolare, grande attenzione è oggigiorno dedicata alla produzione di nanostrutture bidimensionali e film ultrasottili di materiali semiconduttori dal momento che, per molte applicazioni, la presenza di un gap energetico tra la banda di valenza e la banda di conduzione – assente nel caso del grafene, caratterizzato da un comportamento semimetallico – rappresenta un requisito fondamentale per il materiale impiegato. Crescente impegno è stato quindi dedicato alla ricerca e all'utilizzo di nuovi materiali 2D come, per esempio, il disolfuro di molibdeno (MoS_2) bidimensionale, il nitruro di boro esagonale (h-BN) e il silicene – un allotropo del silicio caratterizzato da una struttura di tipo grafenico e da un'ibridizzazione sp^2 degli atomi.
Il presente lavoro di tesi si inserisce, quindi, nell'ambito della ricerca volto alla produzione, alla caratterizzazione e, infine, all'applicazione di materiali ed eterostrutture bidimensionali di tipo semiconduttivo. In particolare, l'approccio utilizzato durante questa attività sperimentale si basa sull'utilizzo di una tecnica di deposizione molto versatile nota come Deposizione a Laser Pulsato (PLD, *Pulsed Laser Deposition*) e sulla caratterizzazione *in situ* – ossia, in condizioni di ultra-alto vuoto (con pressione di base $<10^{-9}$ mbar) – delle strutture 2D prodotte, tramite l'utilizzo di un microscopio a effetto tunnel, che permette di studiare le proprietà strutturali, morfologiche ed elettroniche di un materiale o una superficie, garantendo una risoluzione spaziale molto elevata (fino alla scala nanometrica ed atomica). Nell'ambito dell'attività di ricerca riportata in questa tesi, la tecnica PLD è stata selezionata come metodo di fabbricazione dei materiali 2D di interesse per la sua versatilità e per i numerosi vantaggi che offre. Infatti, la deposizione a laser pulsato permette di depositare qualsiasi tipo di materiale mantenendone la stechiometria e garantendo una deposizione uniforme in termini di struttura, morfologia, spessore e, quindi, proprietà su aree estese del substrato (con dimensioni dell'ordine del cm^2).
La prima parte di questo lavoro di tesi è stata dedicata alla produzione di eterostrutture di disolfuro di molibdeno (MoS_2) e ossido di zinco (ZnO), depositati su un substrato di Au(111) tramite la tecnica PLD. Due diverse strategie sperimentali sono state utilizzate, la prima basata sulla deposizione di ZnO seguita dalla crescita di MoS_2 sullo stesso substrato di oro e la seconda basata su una procedura opposta – crescita di MoS_2 e successiva deposizione di ZnO sulla stessa superficie di Au(111). Eterostrutture di ZnO e MoS_2 sono state ottenute con entrambi gli approcci, anche se il secondo si è dimostrato più promettente e ha portato alla realizzazione di eterostrutture laterali dei due materiali, le cui proprietà morfologiche ed elettroniche sono state studiate, rispettivamente, tramite microscopia a effetto tunnel (STM*, Scanning Tunneling Microscopy*) e spettroscopia a effetto tunnel (STS, *Scanning Tunneling Spectroscopy*). In particolare, le misure STS hanno messo in luce come le proprietà elettroniche dei due materiali depositati vengano influenzate in modo rilevante dalla presenza del substrato metallico che causa una loro leggera metallizzazione e induce un comportamento tipico di un semiconduttore di tipo n.
La seconda parte dell'attività sperimentale ha avuto, come obiettivo principale, la sintesi e la caratterizzazione di nanostrutture bidimensionali di MoS_2 supportate da un substrato di Ag(111), con lo

scopo finale di fare un confronto tra il sistema MoS_2/Ag(111) e il sistema MoS_2/Au(111) (precedentemente studiato in questo laboratorio) in termini di struttura, morfologia e proprietà elettroniche, vibrazionali e ottiche. In particolare, la tecnica PLD è stata utilizzata per realizzare tre campioni di MoS_2 su argento con diversa quantità di materiale depositato e, quindi, diverso ricoprimento, ossia la frazione della superficie del substrato coperta dalle strutture di disolfuro di molibdeno prodotte. La struttura e la morfologia superficiale dei tre campioni sono state poi studiate utilizzando un microscopio a effetto tunnel e ha rivelato la formazione di isole ordinate di MoS_2, caratterizzate da uno spessore di circa 2 Å e dalla presenza di una particolare superstruttura superficiale nota come pattern di Moirè. Le proprietà elettroniche del sistema MoS_2/Ag(111) sono poi state studiate tramite misure di spettroscopia a effetto tunnel che hanno confermato il carattere semiconduttivo del MoS_2 bidimensionale, caratterizzato da un gap energetico di circa 2 eV. In realtà, le proprietà elettroniche del materiale depositato sono influenzate dalla presenza del substrato metallico che provoca una leggera metallizzazione e un comportamento da semiconduttore di tipo n nel disolfuro di molibdeno. Infine, un'ulteriore caratterizzazione delle proprietà del materiale è stata condotta *ex situ* tramite spettroscopia Raman e misure di fotoluminescenza, che hanno evidenziato come anche le proprietà vibrazionali e ottiche del materiale depositato vengano modificate dalla presenza del substrato che può, per esempio, indurre deformazioni o un certo trasferimento di carica all'interfaccia.

L'ultima parte dell'attività sperimentale riportata in questo lavoro di tesi è stata dedicata a una ricerca di tipo preliminare volta a depositare silicio bidimensionale – noto come silicene – usando la tecnica PLD, un processo di deposizione inusuale per la crescita del silicene, che viene tipicamente sintetizzato tramite deposizione da vapore chimica (CVD, *Chemical Vapour Deposition)* oppure tramite crescita epitassiale (MBE, *Molecular Beam Epitaxy*). In particolare, diverse deposizioni sono state effettuate sia su substrati di Ag(111) sia su superfici di Au(111) e alcuni parametri di processo (come il numero di impulsi laser, la pressione dell'atmosfera presente nella camera di deposizione durante il processo PLD e la temperatura del trattamento termico post-deposizione) sono stati variati per capire il modo in cui essi influenzano la struttura e la morfologia del materiale depositato. Sebbene la crescita di strutture ordinate di silicio non sia stata osservata, gli esperimenti condotti hanno permesso di concludere quali siano i parametri di processo più promettenti per la produzione di silicene tramite la tecnica PLD.

Contents

Abstract I

Sommario III

Estratto V

List of Figures IX

List of Tables XI

Introduction XIII

1 Two-dimensional semiconducting materials 1
1.1 Two-dimensional (2D) materials beyond graphene 1
1.2 Synthesis of two-dimensional (2D) materials 5
1.2.1 Two-dimensional molybdenum disulphide by pulsed laser deposition 6
1.2.2 Two-dimensional zinc oxide by pulsed laser deposition 9
1.3 Characterization techniques 11
1.3.1 MoS_2 on Au(111): characterization by means of scanning tunneling microscopy (STM) and spectroscopy (STS) 11
1.3.2 ZnO on Au(111): scanning tunneling microscopy (STM) and spectroscopy (STS) characterization 16
1.4 Pulsed laser deposition (PLD) combined with scanning tunneling microscopy (STM) and spectroscopy (STS): synthesis and characterization of MoS_2 and ZnO on Au(111) 21
1.4.1 2D MoS_2 growth by pulsed laser deposition and its STM/STS characterization 21
1.4.2 2D ZnO grown by pulsed laser deposition and characterized by STM and STS 24
1.5 Objectives of this work 26

2 Experimental methods 29
2.1 Pulsed laser deposition (PLD) 29
2.2 Scanning tunneling microscopy (STM) and scanning tunneling spectroscopy (STS) 32
2.2.1 Working principle and theoretical concepts 33
2.2.2 Scanning tunneling spectroscopy (STS) 39
2.3 Other characterization techniques 42

3 Experimental results 49
3.1 Zinc oxide, molybdenum disulphide and their heterostructures on Au(111) 49
3.1.1 Molybdenum disulphide (MoS_2) and zinc oxide (ZnO) on Au(111) 50
3.1.2 ZnO/MoS_2 heterostructures on Au(111) – first deposition strategy (ZnO deposition followed by MoS_2 growth) 55
3.1.3 ZnO/MoS_2 heterostructures on Au(111) – second deposition strategy (MoS_2 deposition followed by ZnO growth) 59
3.2 Two-dimensional molybdenum disulphide nanostructures on Ag(111) 63
3.2.1 Morphological characterization of MoS_2 nanostructures 64

3.2.2 Electronic properties of MoS_2 nanostructures on Ag(111) 71
3.2.3 Auger electron spectroscopy, Raman spectroscopy and photoluminescence (PL) measurements 74
3.3 Pulsed laser deposition and STM characterization of silicon on Ag(111) and Au(111) 78

4 Conclusions and perspectives 87

Bibliography 91

List of Figures

1.1 Structure and band diagram of bulk and monolayer MoS_2. From [3] 2
1.2 Structure of bulk and graphene-like ZnO. From [11] 2
1.3 Thickness-dependence of the electronic band structure of ZnO. From [12] 3
1.4 Silicene phases on Ag(111). From [5] 4
1.5 Van der Waals and lateral heterostructures. From [21] 5
1.6 Schematic representation of the PLD apparatus. From [22] 6
1.7 Raman spectra of monolayer and bilayer MoS_2 on different insulating substrates. From [25] 7
1.8 AFM thickness profiles of monolayer, bilayer and trilayer MoS_2 on sapphire(0001). From [26] 7
1.9 TEM images and Raman spectra of MoS_2 thin films on different substrates. From [27] 8
1.10 TEM image of MoS_2 on Ag(111). From [29] 9
1.11 AFM images of ZnO films grown at different oxygen pressures. From [31] 10
1.12 STM image of ZnO on Ag(111). From [33] 10
1.13 STM images and schematic model of MoS_2 on Au(111). From [34] 12
1.14 STM images and model of the MoS_2 moiré superstructure on Au(111). From [30] 13
1.15 STS spectrum acquired on the MoS_2/Au(111) system. From [30] 14
1.16 STM images of different MoS_2/Au(111) systems featuring an increasing coverage. From [38] 15
1.17 STM image of monolayer and bilayer MoS_2 on Au(111). From [38] 15
1.18 STM image of MoS_2 on Au(111). STM image and schematic model of a MoS_2 line defect. From [38] 16
1.19 STM images of ZnO on Au(111). From [41] 17
1.20 STS spectrum of the ZnO/Au(111) system. From [41] 18
1.21 STM images of ZnO on Au(111). From [42] 18
1.22 STM images of different ZnO/Au(111) systems obtained by gradually increasing the annealing time. From [42] 19
1.23 Modification of the ZnO lattice constant and moiré periodicity as a function of the number of ZnO layers. STS spectra acquired on Au(111) and on different ZnO layers. From [43] 20
1.24 STM image and dI/dV maps acquired on a ZnO/Au(111) system. From [43] 21
1.25 STM images of MoS_2 on Au(111). From [44] 22
1.26 STM images of triangular MoS_2 islands on Au(111). From [44] 23
1.27 STM images of a continuous film of monolayer MoS_2 on Au(111). From [44] 24
1.28 STS spectrum of single-layer MoS_2 on Au(111). From [44] 24
1.29 STM images of different ZnO/Au(111) systems featuring an increasing coverage. From [45] 25
1.30 STS spectra of different ZnO layers on Au(111). From [45] 26

2.1 Scheme of the PLD apparatus. From [46] 30
2.2 Schematic representation of the plasma plume expansion mechanism. From [46] 31
2.3 Schematic representation of a scanning tunneling microscope. From [48] 33
2.4 Finite potential step and finite rectangular barrier. From [48] 35
2.5 Energy diagram of a trapezoidal potential barrier 35
2.6 Schematic representation of the Bardeen's approach. From [51] 36
2.7 Schematic representation of the energy levels involved in tunneling as a function of the applied voltage sign. From [48] 39
2.8 Schematic representation of the lock-in amplifier working principle. From [48] 40

2.9 Schematic representations of an Auger process and an Auger spectrum. From [55] 43
2.10 Schematic representation of the Stokes and anti-Stokes processes. From [55] 45
2.11 Schematic representation of Raman spectroscopic measurements. From [55] 46
2.12 Schematic representation of the photoluminescence (PL) mechanism. From [56] 47
2.13 Schematic representation of a PL system. From [56] 48

3.1 MoS_2/Au(111) – Large scale STM images and line profile 51
3.2 ZnO/Au(111) – Large scale STM images and line profile 52
3.3 ZnO/Au(111) – Distortion of the Au(111) herringbone reconstruction 53
3.4 ZnO/Au(111) – Dishomogeneity of the ZnO coverage and morphology on the gold surface 53
3.5 MoS_2/Au(111) – Large scale and atomic-resolution STM images after annealing in O_2 54
3.6 ZnO/MoS_2 heterostructures on Au(111) – Large scale STM images and line profile 55
3.7 ZnO/MoS_2 heterostructures on Au(111) – Distortion of the Au(111) herringbone reconstruction . 56
3.8 ZnO/MoS_2 heterostructures on Au(111) – High-magnification STM images and line profile 57
3.9 ZnO/MoS_2 heterostructures on Au(111) – STS spectra 58
3.10 ZnO/MoS_2 heterostructures on Au(111) – Large scale STM images 60
3.11 ZnO/MoS_2 heterostructures on Au(111) – High-magnification STM images and line profiles 61
3.12 ZnO/MoS_2 heterostructures on Au(111) – STS spectra 62
3.13 Ag(111) – Large scale STM images and line profile 64
3.14 MoS_2/Ag(111) annealed at 650 K – STM images and line profile 65
3.15 MoS_2/Ag(111) annealed at 650 K – High-magnification STM images of the Ag – S surface phase . 65
3.16 MoS_2/Ag(111) annealed at 650 K – High-magnification STM images and line profile 66
3.17 MoS_2/Ag(111) annealed at 730 K – Large scale STM images and line profile 67
3.18 MoS_2/Ag(111) annealed at 730 K – High-magnification and atomic-resolution STM images. 2D Fast Fourier Transform 67
3.19 MoS_2/Ag(111) annealed at 730 K – Point defects 68
3.20 MoS_2/Ag(111) annealed at 730 K – Line defects and partially embedded MoS_2 islands 69
3.21 MoS_2/Ag(111) obtained by means of 30 laser pulses – STM images and line profile 70
3.22 MoS_2/Ag(111) obtained by means of 50 laser pulses – Large scale STM images 71
3.23 Ag(111) – STS spectra 72
3.24 MoS_2/Ag(111) – STS spectra 72
3.25 MoS_2/Ag(111) – STS spectra acquired on the island surface and in correspondence of island edges and grain boundaries 73
3.26 MoS_2/Ag(111) – AES spectra 74
3.27 MoS_2/Ag(111) – Raman spectra 75
3.28 MoS_2/Ag(111) – Photoluminescence (PL) measurements 77
3.29 Si/Ag(111) – Large scale STM images after 1 laser pulse, after 5 additional laser pulses and after annealing at 410 K 79
3.30 Si/Au(111) – STM images after 1 laser pulse and after 5 additional laser pulses 80
3.31 Si/Au(111) – STM images after annealing at increasingly high temperature 80
3.32 Si/Au(111) – STM images and line profile after 30 laser pulses 81
3.33 Si/Au(111) – STM images after a 410 K annealing treatment 82
3.34 Si/Au(111) – STM images after a 465 K and a 565 K annealing treatment 83
3.35 Si/Au(111) deposited in Ar – STM images after 30 laser pulses 84
3.36 Si/Au(111) deposited in Ar – STM images after a 410 K annealing treatment 84
3.37 Si/Au(111) deposited in Ar – STM images after a 485 K annealing treatment 85
3.38 Si/Au(111) deposited in Ar – STM images after a 560 K annealing treatment 85
3.39 Si/Au(111) deposited in Ar – STM images after a 630 K annealing treatment 85

List of Tables

1 Raman shift and width of the E^1_{2g} and the A_{1g} peaks, frequency difference between the two peaks and intensity ratio (A_{1g}/E^1_{2g}) for the MoS_2/Ag(111) systems produced by means of 30 and 50 laser pulses, for the MoS_2/Au(111) system and for bulk MoS_2 76

Introduction

Two-dimensional (2D) materials have attracted increasing interest in recent years since the quantum confinement of a material (at least along one direction) may affect its structure and properties, resulting in novel physical and chemical behaviours and in electronic, optical, vibrational and magnetic properties different from those of the bulk form. The most popular example of a 2D material is represented by graphene – i.e. an atomically thin material made up of sp^2 hybridized carbon atoms arranged in the plane in such a way to form a honeycomb lattice. However, since the discovery of the very peculiar properties of graphene [1] in 2004, the class of 2D materials has experienced a formidable expansion thanks to the successful synthesis and investigation of 2D transition metal dichalcogenides (TMDs), such as MoS_2 and WS_2, 2D hexagonal boron nitride (h-BN), silicene – i.e. graphene-like silicon – and so on. Furthermore, 2D materials can be employed in the fabrication of 2D heterostructures, which are incredibly promising for a large variety of future applications, ranging from nanoelectronic to optoelectronic devices, from solar cells to field effect transistors (FETs).

This thesis describes the production of two-dimensional semiconducting materials and nanostructures by means of a peculiar physical vapour deposition (PVD) technique – i.e. pulsed laser deposition (PLD) – and the subsequent characterization of the obtained structures using scanning tunneling microscopy (STM) and spectroscopy (STS). In the framework of this thesis work, this experimental approach has been also applied to the fabrication of 2D heterostructures, which are peculiar both from the synthesis procedure point of view and for the type of 2D materials that are coupled. Indeed, attention will be focused on molybdenum disulphide (MoS_2) and zinc oxide (ZnO) heterostructures grown on top of the (111)-surface of a gold substrate, on 2D MoS_2 nanostructures deposited onto Ag(111) and, finally, on the attempt of producing silicon at the two-dimensional limit by means of PLD, a route that has never been explored experimentally.

Subsequently, the obtained samples have to be characterized and the use of surface science techniques and, more specifically, of scanning tunneling microscopy (STM) is particularly interesting since it allows to image the sample surface directly in the real space and to achieve atomic resolution. Indeed, STM is a peculiar imaging technique based on a quantum-mechanical effect - i.e. the tunneling of electrons from a sharp metal tip to the sample surface (or vice versa), which may occur when the tip and the sample are put very close one to the other, within a fraction of a nanometer. The STM tip is capable of imaging the investigated surface with an incredibly high spatial resolution, even down to the nanometer and atomic scale, thus making STM suitable for the nanoscale study and investigation of the morphological and structural features of surfaces, interfaces and nanostructures and for the deep understanding of peculiar physical phenomena occurring at the atomic scale. Furthermore, the scanning tunneling microscope may be also employed in order to perform spectroscopic measurements. Indeed, scanning tunneling spectroscopy (STS) allows to investigate the local electronic properties of the sample and to probe the surface electronic density of states (DOS) around the Fermi level. Hence, STM and STS are ideal characterization tools to study the properties of semiconducting materials and heterostructures at the 2D limit, which is necessary to address the possible future applications of these materials, such as in the field of catalysis, optoelectronics and energy production.

This thesis is organized according to the following scheme:

- **Chapter 1**: A general introduction to the topic of two-dimensional semiconducting materials is provided, focusing the attention on molybdenum disulphide (MoS_2), zinc oxide (ZnO) and silicon. The research framework is delineated discussing experimental works of interest already reported in the literature in order to favour the comprehension and the interpretation of the obtained experimental results. Finally, the objectives of this thesis work are outlined more in detail.

- **Chapter 2**: The synthesis and characterization techniques employed during the experimental activity presented in this thesis are described both in terms of the needed experimental apparatus and in terms of the physical phenomena at the basis of their working principle. Hence, the most relevant concepts related to pulsed laser deposition (PLD) and scanning tunneling microscopy (STM) and spectroscopy (STS) are introduced, together with a brief explanation of other characterization tools used during this research activity – i.e. Auger electron spectroscopy (AES) and Raman and photoluminescence (PL) spectroscopies.

- **Chapter 3**: The obtained experimental results are reported and discussed in detail. The first part of this chapter is devoted to the STM/STS characterization of ZnO/MoS_2 heterostructures deposited on top of an Au(111) substrate. The second part of the chapter is devoted to the study of the MoS_2/Ag(111) system while, in the last part, the results related to the preliminary experimental activity concerning the deposition of 2D silicon by means of PLD are briefly presented.

- **Chapter 4**: The most relevant results achieved during the reported experimental activity are summarized and the possible future perspectives are briefly outlined.

During the experimental activity presented in this thesis work, STM and STS measurements have been performed for the investigation of ZnO/MoS_2 heterostructures and for the study of the MoS_2/Ag(111) system, while only a preliminary structural and morphological characterization of the 2D Si/Ag(111) and 2D Si/Au(111) systems have been carried out. Furthermore, AES measurements and Raman and PL spectroscopies have been employed in order to deeply investigate 2D MoS_2 deposited onto Ag(111) and the effect of the interaction with the underlying silver substrate. I personally conducted the experimental work, together with the analysis and interpretation of the obtained data.

Chapter 1

Two-dimensional semiconducting materials

Two-dimensional (2D) materials have assumed growing importance both in research activity and in the realm of technological applications since the extensive investigation of the peculiar properties of graphene – i.e. two-dimensional carbon – in 2004. This chapter wants to be an introduction to the topic of 2D semiconducting materials and has the aim of presenting the research framework and motivating the experimental activity that focuses on this type of materials. Section 1.1 gives an overview of semiconducting materials at the two-dimensional limit, devoting particular attention to molybdenum disulphide, zinc oxide and silicene, which have been considered in this thesis work. In sections 1.2 and 1.3, a brief review of the main synthesis methods and the most important characterization techniques for these systems is presented; pulsed laser deposition (PLD) and scanning tunneling microscopy (STM) are given particular emphasis since they are the main experimental methods used in this research activity. In section 1.4 literature works are presented in which the use of PLD and STM is combined for the investigation of these systems. Finally, in section 1.5 the objectives of this thesis work are defined.

1.1 Two-dimensional (2D) materials beyond graphene

Two-dimensional (2D) materials have historically been one of the most studied classes of materials due to the surprising abundance of unusual physical phenomena that occur when a material is confined at the two-dimensional scale and because their fascinating properties promise to be exploited in new or advanced technological applications. Within the emerging class of 2D materials, graphene – observed for the first time in 2004 by Andrej Geim and Konstantin Novosëlov – has undoubtedly attracted the greatest attention thanks to its remarkable electronic and mechanical properties [1]. However, the intrinsic limitations of graphene, such as the absence of a band gap – necessary to provide good performances in field effect transistors (FETs) and in other electronic devices – have motivated research on other 2D materials. Indeed, in the last two decades, an increasing number of experimental activities has been focused on the investigation of materials at the two-dimensional limit: two-dimensional oxides [2], transition metal dichalcogenides (TMDs) [3], hexagonal boron nitride (h-BN) [4], silicene [5] and so on.

The great interest in 2D materials is related to the effect that quantum confinement has on the properties of the materials themselves. Indeed, when a material is confined (at least along one dimension), its physical, mechanical, optical, electronic and magnetic properties are incredibly modified and therefore the features of the 2D materials are highly different from those of the same materials in the bulk form. In order to better explain this concept, 2D molybdenum disulphide (2D MoS_2), 2D zinc oxide (2D ZnO) and silicene – i.e. two-dimensional silicon - can be taken into account, as they are also the materials under investigation in this thesis work.

Molybdenum disulphide (MoS_2) is present in nature in the form of molybdenite, a layered material belonging to the family of transition metal dichalcogenides (TMDs), and it can be used for a lot of different applications, such as like a lubricant or in electronic devices. The structure of bulk MoS_2 is shown in figure 1.1(a) and it is very similar to that of graphite: it consists of S-Mo-S sheets characterized by strong intra-layer covalent bonding between Mo and S atoms and kept together by weak van der Waals forces. However, the single sheets can also exist as stable two-dimensional monolayers. These single layers are chemically rather inert and consist of closed-packed Mo hexagonal layers sandwiched in between two S layers in a trigonal prismatic configuration [3]. The peculiarity of MoS_2 is related to the thickness-dependence of its electronic properties:

MoS_2 is an indirect band gap semiconductor with an energy gap of 1.2 eV in the bulk form but, when its thickness is reduced down to that of a monolayer, quantum confinement effects cause an indirect-to-direct transition in such a way that single layer MoS_2 is characterized by a direct band gap of 1.9 eV [6]. This aspect can be observed by considering the electronic band structures of bulk MoS_2 and MoS_2 monolayer (shown in figure 1.1(b)) and leads to an enhanced photoluminescence of single layer MoS_2 [7] making this material attractive for the fabrication of optoelectronic devices. Furthermore, monolayer MoS_2 can in principle be used in next generation electronic devices because transistors based on atomically thin MoS_2 have proven large carrier mobilities of 200 – 500 cm^2/Vs and excellent on/off current ratios (>10^6) [8]. Finally, the catalytic properties of MoS_2 have the potential for applications in hydrodesulphurization processes [9] and hydrogen evolution reactions [10].

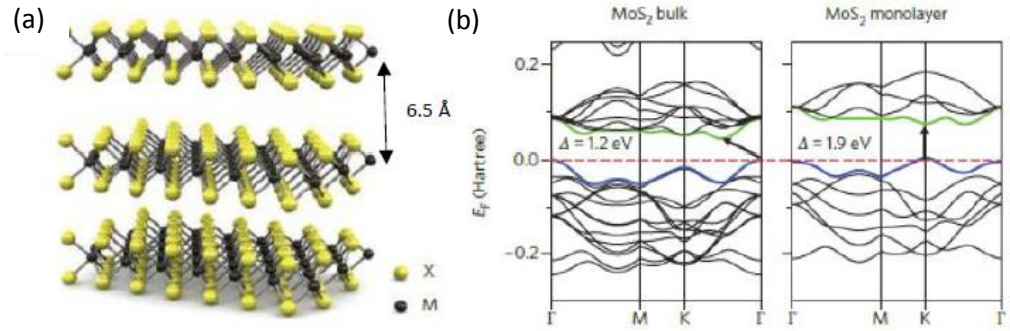

Figure 1.1: (a) Structure of bulk MoS_2, showing also the interlayer spacing between adjacent layers (6.5 Å). 2D MoS_2 consists of only one of the layers depicted in the image. (b) Band structures calculated from first-principles density functional theory (DFT) for bulk and monolayer MoS_2. Reproduced from [3].

Similarly, zinc oxide (ZnO) is a semiconducting material that is part of the II-VI semiconductor class. It has been studied especially as promising material for optoelectronic applications thanks to its peculiar optical and electronic properties such as, for example, a large direct band gap of 3.37 eV. Starting from these considerations, it may be very interesting to consider two-dimensional ZnO, remembering that quantum confinement can produce relevant changes in the properties of the material.

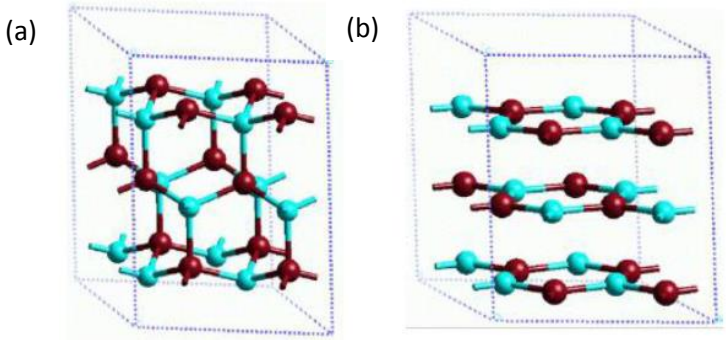

Figure 1.2: Schematic representation of (a) the bulk ZnO wurtzite structure and (b) the two-dimensional graphene-like ZnO structure [11] that occurs due to a specific depolarization mechanism taking place at the two-dimensional limit.

In the case of ZnO, quantum effects cause a remarkable structural modification. The stable form of bulk ZnO is characterized by the wurtzite structure, in which each Zn atom is surrounded by four O atoms in a tetrahedral configuration, and vice versa (figure 1.2(a)). However, at the two-dimensional limit, theoretical calculations have shown that ZnO forms a hexagonal graphitic-like structure that is stable only when the material is sufficiently thin – i.e. composed of only few atomic layers. Graphene-like ZnO is shown in figure 1.2(b): the Zn cations and the O anions are arranged in a trigonal-planar configuration [11]. In this kind of structure, the different atomic layers are stacked one on top of the other thanks to weak van der Waals interactions and the stacking is characterized by an ABAB sequence, in which Zn atoms of the second layer

are on top of the O atoms of the first layer, and vice versa. As regards the electronic properties, 2D ZnO is a direct band gap semiconductor, just like its bulk counterpart, but the size of the energy gap is different. Indeed, Kang *et al.* [12] carried out theoretical calculations in order to determine the electronic band structure of ZnO as a function of the number of layers and they found that the band gap decreases as the thickness of the material (and so the number of atomic layers) increases, as can be evaluated from figure 1.3. This means that in 2D graphene-like ZnO the band gap is larger than in the case of bulk ZnO and that also here, just as in MoS_2, the electronic properties of the material are thickness-dependent. Thanks to these peculiar electronic and optical properties, 2D ZnO has attracted large interest as a promising candidate for a wide range of applications, such as nanoelectronics, optoelectronics and bio sensing [2].

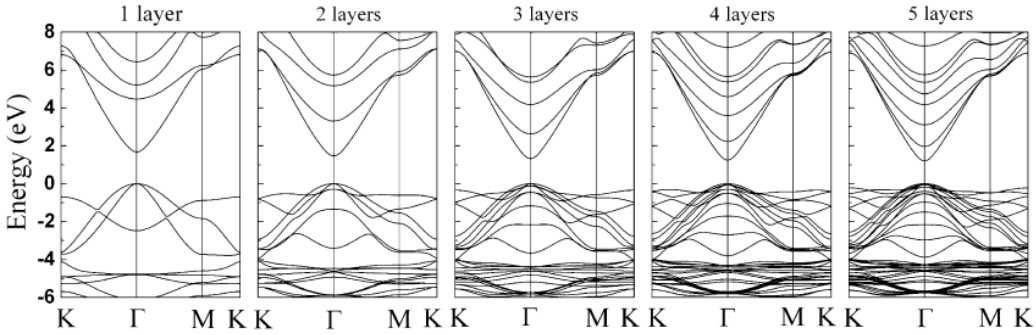

Figure 1.3: Electronic band structure of ZnO as the thickness of the film increases from one layer to five layers [12].

In contrast with 2D MoS_2 and similarly to the case of graphitic-like ZnO, silicene – i.e. the two-dimensional allotrope of Si consisting of a 2D graphene-like hexagonal lattice - does not have a layered and exfoliable bulk-like counterpart. Indeed, silicene is probably the first example of a 2D artificial honeycomb-like lattice made up of Si atoms because, in nature, there exists no graphitic phase of bulk Si, characterized by a diamond-like structure. This is because Si atoms, due to their larger ionic radius, prefer to hybridize sp^3 and to arrange in a tetrahedral configuration [5], while carbon is characterized by a sp^2 hybridization in graphite. Nevertheless, in 1994 Takeda and Shiraishi [13] theoretically considered the Si equivalent of graphite by first-principles calculations finding that this structure should be made up of corrugated rather than planar hexagonal layers due to the interplay between sp^2 and sp^3 bonding and, subsequently, Cahangirov *et al.* [14] confirmed that Si could have stable 2D honeycomb structures.

In the last years many researchers have succeeded in growing silicene on top of metallic substrates, such as Ag(111) [15, 16], considering that the substrate is essential for the growth of 2D silicon as silicene can not exist in its free-standing form (at least so far). In contrast to graphene, silicene is not planar and self-organizes in structurally different superstructures, depending on the lattice matching with the host substrate. This feature can be referred to as the polymorphic nature of silicene – i.e. the capability of Si atoms to accommodate on commensurate substrates in several buckled structures with different periodicities but an overall hexagonal symmetry [5]. In reality, however, the polymorphism of silicene is not only substrate-specific because different silicene superstructures can sequentially take place or coexist on the same substrate. Silicene grown on top of an Ag(111) substrate is probably the most studied system (both theoretically and experimentally), even if it is not the simplest one due to the presence/coexistence of different surface structures, the so-called silicene phases. In figure 1.4 three representative silicene superstructures on Ag(111) (derived from theoretical calculations [17]) are shown together with their experimental scanning tunneling microscopy (STM) images [5], considering that STM is a very powerful characterization technique able to image both the topographic and the electronic properties of a surface, even at the atomic length scale. Figure 1.4(a) depicts the very first silicene phase ever observed on Ag(111), the 4 x 4 silicene phase, in which four lattice spacings of the Ag(111) surface match exactly to three lattice constants of silicene along the Ag[110] direction, resulting in a cell parameter of 3.926 Å for the silicene hexagonal lattice. Moreover, the Si atoms in the unit cell belong to two different planes: 12 of them are on

the bottom plane only 2.17 Å far from the underlying silver surface, while the remaining six Si atoms are placed on top of Ag atoms, 2.92 Å far from the Ag surface. These upper Si atoms are responsible for the characteristic flower-like pattern that can be observed in the STM image of figure 1.4(b).

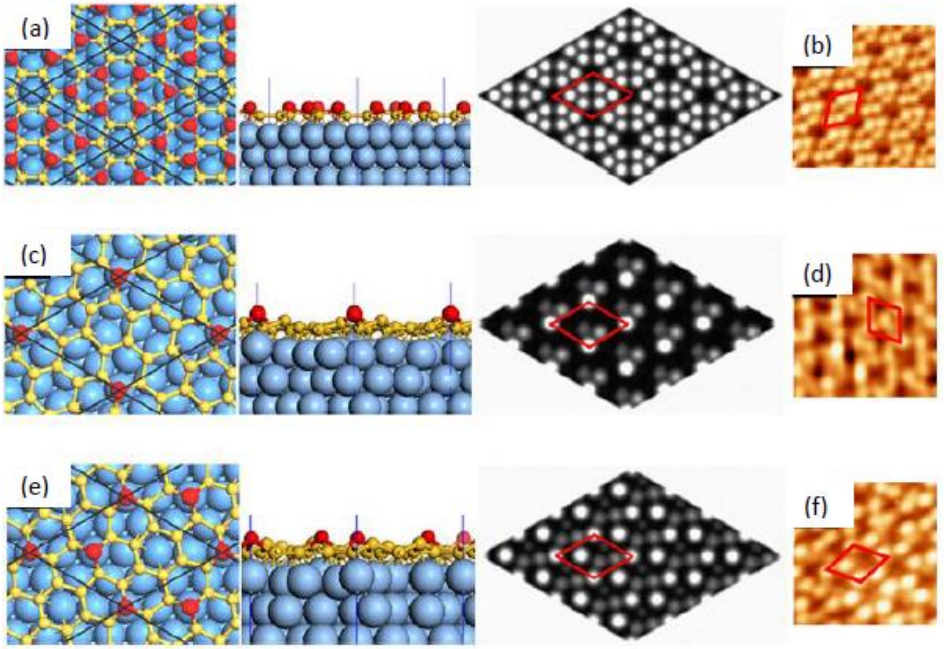

Figure 1.4: (a), (c), (e) Top views, side views and simulated STM images of the 4 x 4, $\sqrt{13}$ x $\sqrt{13}$ and $2\sqrt{3}$ x $2\sqrt{3}$ silicene superstructures, respectively [17]. (b), (d), (f) Experimental STM images of the corresponding silicene phases [5].

4 x 4 silicene can coexist with another kind of superstructure, the so-called √13 x √13 phase (shown in figure 1.4(c)). This silicene supercell is rotated by approximately 13.9° with respect to the Ag[110] direction and contains 14 Si atoms, arranged again on two distinct planes. However, just four of them are sitting on the top plane forming the buckled structure and giving the STM pattern of figure 1.4(d). In addition, other silicene phases can be observed on the silver substrate, such as the 2√3 x 2√3 superstructure characterized by a unit cell with 12 planar and two buckled atoms (see figure 1.4(e) and the experimental STM image of figure 1.4(f)). In reality, although this phase has been observed to coexist with both the 4 x 4 and the √13 x √13 superstructures, typically it tends to form large domains when Si is deposited onto the Ag(111) surface at higher temperatures.

In the realm of 2D semiconducting materials, silicene finds its way not only as the extreme dimensional reduction of bulk silicon (widely used in microelectronics), but also for its expected capability to change its electronic properties in response to structural and chemical modifications. Indeed, silicene can be more or other than the simple reduction of Si down to the 2D limit because it is a silicon allotrope with both structural and electronic properties different from those of bulk Si. Up to now, the most promising application of this material is in field effect transistors (FETs) [18].

Lastly, it is worth mentioning that, in parallel with the experimental efforts on graphene-like materials, another research field has recently emerged. It deals with the so-called heterostructures that are essentially of two different types. 2D vertically stacked heterojunctions are fabricated by stacking different 2D materials one on top of the other in such a way that they are kept together by weak van der Waals forces [19], while lateral heterostructures consist of 2D materials covalently bonded one to the other in the horizontal plane [20]. Examples of both types of structures are shown in figure 1.5. Thanks to the fact that 2D structures provide a full range of materials, including large band gap insulators, semiconductors with high carrier mobility and semimetals, 2D heterostructures are suitable for a very broad range of applications: field

effect/tunneling transistors, biosensors, light emitting diodes (LEDs), light detectors, photovoltaic and energy storage devices [20].

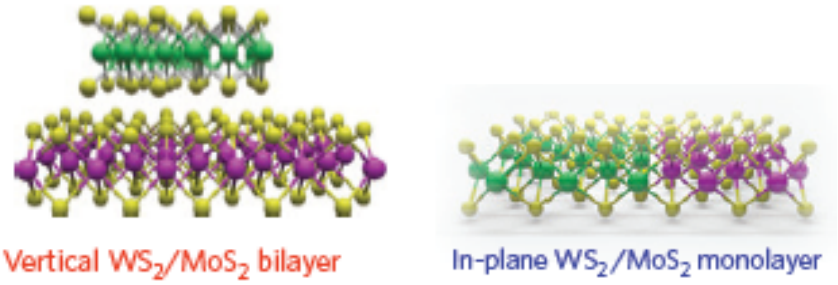

Figure 1.5: van der Waals (left) and lateral (right) heterostructures consisting of WS_2 and MoS_2 monolayers [21].

1.2 Synthesis of two-dimensional (2D) materials

In recent years, significant progress has been made in the synthesis of atomically thin materials with the aim of developing reproducible, reliable and scalable experimental procedures that could be applied also in the industries for the fabrication of real devices. These production techniques can be roughly subdivided into three main categories: exfoliation, chemical processes and physical methods [4].

The first synthesis method to be developed was the so-called micromechanical exfoliation that was successfully used in 2004 in order to produce single-layer graphene. This technique is conceptually very simple: it consists in the use of scotch tape in order to exfoliate graphite and obtain flakes of material with different thicknesses; some of these flakes can be monolayers. This experimental procedure can be applied not only in the case of graphene but also in order to produce other 2D nanostructures starting from layered materials (like MoS_2) that can be exfoliated very easily. Micromechanical exfoliation is still a very used technique in laboratories because the two-dimensional flakes produced are characterized by very high quality and, in addition, it is very easy to fabricate van der Waals heterostructures by putting one on top of the other the previously exfoliated 2D materials [20]. However, this technique has also relevant limitations, especially the poor control over the thickness (and hence the number of layers) and the small lateral size of the exfoliated flakes. An improvement of this experimental procedure is represented by liquid-phase exfoliation that exploits proper chemical species in solution and allows the delamination of a precursor layered crystal into its single layers. Usually, this technique is based on the intercalation reaction with bulky guest species that increases the interlayer spacing and facilitates the delamination process. Nevertheless, it is important to underline that both these exfoliation techniques can be applied only in order to produce two-dimensional structures starting from materials that, in the bulk form, consist of separate layers kept together by weak van der Waals interactions. Therefore, these techniques are not suitable for the production of monolayers starting from non-layered bulk materials (like in the case of ZnO or silicene).

Consequently, it was necessary to develop different synthesis methods based on a bottom-up approach, instead of the top-down one exploited in the case of the exfoliation procedures. This new approach consists in fabricating the material starting from its elemental constituents (atoms or molecules) and is at the basis of both chemical and physical deposition techniques, in which the growth of the material occurs on top of a specific substrate (such as gold, silver, silicon and so on).

Among all the possible chemical methods, chemical vapour deposition (CVD) is surely the most powerful one as it allows producing highly crystalline two-dimensional materials on large areas (even at the centimetre length scale). In CVD processes, volatile gaseous precursors are involved in a chemical reaction that results in the deposition of the 2D material on top of the substrate, which is typically kept at elevated temperature (around 1000 °C) in order to favour the deposition process and the ordering/crystallization of the material. However, this last aspect is not very desirable, especially in the perspective of large-scale production of 2D

materials, and deposition techniques involving a much lower processing temperature have been developed. Indeed, physical vapour deposition (PVD) methods allow the deposition of several materials exploiting synthesis temperatures much lower than those characteristic of CVD. PVD techniques are processes in which the material vaporizes (in the form of atoms or molecules), travels towards the substrate remaining in the vapour phase or in the form of a plasma and finally condensates onto the substrate itself. There exist many PVD techniques that can be used to synthetize 2D materials such as thermal evaporation, sputtering, molecular beam epitaxy (MBE) and pulsed laser deposition (PLD). Among all these methods, attention will be focused on PLD because, while the conventional top-down techniques and CVD processes are characterized by some significant limitations, PLD has proven to be a good alternative for thin films deposition due to its capability of ablating any material, obtaining a stoichiometric transfer of the target material onto the substrate and depositing the vaporized material on a quite large area (with a size in the order of centimetre). For these reasons, PLD has been chosen as the growth technique used to deposit MoS_2, ZnO and silicon in this thesis work.

Pulsed laser deposition is based on the ablation of a solid target by intense laser pulses [22]. More precisely, when the pulses of the focused laser beam hit the surface of the target, the laser-matter interaction generates a plasma plume (containing both atoms and ionized species) that moves towards the substrate placed in front of the target itself (as shown in figure 1.6). The ejected particles deposit on the substrate surface forming nanostructures or ultrathin films that maintain the stoichiometry of the ablated material. PLD is capable of controlling very well both the morphology and the thickness of the deposited material thanks to the fact that several different parameters are able to affect the laser-target interaction and so the deposition process. These parameters are, for instance, the target-substrate distance, the pressure of the background atmosphere, the laser fluence and the frequency of the laser pulses [22]. Other advantages of using PLD as a synthesis method include the high growth rate, the low cost and the capability of depositing the ablated material on a large area with good uniformity. More details about the working principle and the physical phenomena taking place during pulsed laser deposition will be given in section 2.1.

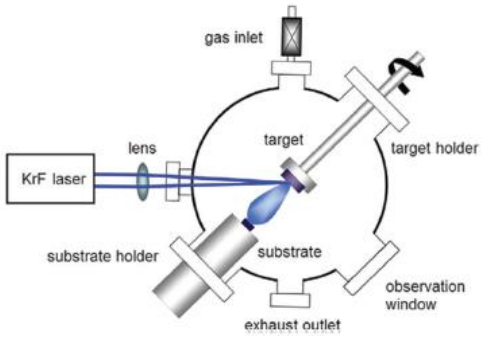

Figure 1.6: Schematic of the experimental setup for pulsed laser deposition [22].

In recent years, PLD has been increasingly used in the synthesis of 2D materials, such as graphene [22], transition metal dichalcogenides (like, for instance, MoS_2 and WS_2 [23]), hexagonal boron nitride [24] and metal oxides (such as zinc oxide). On the contrary, as regards the growth of silicene, it is worth noting that, up to now, no research group has tried to deposit two-dimensional Si and to grow ultrathin 2D Si films using pulsed laser deposition.

Recent literature works in which PLD has been employed to deposit MoS_2 and ZnO on various substrates are reported with more details in sections 1.2.1 and 1.2.2, respectively.

1.2.1 Two-dimensional molybdenum disulphide by pulsed laser deposition

In order to exploit MoS_2 in working devices, it is necessary to develop a synthesis procedure that allows the fabrication of high quality ultrathin films. For this reason, in recent years pulsed laser deposition has been used to grow MoS_2 on top of different substrates, both insulating and metallic ones.

The first attempt in growing MoS_2 by PLD was carried out in 1988 when molybdenum disulphide thin films were deposited on stainless steel substrates at a rather low growth temperature (around 600 K) [22]. However, even though the films showed the same stoichiometry of the ablated target, their internal structure was unknown and their thickness was too large to consider them as 2D materials.

Later, Serrao *et al.* [25] deposited MoS_2 on top of three different substrates: Al_2O_3(0001), GaN(0001) and SiC-6H(0001). The deposition was carried out at 973 K, keeping the KrF excimer laser energy at 50 mJ per pulse and under a residual background pressure from target ablation of 1 x 10^{-4} mbar. The samples were subsequently cooled down to room temperature at a rate of 10 K/min and characterized by means of X-ray diffraction (XRD) and Raman spectroscopy. The as-grown films showed a high degree of crystallinity and thickness uniformity over a large area (5 x 5 mm^2). This last feature can be evaluated by acquiring Raman spectra in different positions of the substrate and comparing the separation between the E^1_{2g} and the A_{1g} peaks corresponding to the in-plane and out-of-plane vibrational modes, respectively (figure 1.7(a)). As the distance between the two peaks is the same in the four corner positions of the substrate, the uniform thickness of the deposited films can be confirmed. Finally, Serrao and co-workers compared the Raman spectra of the MoS_2 thin films grown onto the three different substrates: they observed a similar Raman signal in terms of peak position, peak height and line shape irrespective of the substrate considered suggesting that the films only weakly adhere to the substrate by van der Waals forces (figure 1.7(b)).

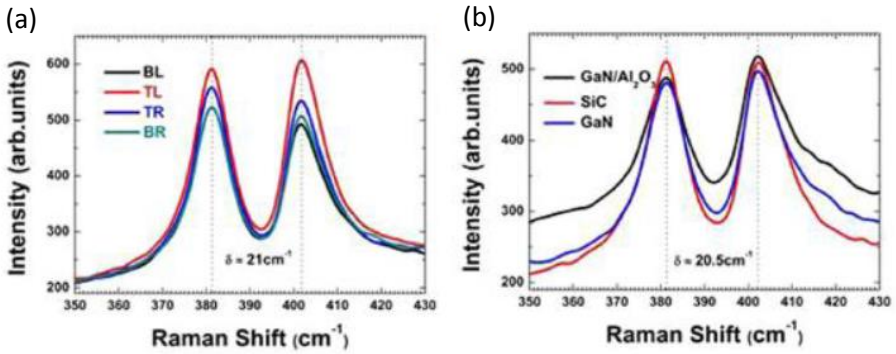

Figure 1.7: (a) Raman spectra acquired at the four corner positions (bottom left (BL), top left (TL), top right (TR) and bottom right (BR)) of a 5 x 5 mm^2 bilayer MoS_2 film grown on top of a GaN substrate. (b) Raman spectra of a monolayer MoS_2 on GaN/Al_2O_3(0001) (black curve), SiC-6H(0001) (red curve) and GaN(0001) (blue curve). Reproduced from [25].

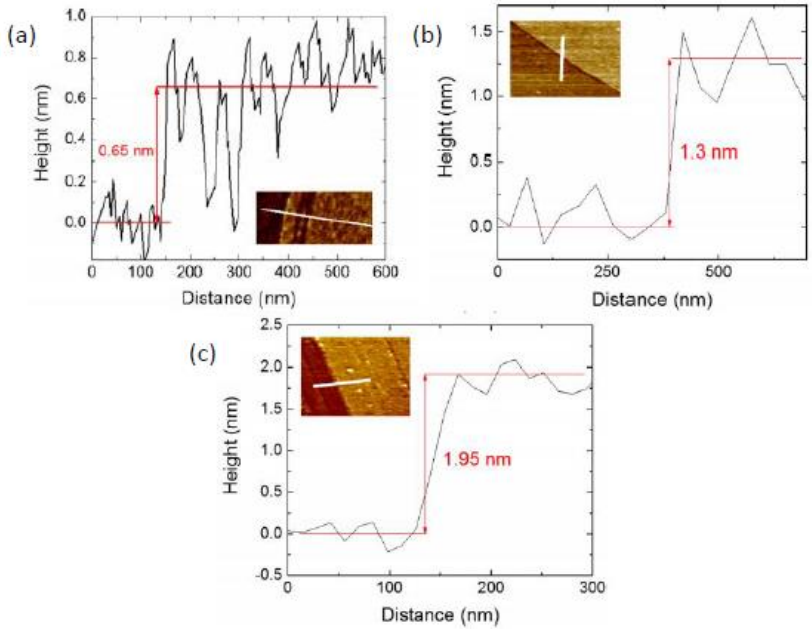

Figure 1.8: AFM thickness profiles of (a) monolayer, (b) bilayer and (c) trilayer MoS_2 grown by PLD on top of a sapphire(0001) substrate [26].

Following the work by Serrao and co-workers, Siegel *et al.* [26] performed the pulsed laser deposition of monolayer and few-layer MoS_2 thin films onto a single-crystal sapphire(0001) substrate. The films were deposited by ablating a MoS_2 target with a pulsed KrF excimer laser (wavelength: 248 nm) using an energy fluence of 1.5 J/cm^2 and heating the substrate up to a temperature of 973 K. The films thus prepared were annealed *in situ* for 5 min at 973 K before cooling. As in the previous work, the high thickness uniformity of the deposited MoS_2 films on a centimetre length scale was demonstrated by means of Raman spectroscopy. Furthermore, Siegel and co-workers proved the ability of the PLD technique to finely control the thickness of the deposited film. Indeed, just controlling the number of laser pulses, films of different thicknesses could be grown with very high precision. This aspect can be appreciated by considering the AFM thickness profiles (figure 1.8) of monolayer, bilayer and trilayer MoS_2 obtained by ablating the target with 50, 100 and 150 laser pulses, respectively. The interlayer spacing of bulk MoS_2 (6.5 Å) can be observed suggesting (as in the previously reported work) a weak interaction between the MoS_2 film and the underlying substrate.
Another work deserving to be mentioned is that of Serna *et al.* [27] in which pulsed laser deposition was proven again to be capable of depositing MoS_2 thin films over large areas, enabling also good thickness control on the whole substrate. The growth process was carried out on different types of substrates: monocrystalline (such as sapphire and quartz), polycrystalline (like HfO_2) and also on amorphous SiO_2. Serna and co-workers remarked that the number of layers (and hence the thickness) of the deposited films can be engineered by tuning the PLD parameters (deposition pressure, laser energy, repetition rate of the laser pulses and so on). The thickness of the deposited material can be evaluated through transmission electron microscopy (TEM) that allows observing the cross section of the film, but also Raman spectroscopy. Indeed, by considering the distance between the E^1_{2g} and the A_{1g} Raman peaks (δ), it is possible to obtain information about the number of layers: the expected δ values are 18 cm^{-1} for one layer, 22.4 cm^{-1} for two layers, 23 cm^{-1} for three layers and 25 cm^{-1} for bulk MoS_2 [28]. In addition, a comparison on the quality of the MoS_2 thin films deposited on the different substrates is presented: MoS_2 grown on HfO_2 (figure 1.9(c)) seems to feature a better quality than films deposited on amorphous SiO_2 (figure 1.9(a)) and quartz (figure 1.9(b)) substrates. This aspect is also evident in the corresponding Raman spectra (figure 1.9(d)), remembering that sharp peaks are an evidence of higher quality.

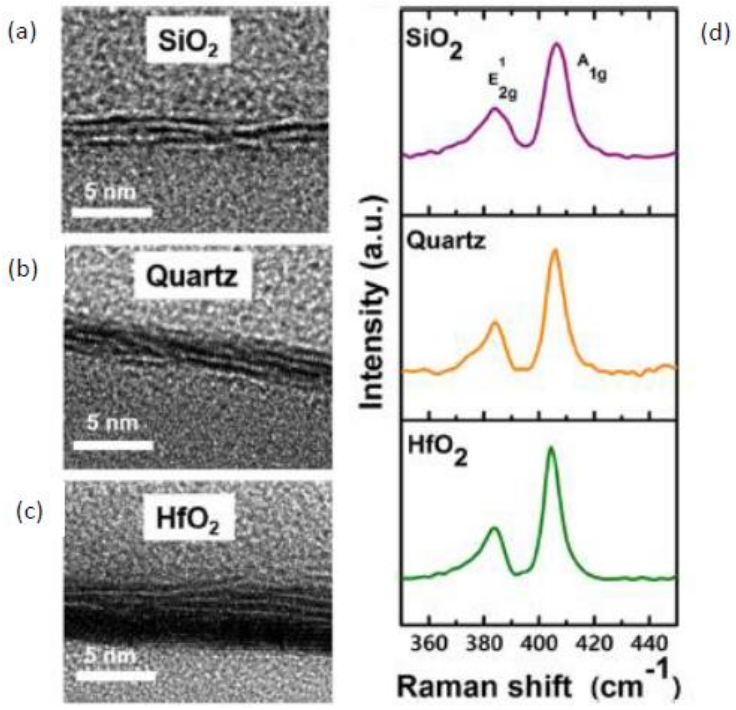

Figure 1.9: TEM images of MoS_2 thin films deposited on different substrates: (a) amorphous SiO_2, (b) monocrystalline quartz and (c) polycrystalline HfO_2; the corresponding Raman spectra are shown in (d) [27].

In all the previously reported papers, molybdenum disulphide has been deposited on top of an insulating substrate. On the contrary, information and studies on the growth of monolayer and few-layer MoS_2 using metal substrates are still limited, probably because of the stronger interaction between MoS_2 and the underlying substrate. Indeed, when depositing MoS_2 on top of a silver substrate the formation of the Ag_2S phase can affect the properties of the overall system [29] and when the deposition is carried out on top of a gold substrate charge transfer phenomena between Au and MoS_2 can take place, causing a significant modification of the electronic properties of the deposited film [30]. However, the use of metal substrates can provide some advantages, including a reduction in the growth temperatures and the ease of producing metal-semiconductor contacts without film transfer.
The growth of few-layer MoS_2 on different metal substrates by means of pulsed laser deposition has been investigated by Loh and Chua [29] in 2014. They considered Ag, Al, Ni and Cu as possible substrates. More in detail, molybdenum disulphide has been deposited using a KrF excimer laser (laser energy: 50 mJ, repetition rate: 10 Hz, pulse duration: 25 ns) for a duration of 10 s to yield an estimated 5 nm thick MoS_2 film on the substrate surface. During the deposition, the substrate temperature was kept at 773 K and the successive cooling was carried out at a controlled rate of 50 °C/min. The obtained films were then characterized using TEM and Raman spectroscopy. Eventually, Loh and Chua discovered that only the silver substrate was successful in forming a highly crystalline MoS_2 film while Mo and S atoms on the other metal substrates tend to form a more disordered structure. The MoS_2/Ag system is shown in figure 1.10: in between the silver substrate and the overlying MoS_2 thin film, the Ag_2S phase is formed due to the strong interaction of S and Ag. The presence of this intermediate layer favours the crystallization of the deposited material helping in the production of MoS_2 thin films characterized by a good degree of crystallinity.

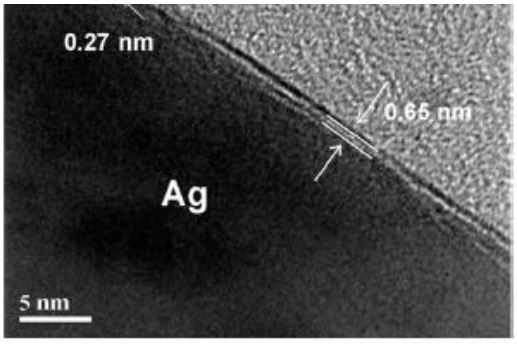

Figure 1.10: Cross-sectional TEM image of the MoS_2/Ag sample obtained by means of PLD using a laser energy of 50 mJ and a deposition time of 10 s [29].

1.2.2 Two-dimensional zinc oxide by pulsed laser deposition

ZnO thin films have been successfully grown by means of a wide range of deposition procedures, such as chemical vapour deposition, molecular beam epitaxy, sputtering and others. However, pulsed laser deposition has not been extensively used in order to grow ZnO thin films and, only in recent years, works on zinc oxide deposited by means of PLD on different substrates have appeared in the literature.
In 1999 Choopun *et al.* [31] exploited PLD in growing ZnO thin films on sapphire(0001) and tried to evaluate the effect of the oxygen background pressure on the properties of the deposited material. Indeed, the deposition was carried out at an optimized growth temperature of about 1000 K and at various O_2 background pressures ranging from 10^{-5} to 10^{-1} mbar and the surface morphology of the deposited films was investigated by means of atomic force microscopy (AFM). As it can be observed from figure 1.11(a), films grown under a low oxygen pressure (10^{-5} – 10^{-4} mbar) are characterized by a honeycomb-like structure with three-dimensional (3D) growth features that cause a quite high roughness of the deposited films. In figure 1.11(b), a transition towards the growth of a smooth film can be observed while a further increase in the oxygen background pressure up to 10^{-1} mbar seems to have an opposite effect and cause again an increase of the surface roughness of the ZnO thin film (figure 1.11(c)).

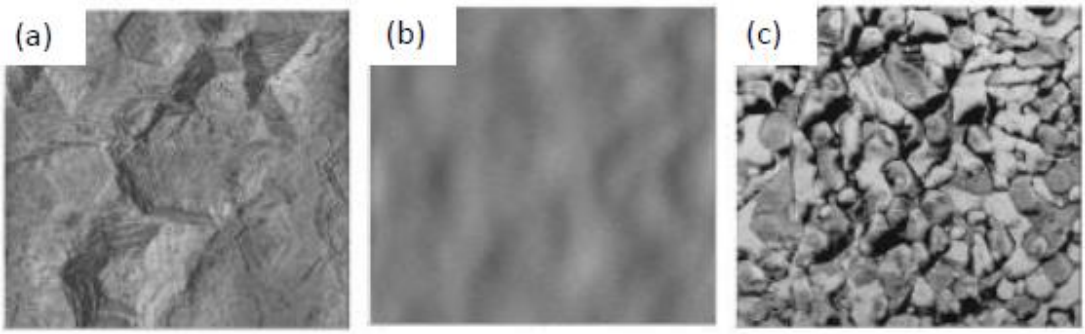

Figure 1.11: AFM images (2 µm x 2 µm) of ZnO films grown at various oxygen pressures: (a) 10^{-4} mbar, (b) 10^{-2} mbar and (c) 10^{-1} mbar [31].

Subsequently, Claeyssens *et al.* [32] studied the growth of zinc oxide thin films both theoretically and experimentally. On one hand, they demonstrated that ZnO assumes a graphitic-like structure at the two-dimensional limit – i.e. when the ZnO film is sufficiently thin and consists of only few atomic layers – while, on the other hand, they deposited ZnO by pulsed laser deposition on top of a silicon substrate. More precisely, the films were grown by pulsed ArF laser ablation (wavelength: 193 nm) using a laser energy of 150 mJ, an O_2 background pressure of 10^{-2} mbar and a substrate temperature ranging from 298 K (room temperature) to 1023 K. As regards the characterization of the deposited material, scanning electron microscopy (SEM) was used to provide visual images of the film morphology as a function of the growth temperature and X-ray diffraction was further employed in order to evaluate the crystallinity and the texturing of the deposited material. The experimental results achieved by Claeyssens and co-workers were eventually in good agreement with the observations made on the ZnO/sapphire(0001) system already considered [31].
However, it is worth noting that, in the previously considered literature works, only rather thick ZnO films have been successfully deposited on top of insulating substrates and hence it is not possible to speak about the formation of two-dimensional graphene-like ZnO.

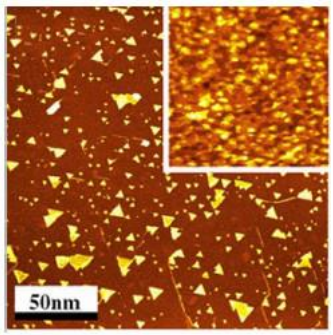

Figure 1.12: STM image (200 nm x 200 nm, V=1.6 V, I=0.5 nA) of 2.2 ML ZnO on Ag(111). The inset shows 3.2 ML on the same scale [33].

Indeed, the first experimental evidence of the ZnO graphitic-like phase was provided by Tusche *et al.* [33] in 2007. In their research activity, Tusche and co-workers have deposited ZnO on Ag(111) by means of PLD. In particular, the deposition was carried out at 300 K using a stoichiometric ZnO target, ablated at a rate of 0.10 ML/s under an oxygen background pressure of 5×10^{-7} mbar. After annealing up to 680 K, stoichiometric films were formed as verified by X-ray photoelectron spectroscopy (XPS). Figure 1.12 shows the surface morphology of the deposited film when the coverage is 2.2 ML, while the inset is related to a coverage of 3.2 ML, considering that 1 ML can be defined to correspond to the surface atomic density of the substrate surface. The structure of the grown material was determined using surface X-ray diffraction (SXRD): the first three layers of the film are characterized by a graphitic-like structure, while the wurtzite structure is restored

starting from the 4th layer. Finally, it is possible to observe that this structural transition takes place together with a relevant modification of the surface morphology of the film (inset of figure 1.12).

1.3 Characterization techniques

Once two-dimensional materials and nanostructures have been synthesized, they have to be investigated in order to evaluate their morphology, structure and degree of crystallinity, electronic and optical properties and so on. Indeed, characterization is necessary in order to determine whether the produced materials are able to fulfil all the requirements for the fabrication of working devices. For this purpose, a wide range of surface science techniques can be used to study the growth mechanism and the properties of 2D materials. The typical experimental approach is based on sample preparation and *in situ* characterization under ideal – i.e. ultra-high vacuum (UHV) – conditions, which means in a system characterized by a base pressure $<10^{-10}$ mbar.

Several characterization techniques are available nowadays and, for the sake of simplicity, it is useful to distinguish them on the basis of the type of information about the investigated materials and low-dimensional structures they can provide. First, there exist several characterization techniques able to investigate the structural properties of the material and this is the case of scanning tunneling microscopy (STM), atomic force microscopy (AFM), transmission electron microscopy (TEM), Raman spectroscopy, low-energy electron diffraction (LEED) and surface X-ray diffraction (SXRD). Secondly, spectroscopic techniques, such as scanning tunneling spectroscopy (STS), Auger electron spectroscopy (AES) and X-ray photoelectron spectroscopy (XPS), are able to investigate and characterize the electronic, optical, chemical and magnetic properties of the studied systems.

In reality, however, it is worth noting that a different subdivision of the characterization tools can be made. Indeed, it is possible to make a distinction between techniques providing spatially averaged information (such as LEED) and techniques allowing a local investigation of the sample surface (such as STM).

The experimental work presented in this thesis is mainly focused on the characterization of pulsed laser deposited 2D materials by means of a scanning tunneling microscope. Indeed, STM is a very powerful characterization tool being capable to image the surfaces under investigation with unprecedented spatial resolution, even down to the nanometer and atomic length scale, and useful in the investigation of non-periodic structural features, including defects and adsorbates. In addition, scanning tunneling spectroscopy (STS) has been employed in order to investigate the electronic properties of the studied systems, providing important information on the electronic local density of states (LDOS) of both occupied and empty energy levels around the Fermi energy. More details about scanning tunneling microscopy and spectroscopy, as well as about other characterization techniques used in this thesis work (for instance, Raman spectroscopy), will be given in sections 2.2 and 2.3.

In the following, literature works in which STM/STS have been exploited as characterization tools will be presented. In section 1.3.1 attention will be focused on MoS_2 deposited on top of a metallic substrate (Au(111) in particular), while section 1.3.2 is dedicated to the STM/STS characterization of ZnO on Au(111). Literature works in which STM/STS have been used to investigate silicene are not reported here because the experimental activity relative to silicon growth presented in this thesis is only preliminary and the achieved results are not comparable with those obtained by other researchers.

1.3.1 MoS_2 on Au(111): characterization by means of scanning tunneling microscopy (STM) and spectroscopy (STS)

In the literature, several experimental works regarding the STM/STS characterization of the MoS_2/Au(111) system can be found. Gold has been the material of choice in order to act as a substrate for the growth of molybdenum disulphide at the two-dimensional limit because of several different reasons. However, the most relevant one is that Au is one of the most commonly used contact metals in electronic devices due to

its high electrical conductivity and chemical inertness; thus, detailed analysis of the MoS_2/Au contact has been an important research field and it is also relevant for future device fabrication.
The first real space STM images of 2D single-layer MoS_2 nanostructures on top of Au(111) have been obtained by Helveg *et al.* [34] in 2000. In their experimental work, Helveg and co-workers have deposited MoS_2 exploiting reactive evaporation. Indeed, Mo has been deposited on the Au(111) surface (shown in figure 1.13(a) with its characteristic herringbone reconstruction (see [35] for more details)) using an e-beam evaporator, in an H_2S atmosphere of 10^{-6} mbar and at a temperature of 400 K; subsequently, an annealing is carried out at 673 K for 15 min while maintaining the H_2S background pressure in order to form crystalline MoS_2 nanoclusters.

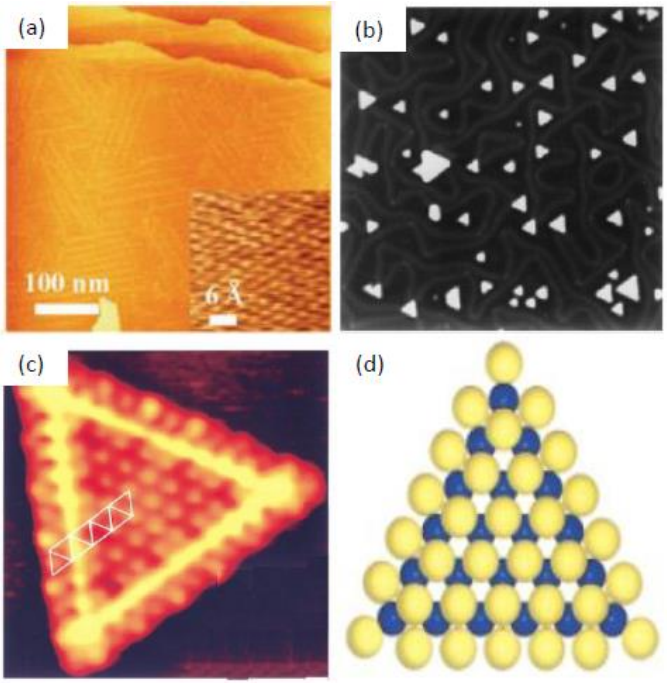

Figure 1.13: (a) Large-scale STM image of the Au(111) surface showing the characteristic herringbone reconstruction arising from the coexistence of face-centred cubic (fcc) and hexagonal close-packed (hcp) regions separated by ridges. The inset is a higher magnification image of the same surface [36]. (b) STM image (74.4 nm x 72.1 nm) of MoS_2 nanoclusters on Au(111). (c) Atomic-resolution STM image (4.1 nm x 4.2 nm, V=5.2 mV, I=1.28 nA) of a MoS_2 island in (b). (d) Model of the structure of the triangular clusters observed in the STM images (yellow = S, blue = Mo). The S edge atoms are out of registry with respect to the S atoms in the basal plane of MoS_2. Reproduced from [34].

As can be evaluated from the STM image in figure 1.13(b), the majority of the nanoclusters are characterized by a triangular shape (with a side length of ~30 Å and with an orientation that reflects the sixfold symmetry of the substrate) and they can be considered as one layer thick MoS_2 islands with the (0001) basal plane of the MoS_2 layer parallel to the underlying substrate. Figure 1.13(c) is an atomically resolved STM image of one of the triangular clusters present in figure 1.13(b): the protrusions are arranged with hexagonal symmetry and with an average interatomic spacing of 3.15 Å, which is exactly the interatomic distance between the S atoms in the (0001) basal plane of MoS_2, thus suggesting that only the sulphur atoms in the topmost S layer of MoS_2 are imaged in an STM measurement. This hypothesis has been also confirmed by theoretical calculations. Further information regarding the thickness and the structure of the deposited nanoclusters can be evaluated by scanning tunneling microscopy. Indeed, since the triangular-shaped islands in figure 1.13(b) have an apparent height of only 2 Å (in contrast with the interlayer spacing of 6.5 Å in bulk MoS_2), it is reasonable to conclude that the nanoclusters are present as single layers on the gold surface. Besides considering their morphological features, Helveg *et al.* [34] have also provided insight into the edge structure of the grown MoS_2 nanoclusters. In principle, the morphology of a MoS_2 island should be determined by two types of edge terminations, the so-called S-edge and Mo-edge. However, the fact that the nanoclusters are

characterized by a triangular rather than a hexagonal shape implies that one of the edge terminations is considerably more stable. At this point, supposing that the edge protrusions in figure 1.13(c) can be associated to S atoms, Helveg and co-workers concluded that the nanoclusters structure is that represented by the model in figure 1.13(d), considering that the yellow dots represent S atoms while the blue ones are Mo atoms.

Following the work done by Helveg and co-workers, Sørensen *et al.* [30] have explored the structural and electronic properties of single-layer MoS_2 synthesized on a single-crystal Au(111) surface by means of STM and STS. The deposition procedure was the same as in [34], except for the fact that the growth temperature was higher (873 K) in order to favour the formation of larger MoS_2 islands with a typical size of 10 – 50 nm and with truncated triangular or hexagonal shape (figure 1.14(a)). A peculiar characteristic of MoS_2 single layers is the periodic buckling observed as a hexagonal set of protrusions on the (0001) basal plane of the MoS_2 islands. This hexagonal lattice (clearly visible in the atomic-resolved STM image of figure 1.14(b)) is the so-called moiré pattern that arises due to the lattice mismatch between MoS_2 and the underlying Au(111) surface (around 9.3%) and that features a 3.28 nm periodicity and a rotation angle θ=5.2° between the superstructure spots and the lines of the MoS_2 lattice. More in detail, the moiré superstructure is related to the substrate and overlayer reciprocal lattice vectors by the following relationship: $\mathbf{k}_{moiré} = \mathbf{k}_{MoS2} - \mathbf{k}_{Au}$ (figure 1.14(c)), where the amplitude of the **k** vectors are given by $k = 4\pi/\sqrt{3}a_i$ and a_i are the real space lattice distances for the moiré pattern, the MoS_2 overlayer and the Au(111) surface, respectively. By considering a_{MoS2}=0.315 nm, a_{Au}=0.288 nm, $a_{moirè}$=3.28 nm and θ=5.2°, a rotation of ϕ=0.45° is obtained and this means that the MoS_2 close-packed rows are almost perfectly aligned with the Au(111) close-packed directions. Moreover, the formation of the moiré pattern is associated with a 100 pm out-of-plane corrugation of the otherwise planar MoS_2 layer, which can be measured by means of STM.

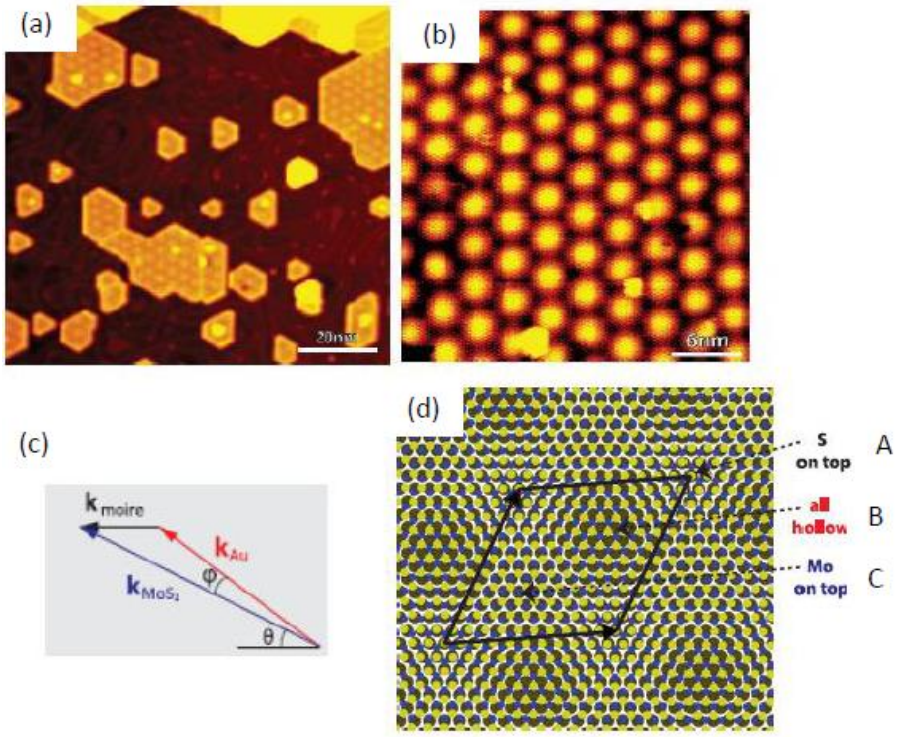

Figure 1.14: (a) Large-scale STM image (100 nm x 100 nm) of single-layer MoS_2 islands on Au(111). It is worth noting that the herringbone ridges seem to terminate at the perimeter of the nanoclusters or to avoid them. (b) Atomic-resolution STM image (30 nm x 30 nm, V=-1.25 V, I=0.61 nA) in which both the atomic structure and the moiré pattern are visible. (c) Relationship among the reciprocal lattice vectors of the MoS_2 overlayer, the gold substrate and the moiré superstructure. θ is the rotational angle between $\mathbf{k}_{MoS2}$ and $\mathbf{k}_{moirè}$ while ϕ is the angle relative to the rotation of $\mathbf{k}_{MoS2}$ with respect to $\mathbf{k}_{Au}$. (d) Model of the moiré superstructure of single-layer MoS_2 on Au(111). The ϕ angle is supposed to be 0.45°. A, B and C indicate the three distinct positional relationships that can coexist in the same moiré supercell. Reproduced from [30].

Figure 1.14(d) shows a model of the moiré superstructure of monolayer MoS_2 on Au(111). The model indicates the coexistence of three different positional relationships: S atoms in the lower layer of the S – Mo – S structure are placed at (A) the top sites of the Au atoms, (B) the hollow sites of the Au atoms and (C) the hollow sites of the Au atoms but with the Mo atoms that are located on top sites of the Au atoms. Considering that the S atoms on hollow sites (B and C) are closer to the Au(111) surface than the S atoms on top sites (A), the periodic bright regions observe in the moiré pattern correspond to the A region, whereas the very dark and dark zones are B and C regions, respectively [30]. However, it is worth mentioning that also electronic effects have to be taken into account when interpreting STM data as they can strongly affect the colour contrast in the STM images.

As regards the electronic properties of the MoS_2/Au(111) system, they have been investigated by means of scanning tunneling spectroscopy. The results of this spectroscopic analysis reveal that the interaction with the underlying gold surface leads to a modification of the band gap of MoS_2 and causes also a doping effect [30]. In the STS spectra of figure 1.15, differential conductance (dI/dV) curves are shown, considering that they represent to a first approximation the local density of states (LDOS) as a function of the energy near the Fermi level. Two important information can be extracted from these spectra. Indeed, a full band gap corresponding to dI/dV = 0 is absent while a region characterized by a low LDOS can be observed between -1 and +0.5 V, from which an energy gap of about 1.5 eV can be extrapolated (a value lower than the 1.8 eV value of the energy gap predicted for isolated single-layer MoS_2). These aspects are peculiarities of the MoS_2/Au(111) system and are related to a doping effect due to electron donation from the gold substrate to the MoS_2 sheets and resulting in a n-type behaviour of the semiconductor in contact with Au(111). A more precise explanation of the STS measurements results can be found in [37]. The increases in the LDOS that can be observed in figure 1.15 at negative voltages lower than -1 V and at positive voltages larger than +0.5 V correspond to occupied states in the valence band (VB) and to unoccupied states in the conduction band (CB), respectively [30].

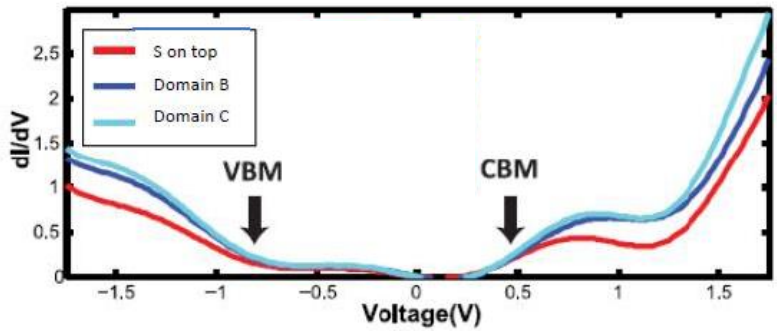

Figure 1.15: STS measurements on the MoS_2/Au(111) system. The curves are relative to three different regions of the moiré pattern showing a different colour contrast in the STM images and the arrows indicate the valence band maximum (VBM) and the conduction band minimum (CBM), respectively [30].

Even though both Helveg *et al.* [34] and Sørensen *et al.* [30] have only considered small MoS_2 islands, it would have been highly attractive to form more uniform and extended layers. According to Sørensen and co-workers [30], this is possible due to the fact that the MoS_2 sheets are coherent over Au(111) step edges. The only experimental problems to be overcome are the corrosive nature of the H_2S gas used during the deposition and the difficulty of fully covering the Au surface with MoS_2 due to the competition between the sulphide phase and Mo – Au alloy formation at high temperature.

Indeed, Grønborg and co-workers [38] managed to synthesize large area epitaxial single-layer MoS_2 on an Au(111) substrate by means of a reactive MBE process in an H_2S atmosphere. Their experimental work was carried out by repeating several times the same growth cycle (very similar to the deposition procedure followed in [34] and [30]) consisting in Mo deposition and annealing, which both take place under an H_2S background pressure of 10^{-7} mbar. The first growth cycle resulted in the formation of relatively large MoS_2

islands with truncated triangular or hexagonal shape and in a coverage of 0.3 ML (figure 1.16(a)). In order to increase the coverage of high-quality single-layer MoS_2, the growth cycle has been repeated resulting in islands merging together at a coverage of 0.6 ML (figure 1.16(b)). Finally, continued cycling of the growth process has led to a higher coverage of 0.8 ML (figure 1.16(c)) and the formation of a nearly continuous single layer of MoS_2 featuring the characteristic moiré pattern (shown in the atomic-resolution STM image of figure 1.16(d)).

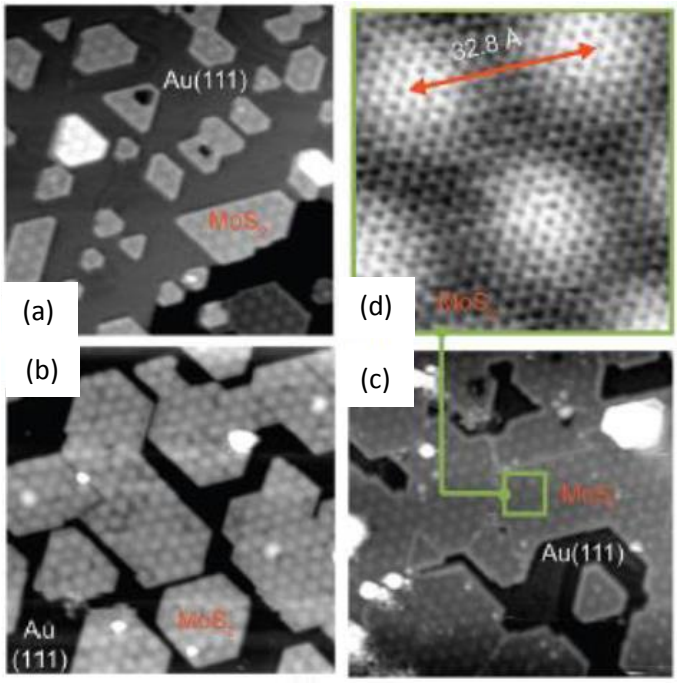

Figure 1.16: STM images (65 nm x 65 nm, V=-0.15 V, I=1.13 nA) of the MoS_2/Au(111) system acquired (a) after one growth cycle (coverage = 0.3 ML) and after having repeated the growth cycle leading to an increase of the coverage up to 0.6 ML (b) and 0.8 ML (c). (d) High-resolution STM image (6 nm x 6 nm, V=-0.15 V, I=1.13 nA) of the MoS_2 moiré pattern within the area marked by the green square in (c). Reproduced from [38].

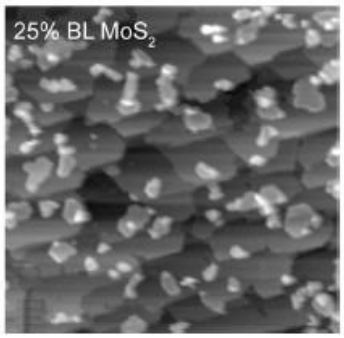

Figure 1.17: STM image (175 nm x 175 nm, V=-1.16 V, I=0.19 nA) of MoS_2 on Au(111) with an estimated coverage of 0.25 ML for bilayer MoS_2 [38].

Once a coverage of 0.8 ML was reached, Grønborg *et al.* [38] observed the formation and growth of regions of bilayer (BL) MoS_2 (see bright regions in figure 1.17). It is very interesting to note that BL MoS_2 islands are characterized by a different structure and a different morphology with respect to SL MoS_2 islands. Indeed, the surface of bilayer MoS_2 seems to be flat and the moiré pattern is absent while single-layer MoS_2 still shows a moiré pattern that is unaffected by the presence of the BL MoS_2 islands. Another important consideration is related to the thickness of these bilayer islands. The apparent height of BL MoS_2 relative to the underlying SL islands is 5.2 Å; this value is comparable to the interlayer spacing in bulk MoS_2 – i.e. 6.5 Å – thus confirming the fact that these new features are bilayer and not multilayer islands. Finally, it is worth

mentioning that the interaction between the second layer of BL MoS_2 and the underlying SL MoS_2 (due to weak van der Waals forces) is weaker than the interaction between single-layer MoS_2 and the gold surface. Furthermore, Grønborg and co-workers explained other important characteristics of the MoS_2/Au(111) system, in particular the lifting of the herringbone reconstruction [35] of the gold surface and the presence of peculiar line defects. The first feature can be seen in figure 1.18(a) where the MoS_2 islands that appear brighter than the rest (see the blue arrow in the image) have been demonstrated to grow on top of small lifted Au islands; indeed, the difference in the apparent height between the brighter and the darker MoS_2 islands has been found to be compatible with the height of a step of the gold surface (2.3 Å). Such small extra Au islands are expected to be generated by the lifting of the herringbone reconstruction that can be again observed in figure 1.18(a), where distortions of the regular herringbone reconstruction are present even after only one MoS_2 growth cycle. On the contrary, a line defect can be clearly seen in figure 1.18(b)-(c) and can be considered as a boundary between two MoS_2 islands characterized by the same edge type (either Mo-edges or S-edges) while joining islands through the meeting of two different edge types results in the formation of a continuous single-layer MoS_2.

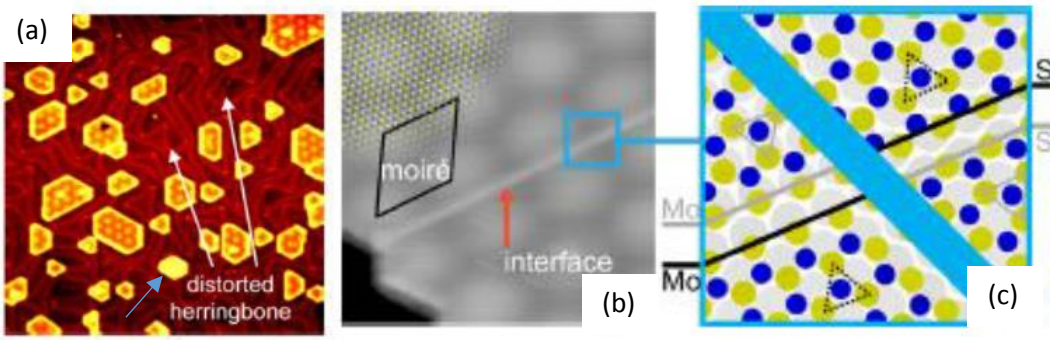

Figure 1.18: (a) STM image (100 nm x 100 nm, V=-1.25 V, I=0.65 nA) of the MoS_2/Au(111) surface after one growth cycle of MoS_2 in which the distortion of the otherwise regular herringbone reconstruction is visible. The blue arrow marks the presence of a MoS_2 island grown on top of a small lifted Au island characterized by exactly the same size and shape. (b) and (c) are the STM image (10 nm x 10 nm, V=-0.88 V, I=0.52 nA) and the schematic model of a line defect, respectively. Reproduced from [38].

Finally, the chemical stability of the deposited MoS_2 layers towards air exposure has been tested. It has been demonstrated that a few hours air exposure followed by a mild annealing to 500 K in ultra-high vacuum conditions (carried out to remove physisorbed chemical species) do not affect the quality of the deposited material [38]. This result suggests an inert character of single-layer MoS_2 towards an oxidizing gas, a property that can allow, for instance, the use of *ex situ* characterization techniques.
To summarize, literature works in which scanning tunneling microscopy and spectroscopy are used as characterization tools to investigate single-layer and bilayer MoS_2 deposited on top of an Au(111) substrate have been reported. It is worth noting that, in all the considered experimental activities, MoS_2 has been grown by means of reactive evaporation or chemical vapour deposition (CVD) and no attempt has been made to deposit two dimensional MoS_2 using pulsed laser deposition (PLD) and to study the resulting nanostructures using STM/STS. Finally, the last important aspect to be underlined is that the typical substrate for the deposition of MoS_2 is Au(111) and different substrates (like, for example, Ag(111)) have been used only rarely and, hence, can be the subject of deep and detailed investigations.

1.3.2 ZnO on Au(111): scanning tunneling microscopy (STM) and spectroscopy (STS) characterization

The most common method to synthesize graphene-like zinc oxide layers relies on the exploitation of molecular beam epitaxy, during which ZnO is grown on top of a metal substrate under ultra-high vacuum (UHV) conditions [39]. More in detail, metallic Zn is usually deposited on the metallic surface that acts as the substrate and it is oxidized either during a reactive evaporation process or after the Zn deposition has been concluded (post-oxidation), resulting in the formation of graphene-like ZnO. Different (111)-oriented metal

surfaces have been exploited to carry out the growth of zinc oxide at the two-dimensional limit, such as Ag(111) (see, for instance [33] and [40]) and Au(111). Often the UHV chamber where the deposition is carried out is equipped with a scanning tunneling microscope (STM) to enable the *in situ* characterization of the deposited material – i.e. determination of the crystal structure at the atomic scale, evaluation of the thickness and of the electronic properties of the grown nanostructures and so on. Before starting considering specific experimental works, it is important to note that 2D ZnO synthesis usually requires the presence of some kind of substrate leading to interactions between the ZnO layer and the substrate itself that can result in a modification of the properties of the deposited material [39]. Among all the possible substrates, the Au(111) surface is one of the most used because it shares the hexagonal symmetry with graphene-like ZnO, can be treated at sufficiently high temperatures and is rather inert towards O_2 and NO_2 – i.e. the main oxidizing species used during the fabrication of 2D ZnO.

In 2013, Stavale *et al.* [41] have analysed the growth of ZnO thin films on an Au(111) support by using STM. The deposition has been carried out by evaporating ZnO under an O_2 pressure of 5 x 10^{-5} mbar, depositing it onto a clean gold surface at room temperature and, finally, annealing the grown films to temperatures between 600 and 800 K while maintaining the same oxygen background pressure. First of all, Stavale and co-workers observed that, when depositing a small amount of material and annealing the sample at rather high temperature (> 750 K), isolated ZnO nanoclusters are formed. These structures (shown in figure 1.19(a)) are up to 6 nm in height, up to 20 nm in diameter and are characterized by a triangular or hexagonal shape.

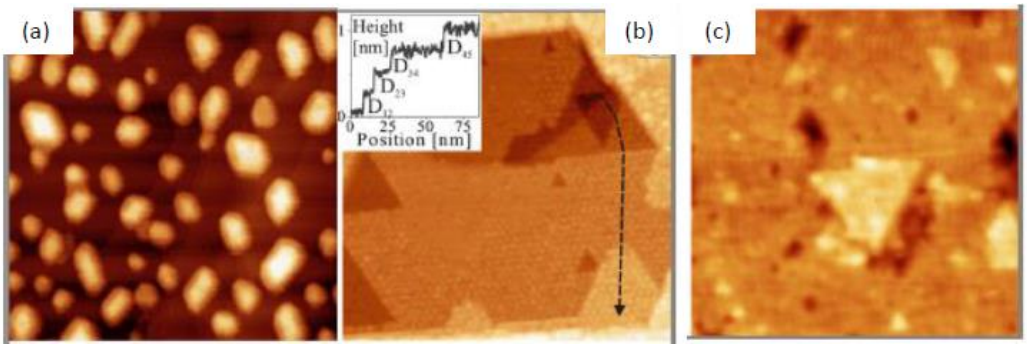

Figure 1.19: (a) STM image (160 nm x 160 nm, V=1.6 V) of ZnO islands on Au(111). (b) STM image (80 nm x 80 nm) of a ZnO thin film with a nominal thickness of 3 ML. The inset shows a height profile across the first four ZnO layers, with step height of 2.2 Å, 2.4 Å, 2.6 Å and 2.6 Å, respectively. (c) STM image (100 nm x 100 nm) of a 15 ML thick film on Au(111). The moiré pattern is no more visible on the surface of ZnO. Reproduced from [41].

Subsequently, by depositing more material and by performing the annealing treatment at a lower temperature, films that cover the entire Au(111) surface have been obtained and an example of a deposited film consisting in 1 - 2 ML can be observed in figure 1.19(b). The surface of this ZnO thin film features the presence of a moiré pattern, similar to the moiré superstructure observed for MoS_2 on Au(111) but with a lower periodicity of 2.2 nm and resulting from (7 x 7) ZnO(0001) unit cells overgrowing (8 x 8) cells of the unreconstructed Au(111) surface. Indeed, STM images of the ZnO/Au(111) system give no hint for the preservation of the herringbone reconstruction typical of the Au(111) surface and therefore suggest that the gold reconstruction is lifted during ZnO growth, a behaviour that has been observed also in the case of MoS_2 deposited on top of Au(111). Furthermore, by means of STM, Stavale *et al.* [41] demonstrated that the moiré pattern remains visible on the first four oxide layers with a constant in-plane periodicity and a constant corrugation of ~1 Å while the superstructure pattern disappears beyond the fourth layer (as can be seen in figure 1.19(c)). However, it is worth mentioning that the ZnO films remain perfectly crystalline, independently on the number of layers. Starting from the obtained experimental results, Stavale and co-workers have also proposed a structural model for the ZnO/Au(111) system and they have taken into account two factors influencing the oxide growth: the polarity of the (0001) wurtzite termination and the lattice mismatch between ZnO and the underlying Au(111) surface, that results in the formation of the moiré pattern. For the

issue of polarity compensation, two balancing effects have to be considered [41]. First, the oppositely charged planes (consisting of Zn^{2+} and O^{2-} ions, respectively) tend to reduce their mutual distance in order to minimize the associated dipole moment. Secondly, electron transfer between the oxide overlayer and the underlying metal substrate generates an interface dipole that causes an increase in the Zn – O interlayer distance. The combination of the two effects results in a situation in which the terminating plane is made of oxygen anions and the Zn – O layer distance is reduced (even though without reaching the zero value as in the case of the ZnO/Ag(111) system [33]). Indeed, the thickness of the first ZnO layer (2.2 Å) is lower than that of higher order layers (2.6 Å).
Finally, the electronic properties of the deposited oxide films have been investigated by means of scanning tunneling spectroscopy and the differential conductance (dI/dV) spectrum for a 15 ML thick ZnO film is displayed in figure 1.20. The band onsets occur at -2 and +0.8 V for the valence and the conduction band, respectively, thus resulting in a band gap of 2.8 eV – i.e. smaller than the bulk value of the band gap (3.4 eV). Moreover, the Fermi level is closer to the CB than to the VB and this finding reflects the strong n-type conductance behaviour of ZnO on top of Au(111) [41] (enhanced by the oxide/metal surface interaction and by the electron transfer occurring at the interface between ZnO and the gold substrate).

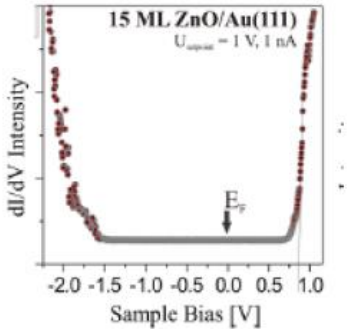

Figure 1.20: Differential conductance (dI/dV) spectrum taken on a 15 ML thick ZnO film with a 1.5 V set point bias [41].

In the same year, also Deng *et al.* [42] addressed the synthesis of single-layer and bilayer zinc oxide onto a gold substrate. The growth of ZnO on Au(111) was achieved by means of reactive evaporation, which means room temperature deposition of Zn under a 3 x 10^{-8} mbar pressure of NO_2 followed by an annealing at 550 K in ultra-high vacuum. Subsequently, STM measurements have been carried out at room temperature and in UHV conditions in order to follow the evolution of the ZnO morphology as the annealing time is increased.

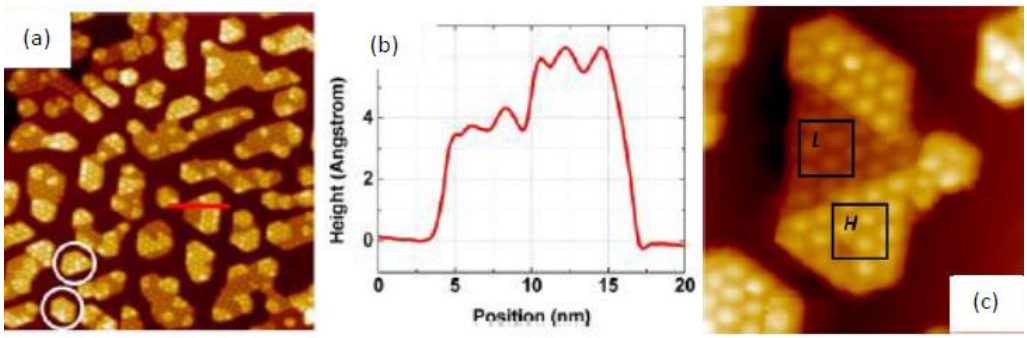

Figure 1.21: STM image (100 nm x 100 nm, V=1.5 V, I=5 pA) of ZnO deposited on Au(111) with an annealing treatment at 550 K for 5 min. The white circles highlight the presence of pure high-ZnO structures together with mixed low/high-ZnO ones. (b) Line profile along the red line in (a). (c) STM image (30 nm x 30 nm, V=1.5 V, I=5 pA) showing the moiré pattern on both the lower and the higher ZnO structures on Au(111). Reproduced from [42].

Figure 1.21(a) shows an STM image of the ZnO/Au(111) system annealed at 550 K for 5 min: two different types of ZnO nanostructures (characterized by a distinct height) can be observed on the gold substrate and they can be associated to monolayer and bilayer ZnO. Indeed, the height of the lower ZnO structure is ~3.5

Å, whereas the height of the higher ZnO structure is measured to be ~5.5 Å (as can be seen in the line profile of figure 1.21(b)). It is worth noting that the density of low-ZnO is larger than that of high-ZnO under these growth conditions and that a hexagonal moiré pattern with a periodicity of 2.3 nm can be seen on the surface of both structures (figure 1.21(c)). The observed moiré superstructure results from the lattice mismatch (around 12%) between the ZnO and the Au(111) lattices which are, however, aligned along the same direction (and not rotated one with respect to the other as in the MoS_2/Au(111) system). Moreover, it can be noted that both structures are characterized by a hexagonal unit cell with a lattice parameter of ~3.3 Å.
Deng and co-workers further discovered that the lower ZnO structures are gradually converted into higher ZnO structures upon annealing at 550 K for a longer period. For instance, the situation resulting from an annealing at 550 K for 30 min is shown in figure 1.22(a), in which also the size of the high-ZnO islands remarkably increases. Indeed, bilayer ZnO is energetically more favourable with respect to monolayer ZnO because the interaction energy between two ZnO layers is almost twice the interfacial adhesion energy between ZnO and Au, which interact only through weak van der Waals forces. After annealing at 550 K for 60 min (figure 1.22(b)), the higher ZnO structures are significantly more numerous than the lower ZnO ones (present with a percentage lower than 10%) while further annealing at 550 K (for instance, for 120 min) does not induce any significant modification in the oxide morphology, as can be observed in figure 1.22(c) and in the line profile in figure 1.22(d). Indeed, the thickness of high-ZnO is again ~5.5 Å and the moiré pattern is still present on the zinc oxide surface. However, it should be noted that annealing at higher temperature – i.e. 575 K – results in a quick loss of ZnO from the Au(111) surface and this is probably due to the thermal decomposition of ZnO at the annealing temperature or to the diffusion of ZnO into the bulk of the gold substrate.

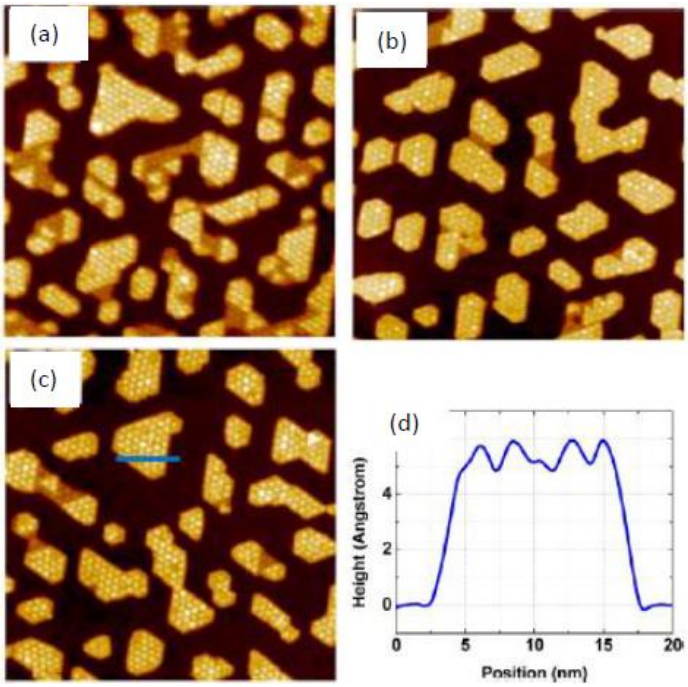

Figure 1.22: STM images (100 nm x 100 nm, V=1.5 V, I=5 pA) of ZnO grown on Au(111) using reactive deposition followed by annealing at 550 K for (a) 30 min, (b) 60 min and (c) 120 min. (d) Line profile along the blue line in (c). Reproduced from [42].

Deng *et al.* [42] have observed that the experimental STM images of the ZnO/Au(111) system could be acquired without any apparent influence of the tunneling bias and, in particular, from 1.5 to 0.2 V. This experimental finding reveals the metallization of 2D ZnO on top of Au(111) despite bulk zinc oxide being a wide-bandgap semiconductor. The metallic character of ZnO is due to the interaction with the Au substrate that, although relatively weak and related only to van der Waals forces, is sufficient to modify the electronic properties of the ZnO layer and to make it metallic. Finally, it is important to mention that Deng and co-

workers also managed to use the same deposition procedure in order to grow ZnO at higher coverage (~2 ML) to form continuous structures.

In order to gain more insight into the morphological and electronic properties of few-layer ZnO systems, the experimental work by Lee *et al.* [43] should be considered. Indeed, the researchers have demonstrated that the lattice constant and the electronic band gap of ultrathin ZnO can be tuned by simply controlling the number of layers present in the considered structures. In their experimental activity, ZnO has been grown by reactive deposition of Zn in a NO_2 atmosphere and has been studied by means of scanning tunneling microscopy and spectroscopy. First, attention will be focused on the morphological features – i.e. lattice constant and moiré periodicity – while in the following the tunability of the electronic properties and, in particular, of the energy gap with the number of layers will be addressed. As regards the morphological features, the results are summarized in the graph of figure 1.23(a) for ZnO structures ranging from monolayer ZnO to ZnO structures consisting of four layers. It can be noted that the in-plane lattice constant of 2D ZnO is expanded compared to that of the bulk wurtzite structure – i.e. 3.25 Å – and that the lattice constant as a function of the number of ZnO layers shows a maximum for bilayer zinc oxide and then decreases to almost the bulk value for structures with four layers. These observations reveal that there is an inverse relationship between the in-plane lattice constant and the thickness of the ZnO islands. A similar relationship can be also found between the periodicity of the moiré pattern and the lattice constant and can be justified by considering the definition of the moiré superstructure periodicity (based on the reciprocal lattice vectors of the substrate and the overlayer) and by assuming that the lattice constant of the Au(111) substrate does not change.

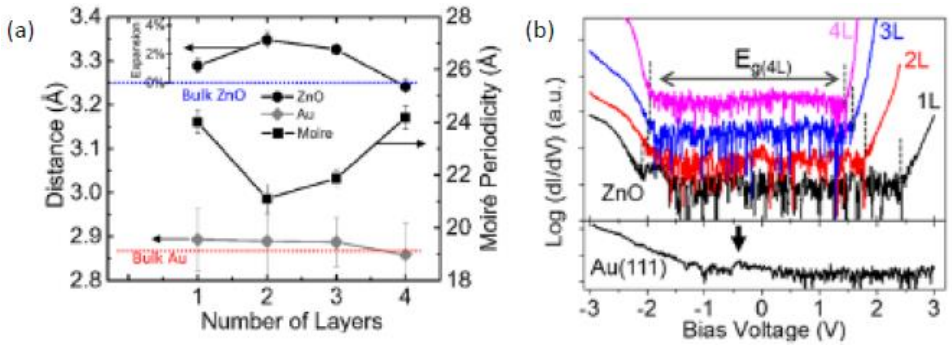

Figure 1.23: (a) ZnO lattice constant (filled circles, left axis) and moiré periodicity (filled squares, right axis) as a function of the number of ZnO layers. (b) Lower panel: dI/dV spectrum for the clean Au(111) surface. The spectrum is shown in logarithmic scale and the arrow indicates the surface state at V=-0.4 V. Upper panel: dI/dV spectra for each of the ZnO layers ($V_{setpoint}$=1 V, $I_{setpoint}$=50 pA). The spectra have been reported in logarithmic scale in order to better identify the valence and conduction band edges. Reproduced from [43].

The electronic properties of the fabricated ZnO layers have been investigated starting from the differential conductance (dI/dV) spectra in figure 1.23(b). The lower panel of figure 1.23(b) shows the dI/dV spectrum of the clean Au(111) surface in which the surface state peak at V=-0.4 V is clearly visible, while in the upper panel the dI/dV spectra relative to the different ZnO layers can be observed. Starting from these experimental results, Lee and co-workers managed to demonstrate that the band gap of the ZnO structures decreases as the number of layers increases, being 4.48 eV for monolayer ZnO and becoming very similar to the energy gap of bulk ZnO – i.e. 3.37 eV - for structures consisting of four layers. The reduction in the band gap with the number of layers is due to the fact that the conduction band minimum (CBM) decreases by as much as 1 eV while the valence band maximum (VBM) remains near V=-2 V independently on the number of layers. In conclusion, Lee *et al.* underlined the fact that the layer-specific electronic properties of ultrathin ZnO layers can be exploited in order to distinguish among these nanostructures that can be hardly identified unambiguously only on the basis of their apparent thickness. Indeed, the distinct electronic properties of the different layers can give a different colour contrast in the differential conductance (dI/dV) maps acquired by means of a scanning tunneling microscope (see section 2.2.2). An example is shown in figure 1.24(b)-(c): with

an applied bias V=3.2 V only monolayer ZnO is clearly visible, bilayer ZnO gives a very bright contrast at V=2.5 V and so on.

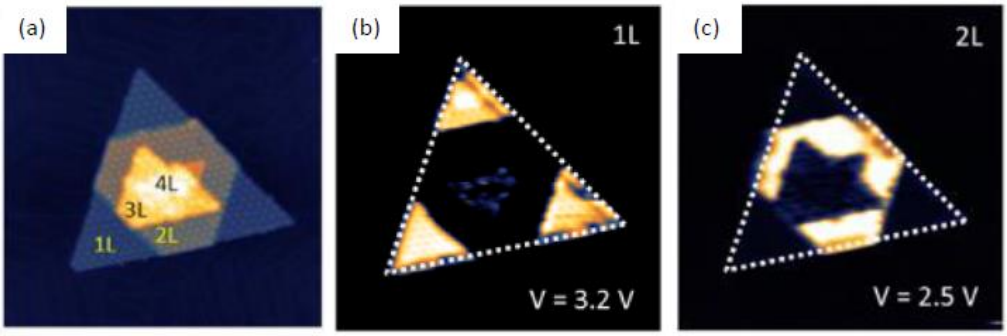

Figure 1.24: (a) STM image (82 nm x 82 nm, V=1.5 V, I=50 pA) of a ZnO structure on Au(111). (b) dI/dV map taken at V=3.2 V where a very bright signal from the first ZnO layer is observed. (c) dI/dV map taken at V=2.5 V where the bright contrast is given by bilayer ZnO. Reproduced from [43].

To summarize, literature works in which scanning tunneling microscopy and spectroscopy have been employed to characterized low-dimensional ZnO structures have been presented. However, as in the case of molybdenum disulphide, zinc oxide has been grown only exploiting reactive MBE or CVD. Thus, the combination of STM/STS as characterization techniques with different synthesis methods (such as pulsed laser deposition) has not been extensively explored yet.

1.4 Pulsed laser deposition (PLD) combined with scanning tunneling microscopy (STM) and spectroscopy (STS): synthesis and characterization of MoS_2 and ZnO on Au(111)

All the experimental works found in the literate and in which the researchers have carried out an atomic-scale investigation of two-dimensional materials and nanostructures by means of a STM analysis and STS measurements are based on the exploitation of chemical vapour deposition (CVD) and molecular beam epitaxy (MBE) as growth techniques. However, only little research activity has been dedicated to the employment of PLD as synthesis method and a scanning tunneling microscope as characterization tool and extensive experimental activities exploiting the combination of these two powerful techniques are still uncommon in spite of the several advantages that both PLD and STM/STS can provide. Indeed, PLD is a very peculiar and versatile synthesis technique that allows us to tune the morphology (and hence the electronic and optical properties) of the deposited structures in a very fine way and then STM/STS characterization provides the possibility to investigate them with an incredibly high spatial resolution, even down to the atomic scale. Driven by the peculiar and attractive features of PLD and STM/STS previously mentioned, this type of research activity has already been initiated in our laboratory, and, in particular, attention has been focused on two-dimensional MoS_2 [44] and ZnO [45] grown on top of Au(111) surfaces.
First, attention will be focused on the growth of MoS_2 on top of Au(111) starting from crystalline structures at the nanoscale and eventually obtaining large-area single-layer films that are very attractive for future applications. Then, the growth, surface structure and electronic properties of 2D ZnO deposited by means of PLD will be considered.

1.4.1 2D MoS_2 growth by pulsed laser deposition and its STM/STS characterization

In the experimental work by Tumino *et al*. [44], MoS_2 deposition has been performed in a PLD chamber kept at a base pressure of 5 x 10^{-9} mbar (hence in UHV conditions) by ablating a rotating MoS_2 target with a KrF excimer laser (wavelength: 248 nm, repetition rate: 1 pulse per second, pulse energy: 100 mJ, laser fluence:

0.5 - 1.5 J/cm^2). During the deposition process, the gold substrate has been kept at room temperature and placed 5 cm far from the ablated target. Then, the samples underwent a thermal treatment at temperatures ranging from 500 to 810 K, by maintaining the samples in ultra-high vacuum and by keeping the temperature constant for 30 min. STM/STS measurements have been performed at room temperature in order to investigate the grown structures.

The first part of the experimental activity has been dedicated to the growth and investigation of nanosized MoS_2 crystals deposited by using 20 laser pulses and subsequently annealed at various temperatures in order to evaluate the effect of the thermal treatment on the morphology of the deposited material. Immediately after PLD and before the annealing treatment, the substrate appears to be covered by a nanostructured film having a disordered surface morphology (figure 1.25(a)). However, when the thermal treatment is carried out in the temperature range 560 - 640 K, an organization of the deposited material can be observed, resulting in the formation of triangular islands with an average size of ~3 Å (figure 1.25(b)).

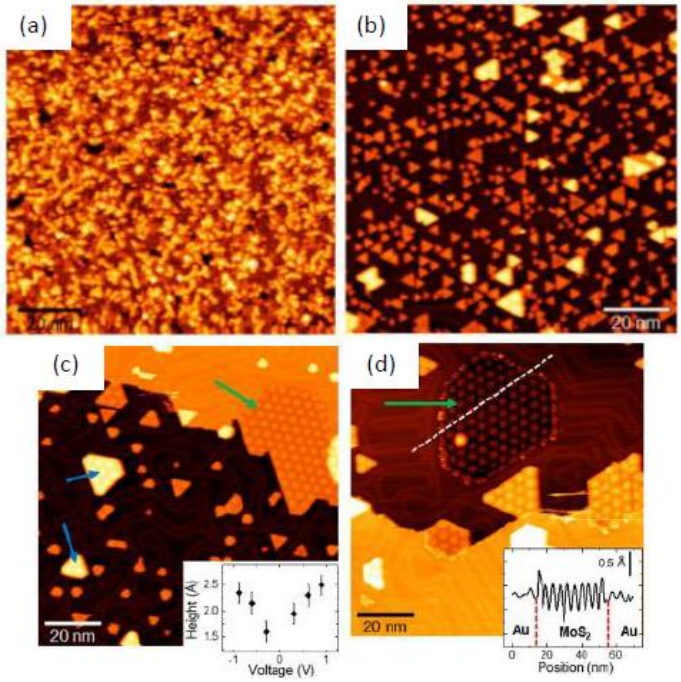

Figure 1.25: (a) STM image (100 nm x 100 nm, V=1.93 V, I=0.5 nA) of as-deposited MoS_2 on top of the Au(111) surface. (b) STM image (100 nm x 100 nm, V=0.5 V, I=0.4 nA) of the sample obtained after PLD and annealing at 640 K. (c) STM image (100 nm x 100 nm, V=1 V, I=0.4 nA) of the sample obtained after PLD and annealing at 720 K. The blue arrows indicate single-layer MoS_2 islands growing on top pf a small lifted gold terrace whereas the green arrow marks the presence of a rather large MoS_2 nanocrystal attached to the Au step edge. The inset shows the variation in the apparent height of the single-layer MoS_2 islands as a function of the applied bias voltage. (d) STM image (100 nm x 100 nm, V=1.2 V, I=0.3 nA) of MoS_2 on Au(111) subjected to a thermal treatment at 810 K. The green arrow indicates the presence of a partially embedded MoS_2 island and the inset shows the line profile along the white dashed line. Reproduced from [44].

Finally, when the annealing temperature is set around 700 K isolated MoS_2 islands with a well-defined geometry and surface morphology can be observed on top of the Au(111) surface, together with larger crystals which are characterized by a size of the order of tens of nanometers and grow attached to the gold step edges (indicated by the green arrow in figure 1.25(c)). In the samples annealed at high temperature, some peculiar features can be identified such as, for instance, the presence of brighter islands (see blue arrows in figure 1.25(c)) that are very similar to those observed by Grønborg and co-workers [38] and can be described as single-layer MoS_2 islands growing on top of small lifted Au terraces having exactly the same size and shape of the overlying MoS_2 crystals. Scanning tunneling microscopy can be also exploited to measure the thickness of the MoS_2 islands even though it is important to remember that the topographic information provided by STM is affected by the surface electronic properties and hence the measured height generally

depends on the applied bias. Indeed, as can be observed in the inset of figure 1.25(c), the thickness of single-layer MoS_2 can range from 2.5 to 1.6 Å as the applied voltage is varied in the range 1 - 0 V [44]. However, this measured thickness is significantly lower than both the interlayer distance of bulk MoS_2 – i.e. 6.15 Å – and the thickness of single-layer MoS_2 on top of other substrates – i.e. 6.7 Å on graphite. The reduced thickness of monolayer MoS_2 on Au(111) can be due to a stronger interaction between the gold substrate and MoS_2 itself or the formation of an interface tunneling barrier causing a lowering in the tip-sample tunneling conductivity.
By investigating the effect of the annealing treatment, Tumino and co-workers have also discovered that higher temperatures of the thermal treatment can favour the formation of single-layer MoS_2 islands partially embedded into the surface layer of the gold substrate [44]. An example of these peculiar structures can be observed in figure 1.25(d) and be considered as a MoS_2 nanocrystal growing on top of a one-step lower Au patch with respect to the surrounding gold terrace. This interpretation is supported by the line profile in the inset of figure 1.25(d) which shows that the partially embedded MoS_2 island and the surrounding Au terrace are approximately at the same level. In conclusion, it is relevant to underline that the growth of partially embedded structures leads to the formation of in-plane MoS_2/Au contacts, whose investigation can provide important information for the fabrication of the so-called lateral heterostructures and future working devices.

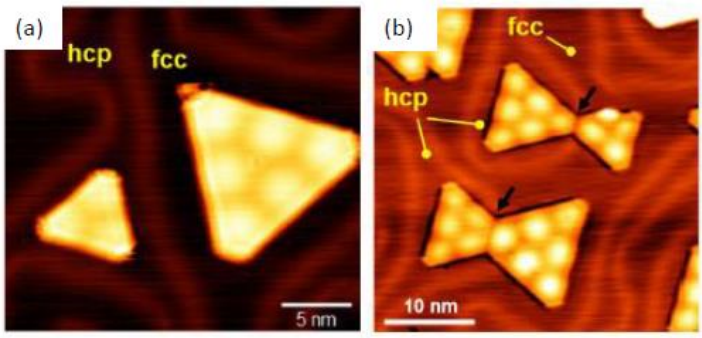

Figure 1.26: (a) STM image (V=0.6 V, I=1 nA) of two oppositely oriented MoS_2 triangular islands. The left MoS_2 nanocrystal grows on the hcp region of the Au herringbone reconstruction, while the right one lies on top of the fcc region. (b) STM image (V=1 V, I=0.3 nA) showing two oppositely oriented MoS_2 triangular islands merging together and forming 60° domain boundaries. Reproduced from [44].

Furthermore, by acquiring higher-resolution STM images, the researchers have investigated the atomic scale properties of the MoS_2 nanocrystals. As already mentioned, the MoS_2 islands formed during the previously described deposition process are characterized by a predominantly triangular shape (sometimes showing truncated corners) and feature the characteristic moiré pattern. Tumino *et al*. [44] have observed that the MoS_2 crystals grow on either fcc or hcp domains (see [35] for more details), thus causing distortions of the otherwise regular herringbone reconstruction of the gold substrate. Moreover, as can be seen in figure 1.26(a), triangular islands lying on different stacking regions show an opposite orientation, probably due to a strong interaction between the Mo atoms of the overlayer and the gold substrate causing a correlation between the MoS_2 lattice orientation and the substrate stacking configuration, and occasionally they can merge together, forming 60° domain boundaries, as shown in figure 1.26(b).
On the contrary, the second part of the experimental activity reported in [44] is dedicated to the growth of large-area single-layer MoS_2 films that are surely more attractive than isolated nanocrystals for the consideration of 2D MoS_2 future applications. In order to obtain a monolayer structure covering almost all the gold surface, two different approaches have been explored. The first one consists in repeating the same growth cycle – i.e. pulsed laser deposition and annealing – up to five times gradually extending the coverage up to 0.9 ML, whereas in the second one an almost complete MoS_2 monolayer has been deposited by carrying out a single growth cycle with optimized deposition parameters (figure 1.27(a)-(b)).

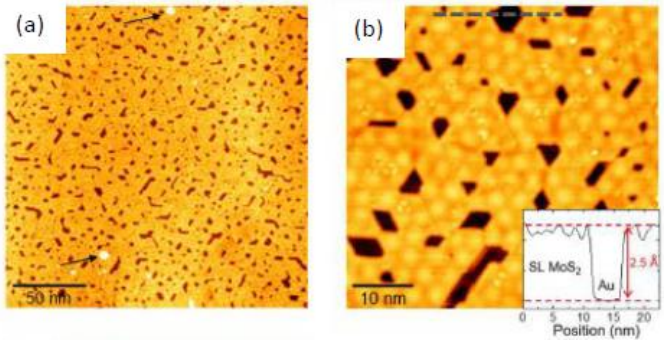

Figure 1.27: 200 nm x 200 nm (a) and 100 nm x 100 nm (b) STM images of a continuous film of monolayer MoS_2 grown on top of Au(111) by means of a single growth cycle [44]. The inset shows the line profile along the grey dashed line in (b) and demonstrates the formation of one single MoS_2 layer.

Scanning tunneling spectroscopy measurements have been carried out in order to characterize the electronic properties of the 2D structures on top of Au(111). The results are shown in the differential conductance (dI/dV) spectrum of figure 1.28. Several information can be extrapolated from the analysis of this spectrum [44]. First, an electronic band gap of approximately 2 eV results from the fact that the valence band and the conduction band edges occur at -1.5 eV and 0.5 eV, respectively. Second, a slight metallization of the deposited material can be recognized by observing the non-zero tunneling conductivity in the energy gap region. Third, MoS_2 on top of Au(111) seems to be characterized by a n-type character due to charge transfer phenomena occurring at the interface between the overlayer and the underlying gold substrate and resulting in the pinning of the Fermi level near the conduction band edge. All these peculiar features are hints of the role of the substrate in modifying the properties of the MoS_2 overlayer and further investigation of the change in the optical and electronic properties of MoS_2 on top of Au(111) have been also investigated by means of *ex situ* Raman and photoluminescence spectroscopies (see [44] for more details).

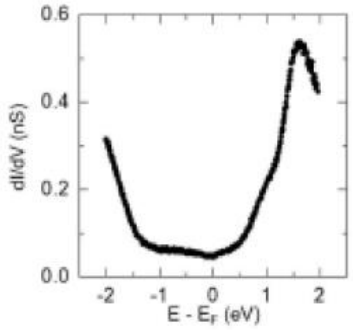

Figure 1.28: STS spectrum of single-layer MoS_2 on top of Au(111) [44].

1.4.2 2D ZnO grown by pulsed laser deposition and characterized by STM and STS

The experimental activity by Tumino *et al.* [45] has been focused on the growth of two-dimensional ZnO by PLD and on the subsequent characterization of its morphological, structural and electronic properties by means of *in situ* scanning tunneling microscopy (STM) and spectroscopy (STS). More specifically, the deposition has been carried out using a stoichiometric ZnO target and a KrF excimer laser emitting 20 ns pulses with a wavelength of 248 nm and a laser fluence of 0.5 J/cm^2. During the deposition, the substrate has been kept 5 cm far from the target and at room temperature and an oxygen background pressure of 5 x 10^{-3} mbar has been maintained in order to minimize the possibility of having oxygen deficiency in the deposited material. Once the ablated material has been deposited on top of the gold substrate, the samples have been subjected to a two-step thermal treatment consisting in a first annealing at 540 K for 20 min in O_2 atmosphere (5 x 10^{-6} mbar) followed by an additional annealing at 570 K in UHV conditions that is performed in order to

favour the desorption of the oxygen in excess. The as-produced samples are then characterized by performing room temperature STM and STS measurements.

As for the morphological and structural properties, Tumino *et al.* [45] have investigated the growth of ZnO nanostructures by gradually increasing the number of laser pulses from 1 to 20; the evolution of the ZnO/Au(111) system can be observed in the images of figure 1.29. After one laser pulse (figure 1.29(a)), two types of nanocrystals are formed on the gold surface: the hexagonal islands (indicated by the green arrow in figure 1.29(a)) are present in a larger amount and are characterized by a thickness of ~3.7 Å, while the smaller triangular crystals (see red arrows in figure 1.29(a)) are less numerous and only ~2 Å thick. Considering that the interlayer spacing in graphene-like ZnO is estimated to be 2 - 2.5 Å, triangular and hexagonal nanocrystals can be associated to monolayer and bilayer ZnO, respectively. For two (figure 1.29(b)) and four laser pulses, only bilayer islands are formed revealing the 2D ZnO preference of forming bilayer structures rather than wetting the gold surface, a behaviour that is probably driven by the much higher ZnO interlayer interaction energy with respect to the interfacial energy between zinc oxide and Au(111) [42]. After six laser pulses (figure 1.29(c)), the hexagonal bilayer islands start to coalesce and the ZnO third layer begins to appear (see the blue circle in figure 1.29(c)), while by increasing again the number of laser pulses, the third layer expands (figure 1.29(d)) and the growth of the fourth (figure 1.29(e)) and fifth (figure 1.29(f)) layers starts.

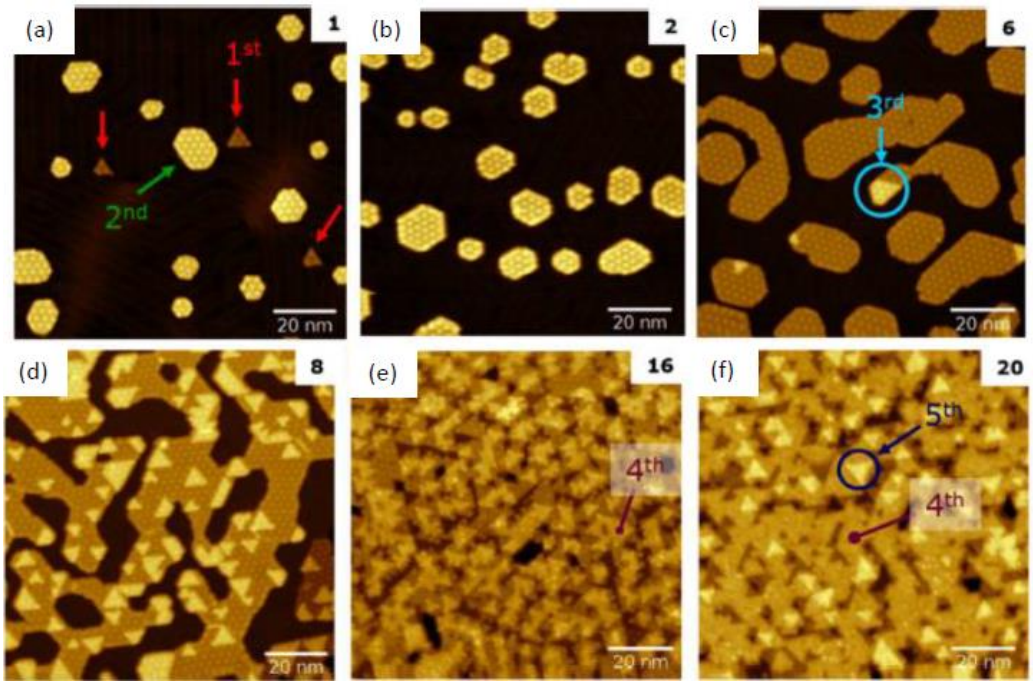

Figure 1.29: STM images (100 nm x 100 nm, V=2.5 V, I=1 nA) showing the growth of ZnO nanostructures by carrying out the deposition with an increasing number of laser pulses: (a) 1, (b) 2, (c) 6, (d) 8, (e) 16 and (f) 20. Reproduced from [45].

By acquiring and analysing high-resolution STM images, the researchers have noticed that monolayer and bilayer ZnO feature the moiré pattern characteristic of 2D ZnO on Au(111) and having a periodicity of 2.2 nm. However, while the third layer is characterized by the same moiré superstructure, the surface morphology dramatically changes starting from the fourth layer that does not exhibit the moiré pattern anymore. This structural modification can be associated to a transition from the graphene-like phase (stable only for a very low thickness of the deposited material) to the bulk wurtzite structure [45].

In order to characterized the electronic properties of the ZnO/Au(111) system, STS measurements have been performed and the resulting dI/dV spectra are shown in figure 1.30(a). The Au(111) spectrum features the characteristic Shockley state at -0.5 V. The differential conductance spectrum of ZnO single-layer is very similar to the gold one, while the spectrum of bilayer ZnO is characterized by a sharp increase in conductivity at 2.5 V, which can be taken as the onset of the ZnO conduction band. This modification of the STS spectrum

can be explained considering the penetration of the Au electronic wavefunction across the gap region of ZnO that is more relevant for monolayer than for bilayer ZnO due to the gradual increase in the STM tip – Au distance as the thickness of the ZnO layer increases [45]. The spectra related to the third, fourth and fifth ZnO layers exhibit a typical semiconducting behaviour with a zero-conductivity gap region.

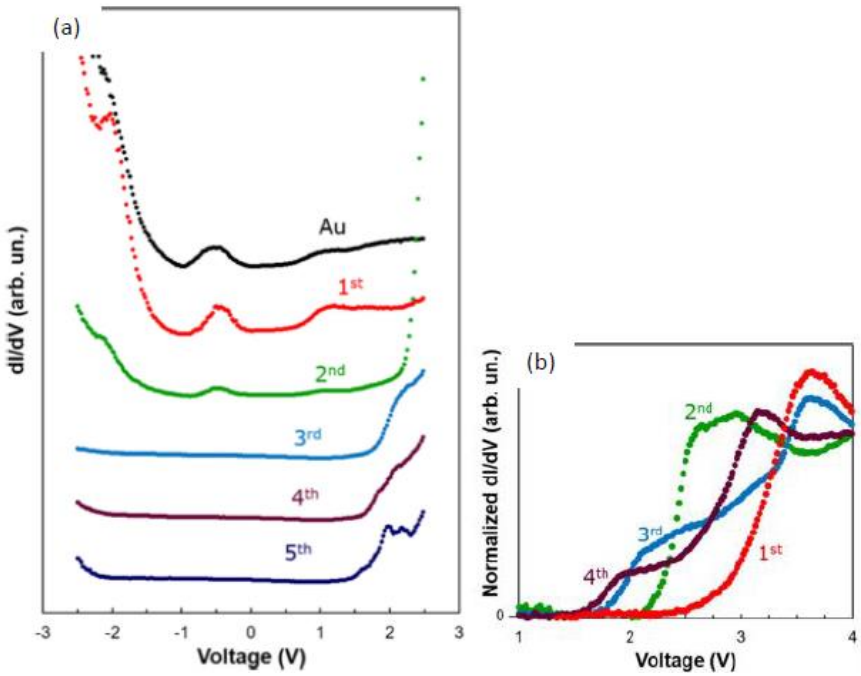

Figure 1.30: (a) Differential conductance (dI/dV) spectra of Au(111) and different ZnO layers ($V_{setpoint}$=2.5 V, $I_{setpoint}$=1 nA). (b) Normalized dI/dV spectra in the range 1 - 4 V ($V_{setpoint}$=4 V, $I_{setpoint}$=1 nA). Reproduced from [45].

Eventually, in order to further investigate the energy range where the onset of the conduction band takes place, STS spectra have been acquired in the 1 - 4 V range (figure 1.30(b)) and two peculiar features have been observed. On one hand, the onset of the ZnO conduction band occurs at increasingly lower voltages as the ZnO thickness increases, resulting in a decrease of the energy gap as the number of layers increases. On the other hand, a staircase-like behaviour of the STS curve (and hence of the electronic density of states) can be observed and can be due to 2D quantum confinement in the ZnO layers [45].

1.5 Objectives of this work

The previous discussion on pulsed laser deposition and STM/STS characterization of two-dimensional semiconducting materials allows us to outline the objectives of this thesis work.

First of all, it is important to underline that the combination of PLD and characterization by means of scanning tunneling microscopy (STM) and spectroscopy (STS) represents a novel experimental approach that has been exploited only marginally despite the fact that it is able to offer several advantages. Thus, an experimental activity combining PLD and STM/STS is already a novelty that can fill a gap present in the literature. Indeed, exploiting this peculiar experimental procedure and relying on the experimental findings resulting from the research activity already carried out in our laboratory, this work is focused on the development of the acquired knowledge in order to explore the possibility of combining different 2D materials and fabricating heterostructures and of studying the growth of 2D MoS_2 on top of different substrates, such as Ag(111). As side activity, a preliminary experimental research regarding the pulsed laser deposition of silicene - a route that has never been followed for the growth of 2D silicon – has been also carried out, even though further investigation is surely required. This because, traditionally, silicene has been synthesized using different techniques, such as evaporation. Pulsed laser deposition has never been employed for this purpose and it

would be interesting to exploit this deposition method to attempt to grow silicene on top of Ag(111) – i.e. the typical metallic substrate used as a support for graphene-like silicon – and Au(111), which represents the traditional substrate employed in electronic applications.
More in detail, the main objectives of this thesis work can be summarized in the following list.

- Fabrication of MoS_2/ZnO heterostructures by means of pulsed laser deposition (PLD):
  Vertical and lateral heterostructures represent the next research step for the exploitation of 2D materials in real and working devices, such as field-effect transistors (FETs) and photovoltaic applications. Traditionally, heterostructures based on two-dimensional materials have been fabricated by means of micromechanical exfoliation and subsequent stacking of the single layers one on top pf the other or by directly growing one material on top of the other by means of molecular beam epitaxy (MBE). However, heterostructures fabrication by means of PLD has not been addressed in detail and it would be intriguing to apply the PLD + STM/STS experimental approach to the production and characterization of these systems. Moreover, it would be interesting to investigate the coupling of MoS_2 and ZnO that can be easily deposited on top of the same substrate by means of PLD. In reality, as the synthesis conditions of the two material are slightly different (especially as regards the temperature of the annealing treatment), the fabrication of MoS_2/ZnO heterostructures on top of Au(111) has been addressed following two strategies. The first one is based on the growth of 2D ZnO followed by the deposition of MoS_2, while the second one relies on an opposite experimental procedure during which MoS_2 is deposited first and then ZnO is grown on top of the same gold substrate.

- Production and characterization of 2D MoS_2 on Ag(111):
  Pulsed laser deposition and STM/STS characterization of two-dimensional MoS_2 on top of Au(111) has been extensively investigated in our laboratory. However, it would be interesting to synthesize MoS_2 on other metallic substrates (such as Ag(111)) by means of PLD and to characterize the obtained structures using a scanning tunneling microscope. Indeed, such an analysis can help to understand the interaction of 2D MoS_2 with the underlying substrate and to address the modification of the MoS_2 morphological, structural, electronic and optical properties induced by the presence of the substrate itself.

Chapter 2

Experimental methods

The experimental work presented in this thesis is mainly based on the growth of two-dimensional semiconducting materials on top of metallic substrates by means of pulsed laser deposition (PLD) and on the characterization of the obtained structures using scanning tunneling microscopy (STM) and spectroscopy (STS). PLD is a very versatile deposition technique that allows us to deposit the ablated material on large areas (in the order of cm^2) and to finely control both the morphology and the thickness of the grown structures by simply tuning the processing parameters. The combination of PLD and STM/STS is a very desirable experimental procedure to deeply investigate 2D materials and nanostructures. Indeed, scanning tunneling microscopy and spectroscopy belong to the family of scanning probe techniques that are fundamental tools for the investigation of surfaces at the nanometer scale. In particular, STM and STS allow us to observe the morphology, the structure and the electronic properties of a material or a nanostructure in a local way and with incredibly high spatial resolution, even down to the nanometer and atomic scale. This chapter is aimed at introducing the synthesis and characterization techniques used during our experimental activity. Section 2.1 is dedicated to pulsed laser deposition: its working principle and the physical phenomena occurring during the ablation of the target and the condensation of the vaporized material on top of the substrate are explained in detail. In section 2.2 attention will be focused on STM and STS, whose theoretical and experimental concepts are outlined, and in section 2.3 a brief explanation of other used characterization techniques (such as Auger electron spectroscopy and Raman and photoluminescence spectroscopies) is given.

2.1 Pulsed laser deposition (PLD)

Pulsed laser deposition is a physical vapour deposition (PVD) technique based on the production of a plasma from a material target irradiated by intense laser pulses [46]. PLD has demonstrated a great versatility for the production of a wide range of materials such as metals, ceramics, oxides, semiconductors, polymers and biomolecules in the form of thin films and it has also proven to be a powerful method for the deposition of materials characterized by a complex stoichiometry. In addition, PLD offers the possibility to synthesize nanostructured materials with tailored physical and chemical properties through a fine tuning of morphology and structure down to the nanoscale, opening the way for the design of materials with enhanced performances or novel properties and suitable for specific applications. In the following, a description of the experimental apparatus and an insight into the physical phenomena occurring during the deposition process will be given.

Pulsed laser deposition is a growth technique exploiting the use of a pulsed laser source emitting nanosecond laser pulses and the very peculiar interaction between the high-energy laser pulses and the solid target to be ablated [47]. More in detail, the intense laser pulses are focused onto the solid target (placed inside a vacuum chamber) and they are partially absorbed. As a consequence, the target material is vaporized, a plasma plume is generated and the material from the plume is then allowed to condense on a substrate, placed a few centimetres far from the target. The growth process can also involve the use of a background gas that can be inert or reactive and that can affect the expansion of the plasma plume or the reactions occurring at the substrate surface.

The typical scheme of a PLD apparatus is shown in figure 2.1 and consists in a vacuum chamber containing the target material and the substrate, a laser source and an optical path constituted by mirrors, lenses and a

viewport that are necessary in order to focus the laser pulses on the target material inside the chamber [46]. As regards the deposition chamber, the PLD process is performed inside a stainless steel chamber equipped with a pumping system consisting of a gas inlet system and a primary pump and a turbomolecular pump that are necessary to maintain ultra-high vacuum (UHV) conditions or a controlled background atmosphere inside the chamber itself. The target material is mounted on a carousel capable to host simultaneously four different disk-shaped targets and to rotate around the vertical axis. This rotational movement allows us to select the desired target by properly placing it along the trajectory of the incident laser beam and it is also needed for keeping the target under rotation during the deposition process in order to guarantee a uniform ablation of the target itself. As for the substrate, it is placed in front of the target and its position can be controlled by electronic motors allowing to set a specific target-substrate distance and to control the position of the sample with respect to the plasma plume. During all the deposition processes carried out in the experimental activity presented in this thesis work, the target-substrate distance has been maintained constant and equal to ~5 cm.

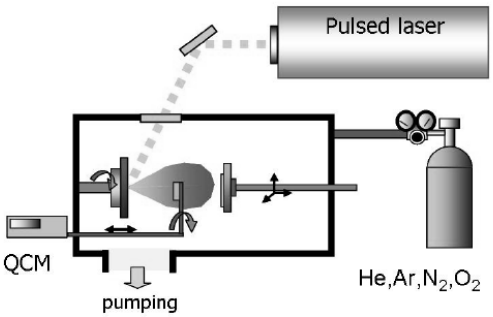

Figure 2.1: Scheme of the pulsed laser deposition apparatus [46].

The radiation source is a KrF excimer laser, emitting laser pulses characterized by a wavelength of 248 nm – i.e. in the UV range. Excimer lasers exploit the formation of unstable molecules, usually generated by the bonding between a noble gas and a halogen, such as krypton (Kr) and fluorine (F). Indeed, noble gases can form bound molecules with halogens, even though these molecules can exist only temporarily and only if the noble gas atoms are in an excited state – i.e. induced by an electrical discharge. Once formed, the excited compounds can release the excess energy by undergoing spontaneous or stimulated emission, resulting in strongly repulsive ground state molecules that dissociate back into two unbound atoms. The laser pulse duration is ~10 - 20 ns. The pulse energy can be set up to 400 mJ and the maximum repetition rate is 200 Hz, even if an energy of 50 - 100 mJ and a repetition rate of 1 pulse per second are typically used in the deposition processes described in this work. The emitted laser pulses follow an optical path composed by two mirrors and a focusing lens, the latter placed just before the quartz window through which the beam enters the UHV chamber and necessary in order to reduce the laser spot size on the target, thus increasing the laser fluence – i.e. the energy per unit area.

Finally, it is worth mentioning that the used PLD apparatus is directly connected, by means of magnetically coupled transfer probes, to a chamber for sample preparation where surface cleaning, annealing treatments and Auger electron spectroscopy (AES) measurements can be performed and to a UHV analysis chamber equipped with a commercial scanning tunneling microscope for variable-temperature STM/STS measurements. Therefore, this system makes possible to perform both the PLD process and the characterization of the deposited material *in situ* and, hence, under UHV conditions.

After having briefly described the experimental apparatus, the physical mechanisms involved in pulsed laser deposition can be considered. The most important physical phenomena in PLD are the coupling of the electromagnetic radiation with the condensed matter, the subsequent production of a plasma, its expansion away from the target and its recondensation on top of a substrate. However, it is necessary to underline that

these physical processes are highly complex and interrelated and depend not only on the laser pulse parameters but also on the target material [47].

The first physical phenomenon to be taken into account is light-matter interaction that results in the formation of a plasma plume expanding from the target surface towards the substrate. In traditional PLD processes, laser pulses in the 10 - 20 ns range are able to transfer to the target a power in the order of 10 - 100 MW, corresponding to a laser fluence of 1 - 10 J/cm^2 [46]. Under these conditions, the electric field generated inside the target material is in the order of 10^5 V/cm, a value that is sufficient to cause a dielectric breakdown in the material [46] and hence the vaporization of the target itself, thus resulting in the formation of a plasma – i.e. an hot ionized gas consisting of approximately equal numbers of positively charged ions and negatively charged electrons. Another important aspect to be underlined is that, in the case of nanosecond laser pulses, the ablation mechanism is mainly a thermal one as the energy is transferred to the target in a time scale longer than the typical time scale for the electron-phonon interaction – i.e. in the ps range. Moreover, since plasma expansion starts while the laser pulse is still impinging on the surface of the target, a shielding effect takes place due to the fact that the plasma itself partially absorbs the energy of the laser pulse. In such conditions, the laser-matter interaction and, in particular, the ablation depth are determined by both the thermal diffusion length and the optical penetration depth of the target material, affecting the amount of ablated material and hence the deposition rate [46].

The second relevant physical process occurring during pulsed laser deposition is the expansion of the plasma plume towards the substrate, a phenomenon that is very much affected by the background atmosphere and pressure. Indeed, three different situations can be distinguished and analysed (see figure 2.2 for a schematic representation) [46]. Under ultra-high vacuum conditions (base pressure <10^{-10} mbar), plasma plume expansion takes place almost without any collision between the ablated species and hence highly energetic atoms (with energies of tens of eV) impinge on the substrate, resulting in the deposition of compact films and in a strong adhesion between the substrate and the deposited material. On the contrary, when an inert background gas is injected into the deposition chamber, the plasma expansion dynamics is characterized by several collisions among the ablated species, the ablation plume is spatially confined and this spatial confinement favours clusters nucleation in the gas phase. These clusters can then diffuse in the background gas decreasing their kinetic energy and they can deposit on top of the substrate producing a cluster-assembled material in which the clusters maintain, at least partially, their structure and properties. Finally, if PLD is carried out under a reactive atmosphere, the chemical composition of the clusters can be modified by the interaction with the surrounding gas phase allowing to deposit a material with a controlled chemical composition. This last approach can be used, for instance, in order to grow metal oxide films and nanostructures by ablating a metallic target in an O_2 background atmosphere.

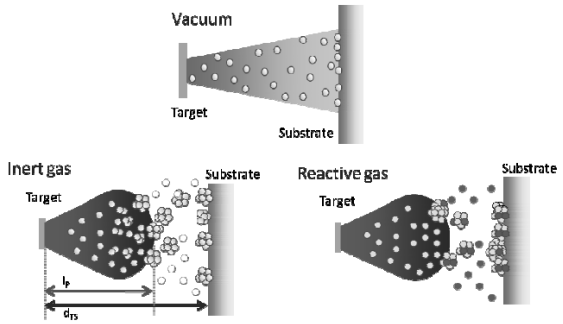

Figure 2.2: Schematic representation of the plasma plume expansion mechanism occurring during pulsed laser deposition in three distinct situations – i.e. in vacuum conditions, in an inert atmosphere and in the presence of a reactive background gas [46].

The plasma plume expansion dynamics has a key role in determining the characteristics of the ablated species impinging on the substrate and, consequently, in affecting the growth of two-dimensional materials and structures on top pf the substrate itself. Hence, the control of the deposition parameters affecting the plasma

plume expansion dynamics is of great importance in order to deposit materials with the desired morphology, structure and properties [46]. More in detail, it is possible to discriminate between the parameters of the laser and those of the deposition process. The former are, for instance, the wavelength of the laser light, the fluence, the frequency of the laser pulses (i.e. the repetition rate), the pulse duration and so on, while the latter include the target-substrate distance, the pressure and type of the background gas and the deposition time. The proper tuning of all these experimental parameters allows us to control the morphology and the structure of the deposited material in a very fine way and hence to fabricate materials and nanostructures with desired chemical, physical, electronic and optical properties and suitable for specific applications.
In conclusion, it can be useful to list the pros and cons of pulsed laser deposition in order to be aware of the advantages and limitations of the growth technique chosen to fabricate two-dimensional materials and nanostructures during the experimental work presented in this thesis. On one hand, PLD has some drawbacks such as the production of macroscopic particles that are generated during the ablation process and can be deposited on top of the substrate affecting the structure and morphology of the grown material. In addition, other relevant disadvantages to be overcome include the presence of impurities in the target material that can be found also in the grown structures and the crystallographic defects that can be found in the deposit due to the bombardment by high kinetic energy ablation particles. On the other hand, however, PLD for ultrathin films and 2D materials growth has several advantages [22, 47]:

1. rather low deposition temperatures can be exploited and it is even possible to carry out the growth process by keeping the substrate at room temperature and performing a post-annealing treatment in order to favour the ordering and crystallization of the deposited material;
2. almost any solid material can be ablated and hence deposited on top of the desired substrate;
3. since the deposition process is characterized by a pulsed nature and each laser pulse results in the vaporization of a very small amount of material, it is possible to control the growth rate very finely;
4. under optimized processing conditions, the ratios of the elemental components of the target and the deposited material are the same (even in the case of systems characterized by a complex chemical composition) and hence stoichiometric transfer of the ablated material from the target to the substrate can be achieved;
5. as the working conditions are far from the chemical equilibrium, PLD offers the possibility to produce novel or metastable materials that are not attainable under traditional thermal conditions;
6. uniform deposition of the vaporized material (in terms of chemical composition, morphology, structure and thickness) can be achieved on large areas, even in the centimetre length scale;
7. high growth rates combined with low costs make PLD a deposition technique compatible with the requirements of mass production and hence suitable for future industrial applications.

All these desirable features have contributed to make PLD increasingly employed as a deposition method and complementary to the traditionally used growth techniques (such as thermal evaporation, chemical vapour deposition and molecular beam epitaxy), in turn characterized by both advantages and limitations. Therefore, all the listed advantages can justify the use of pulsed laser deposition for the fabrication of high-quality 2D materials and nanostructures and the exploitation of this very versatile growth technique in the field of laboratory research.

2.2 Scanning tunneling microscopy (STM) and scanning tunneling spectroscopy (STS)

The scanning tunneling microscope was invented in 1981 by G. Binnig and H. Rohrer, who were awarded by the Nobel Prize in physics in 1986. This invention has opened the way to subsequent progresses in surface science as it has made possible the birth and development of a very powerful characterization tool. Indeed, scanning tunneling microscopy allows the investigation and study of surfaces in the real space and with unprecedented spatial resolution, down to the nanometer and even atomic length scale. Since its invention,

STM has provided relevant information on the physical properties (structure and morphology) of several surfaces and relevant advances have been made both in the theoretical understanding and in the experimental application of STM as a characterization technique. In addition, the scanning tunneling microscope has demonstrated to be capable of performing also spectroscopic measurements. Indeed, scanning tunneling spectroscopy has proven to be a peculiar technique that can be exploited for the local investigation of the surface electronic properties, managing to probe simultaneously the density of states (DOS) of both occupied and empty energy levels. Despite being very powerful characterization techniques, STM and STS provide experimental results that are very difficult to be analysed. Therefore, the development and exploitation of several theoretical tools is necessary in order to support the achieved experimental findings. In the following, the working principle and the theoretical models used to describe the physical mechanisms at the basis of scanning tunneling microscopy and spectroscopy will be briefly discussed.

2.2.1 Working principle and theoretical concepts

The physical phenomenon at the basis of scanning tunneling microscopy is the tunneling effect, which can be observed when a sharp metallic tip and the sample surface are put very close (within a fraction of a nanometer) one to the other, a bias voltage is applied and, as a consequence, a current flows between the tip and the sample. More in detail, a voltage ranging from ~10 mV to few volts is applied between the tip and the sample resulting in a tunneling current in the order of 1 nA that arises when a tip-sample distance of 0.5 - 1 nm is achieved and that flows across the tunneling potential barrier. It can be now useful to describe the working principle of a scanning tunneling microscope and, for this purpose, a schematic representation of an STM is shown in figure 2.3.

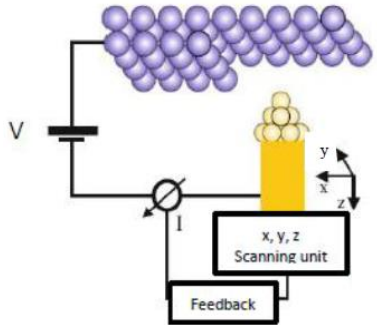

Figure 2.3: Schematic representation of a scanning tunneling microscope. Adapted from [48].

In the scanning tunneling microscope present in our laboratory, the metallic tip is mounted on a cylindrical scanner tube that is driven by three piezoelectric actuators, capable of moving and positioning the tip with very high accuracy: the x-piezo and the y-piezo control the in-plane movement while the z-piezo governs the vertical displacement of the tip and hence the tip-sample distance. The sample is upside-down and electrically connected to the ground (while the bias voltage necessary to generate the tunneling current is applied to the tip). During the experimental activity reported in this thesis work, homemade tungsten (W) tips fabricated through electrochemical etching have been used and the samples have been mounted on top of a tantalum (Ta) plate before performing PLD and STM/STS characterization. Before starting the STM measurements, a software is used in order to set the measurement parameters – i.e. the tip-sample bias voltage, the current set-point, the scan speed and the frame size – considering that the voltage can range from -10 V to +10 V. Subsequently, a voltage is applied between the tip and the sample, the tip is approached towards the sample surface until a tunneling current flows across the potential barrier and the tip starts to scan the sample surface. While the tip is scanned along the surface in the x and y directions, a feedback mechanism continuously adjusts the tip height by approaching or retracting the tip in order to maintain a constant value of the tunneling current [48]. More precisely, the tunneling current flowing between the tip and the sample is amplified by a transimpendance pre-amplifier, which usually works with a gain of 3×10^7

and a bandwidth of 80 kHz, the resulting signal is compared with the established current set-point and finally the feedback loop generates the error signal that drives the z-piezo, and hence the tip, in order to have a constant tunneling current. By recording the feedback signal as a function of the in-plane position, it is possible to obtain a map (or image) of the tip height that roughly corresponds to the topography of the sample surface. Nevertheless, it is fundamental to underline that the interpretation of the tip height for constant tunneling current as the surface topographic profile is only a first approximation [48]. Indeed, the STM images can be affected by surface electronic effects such as, for instance, the presence of atoms with different electronic properties – i.e. a different tunneling conductivity - that result in a different apparent height on the sample surface and hence a different colour contrast in the STM image.
The system consisting of the metallic tip and the sample separated by a certain gap is very complex and can be treated in different approximations. However, it can be useful to consider at first a simple one-dimensional model [48] for tunneling in order to grasp the very important exponential dependence of the tunneling current on the tip-sample distance. In classical mechanics, an electron moving in a region of space where a potential step U(z) is present (being z the direction of motion) is characterized by an energy E given by the sum between the kinetic energy of the particle and the potential U(z):

$$E = \frac{p_z^2}{2m} + U(z) \tag{2.1}$$

In the region where E > U(z), the electron has a non-zero kinetic energy while, on the contrary, the electron can not penetrate into a region of the space where E < U(z). Such a region is called a classically forbidden potential barrier. In quantum mechanics, however, the same electron is described by a wavefunction ψ(z) which satisfies the Schrödinger equation:

$$-\frac{\hbar^2}{2m}\frac{d^2}{dz^2}\psi(z) + U(z)\psi(z) = E\psi(z) \tag{2.2}$$

Different solutions of the Schrödinger equation are found in the classically allowed and in the classically forbidden regions (see figure 2.4(a) for a graphic representation). In the former case – i.e. when E > U(z) - the wavefunctions satisfying the Schrödinger equation are:

$$\psi(z) = \psi(0)e^{\pm ikz} \tag{2.3}$$

where

$$k = \frac{\sqrt{2m(E - U(z))}}{\hbar} \tag{2.4}$$

is the wavevector. This means that the electron is moving (in either a positive or negative direction) with a constant velocity, which is the same as in the classical case, and the real part of the electron wavefunction is characterized by an oscillating behaviour. Conversely, in the latter case – i.e. when E < U(z) – the Schrödinger equation has solutions given by:

$$\psi(z) = \psi(0)e^{\pm \kappa z} \tag{2.5}$$

where

$$\kappa = \frac{\sqrt{2m(U(z) - E)}}{\hbar} \tag{2.6}$$

is the decay constant describing the state of an electron that decays along the z direction. This means that the solutions of the Schrödinger equation in the classically forbidden region are exponentially decaying wavefunctions and the probability of finding a particle at a position z inside the barrier is proportional to the square modulus of the wavefunction itself:

$$|\psi(z)|^2 = |\psi(0)|^2 e^{-2\kappa z} \tag{2.7}$$

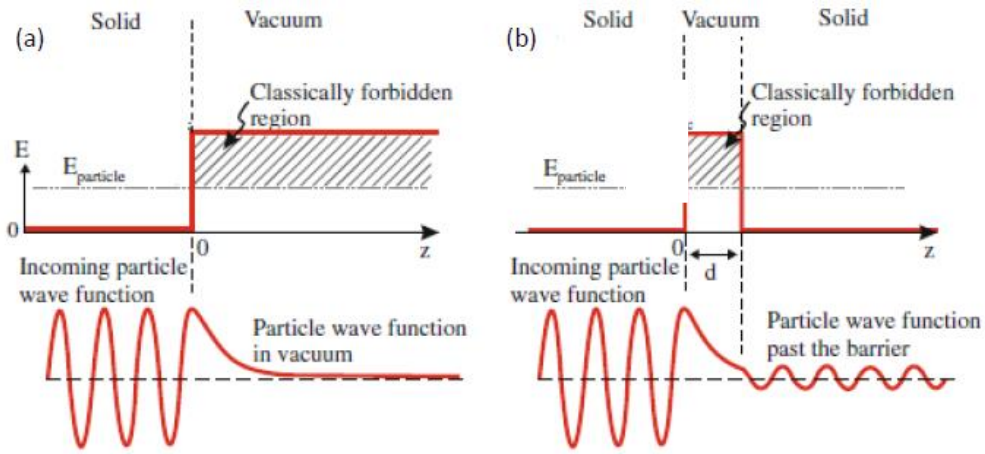

Figure 2.4: (a) Top: potential diagram of a finite potential step. Bottom: real part of the electron wavefunction featuring an exponential decay in the vacuum region – i.e. inside the potential barrier. (b) Top: potential diagram of a finite rectangular barrier. Bottom: real part of the electron wavefunction that is oscillating in front of the barrier, exponentially decaying inside the barrier and oscillating again past the barrier. Reproduced from [48].

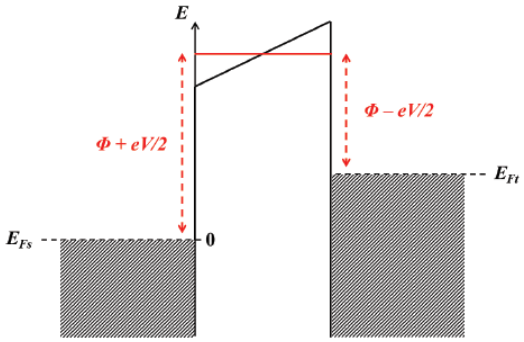

Figure 2.5: Energy diagram representing the potential barrier present between the tip (on the right) and the sample (on the left). The linear trend of the potential in the barrier region can be approximated by considering a constant value of the potential equal to ϕ + eV/2, considering that ϕ is the average value between the tip and sample workfunctions.

However, this happens in the case of a finite potential step while the tip-sample system can be better described by a trapezoidal barrier, in which the asymmetry is due to the bias voltage applied between the tip and the sample and is necessary in order to have tunneling (figure 2.5). However, the linear trend of the potential in the barrier region can be approximated by considering a constant value of the potential equal to ϕ + eV/2 (where ϕ is the average between the workfunctions of the tip and the sample) and hence a finite rectangular barrier, in which the size of the potential barrier roughly corresponds to the tip-sample distance d (see figure 2.4(b)). As the probability of finding an electron in the barrier region exponentially decreases along the z direction, if the potential barrier is sufficiently thin – i.e. if the tip-sample distance is enough small – it is possible to have a non-zero probability of finding the particle at a position z = d. Thus, it is possible for the particle to cross the potential barrier and to tunnel from the tip to the sample, or vice versa. In such

conditions, a transmission coefficient can be defined as the ratio between the probability of finding the particle at the position z = d and the probability of finding the electron at z = 0:

$$T = \frac{|\psi(d)|^2}{|\psi(0)|^2} \approx e^{-2\kappa d} \tag{2.8}$$

As can be observed, the transmission (or tunneling) coefficient decays exponentially with the tip-sample distance d. Nevertheless, the relevant parameter that has to be considered in scanning tunneling microscopy is not the transmission coefficient but the tunneling current I. However, it can be found that the tunneling current I is proportional to the transmission coefficient T and thus it is in turn characterized by the same negative exponential dependence on the tip-sample distance [48]. Moreover, it is worth noting that a small variation in the barrier thickness (for instance, 0.1 nm) results in a change in the transmission factor of an order of magnitude. Hence, the tunneling current increases by an order of magnitude if the tip approaches by 1 Å to the sample surface. This extremely high sensitivity of the tunneling current to the tip-sample distance is the reason for the incredibly high vertical resolution of the STM, which can reach the picometer regime and makes this characterization tool suitable for the investigation of surfaces and one- and two-dimensional nanostructures.
Nonetheless, the current flow across a tunneling junction is a complex many-particle problem, which takes into account the interaction between the tip and sample electronic states as well as the characteristics of the potential barrier, and thus can not be described by simply relying on the previously considered one-dimensional model. Indeed, different theoretical frameworks have been developed in order to address and explain this phenomenon. One of the most useful descriptions is based on the tunneling theory developed by Bardeen in 1961 [49] and then adapted to scanning tunneling microscopy for the first time in 1983 by Tersoff and Hamann [50].

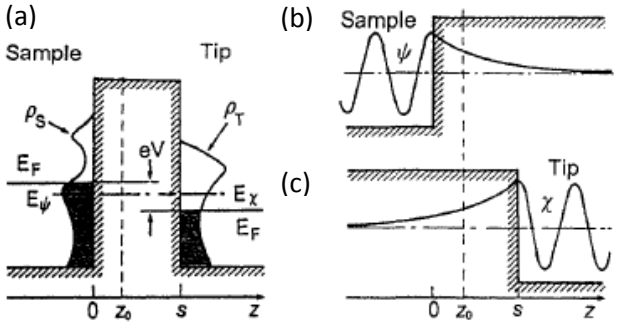

Figure 2.6: Schematic representation of the approach used by Bardeen in order to address the tunneling problem. Indeed, instead of solving the Schrödinger equation for the coupled system (a), Bardeen considers two separate subsystems ((b) and (c)) and exploits the time-dependent perturbation theory [51].

Bardeen's theory consists in a first-order time-dependent perturbation approach [49] and a schematic representation of this approach is shown in figure 2.6. Instead of trying to solve the Schrödinger equation of the overall system (made up of the tip, the sample and the potential barrier), Bardeen considers two separate subsystems first and solves the stationary Schrödinger equation for the tip and the sample independently in order to find the electronic states of the two separate subsystems. Then, the rate of transferring an electron from the tip to the sample (or vice versa) is calculated exploiting the time-dependent perturbation theory. As a result, Bardeen shows that the amplitude for electron transfer – i.e. the tunneling matrix element M – can be evaluated starting from the surface wavefunctions of the two subsystems taken at a separation surface (considering that the choice of the separation surface does not significantly affect the result). In other words, Bardeen finds that the tunneling matrix element M is determined by a surface integral on a separation surface lying in between the tip and the sample – i.e. at a position $z = z_0$:

$$M = \frac{\hbar}{2m}\int_{z=z_0}\left(\chi^*\frac{\partial\psi}{\partial z} - \psi\frac{\partial\chi^*}{\partial z}\right)dS \tag{2.9}$$

where χ and ψ are the wavefunctions of the tip and the sample, respectively.
The rate of electron transfer is then determined by means of the Fermi golden rule according to which the probability P for an electron in the state ψ of the sample (with energy E_ψ) to tunnel into the state χ of the tip (with energy E_χ) is given by:

$$P = \frac{2\pi}{\hbar}|M|^2\delta(E_\psi - E_\chi) \tag{2.10}$$

where the δ function present in the equation implies that only the electronic states characterized by the same energy in the two subsystems can tunnel one into the other. Subsequently, Bardeen evaluates the tunneling current by summing over all the relevant electronic states and considering that the electrons in both the tip and the sample obey the Fermi distribution at any temperature T > 0 K. When a bias voltage V is applied between the tip and the sample, the total tunneling current is given by:

$$I = \frac{4\pi e}{\hbar}\int_{-\infty}^{+\infty}[f(E_F - eV + \epsilon) - f(E_F + \epsilon)] \times \rho_S(E_F - eV + \epsilon)\rho_T(E_F + \epsilon)|M|^2 d\epsilon \tag{2.11}$$

where

$$f(E) = \frac{1}{1 + \exp\left(\frac{E - E_F}{k_B T}\right)} \tag{2.12}$$

is the Fermi distribution function and $\rho_S(E)$ and $\rho_T(E)$ are the density of states (DOS) of the sample and the tip, respectively.
If the thermal energy k_BT is sufficiently small, the Fermi distribution function can be approximated by a step function and the resulting expression for the tunneling current becomes:

$$I = \frac{4\pi e}{\hbar}\int_0^{eV}\rho_S(E_F - eV + \epsilon)\rho_T(E_F + \epsilon)|M|^2 d\epsilon \tag{2.13}$$

and, hence, Bardeen finds that the tunneling current is related to the convolution of the tip and sample DOS. Starting from the theoretical work done by Bardeen [49], Tersoff and Hamann [50] applied the Bardeen's approach to scanning tunneling microscopy in order to find the expression of the tunneling current in the limit of very small tunneling voltages – i.e. evaluating the transmission matrix element M at the Fermi level, which is almost the same for both the tip and the sample. In order to perform the calculation of the transmission matrix element, explicit wavefunctions for the tip and the sample have to be inserted into Eq. (2.9). However, although the sample wavefunctions can be described by a plane wave Fourier expansion, also the tip wavefunctions are needed to solve the integral and this can give rise to some problems because the structure of the tip is usually unknown. Therefore, Tersoff and Hamann assume the simplest possible approximation for the description of the tip, in the sense that they suppose that the tip wavefunctions are spherically symmetrical outside the tip region or, in other words, that only tip s-like orbitals are involved in the tunneling process. Within this approximation, the matrix element M is proportional to the sample

wavefunctions evaluated at the tip centre of curvature ($\mathbf{r_0}$) and, eventually, the tunneling current evaluated by Tersoff and Hamann is proportional to:

$$I \propto \rho_T(E_F) \sum_n |\psi_n(\boldsymbol{r_0})|^2 \delta(E_n - E_F) \tag{2.14}$$

where $\rho_T(E_F)$ is the tip density of states evaluated at the Fermi level, ψ_n represents the sample wavefunctions and the summation term represents the local density of states (LDOS) of the sample evaluated at the Fermi level and at the tip centre of curvature ($\mathbf{r_0}$). Thus, the expression of the tunneling current in Eq. (2.14) can be rewritten as:

$$I \propto \rho_T(E_F)\rho_S(E_F, \boldsymbol{r_0}) \tag{2.15}$$

Hence, according to this model, the tip essentially probes the sample wavefunctions at the position $\mathbf{r_0}$ and the scanning tunneling microscope measures the sample DOS at the tip position. With this approximation, STM has a quite simple interpretation as measuring a property of the surface, without having to consider the complex tip-sample system. This means that it is possible to assume (to a first approximation) that in STM the LDOS of the sample alone is measured without any influence due to the presence of the tip, but at the position at which the tip is located. However, it is better to underline that the model proposed by Tersoff and Hamann remains valid only when the tip wavefunction can be approximated by an s-wave – i.e. a spherical wavefunction – and, more importantly, in the limit of very small voltages.

The low-voltage approximation implemented in the STM theory by Tersoff and Hamann [50] is not suitable to describe voltage-dependent measurements, such as in the case of scanning tunneling spectroscopy, in which the applied voltage can be varied in a range of few volts around the Fermi level. Indeed, in those cases, a different approach has to be considered in order to derive the expression of the tunneling current as a function of the applied bias voltage. A very simple approach that can be taken into account is the energy-dependent approximation of the Bardeen model [48] in which, since each wavefunction corresponds to a particular energy value, the dependence of the transmission matrix element on the wavefunctions (Eq. (2.9)) can be replaced by a dependence on the energy. In reality, however, the tunneling current does not depend on the matrix element M but on its square modulus, which can be considered as a transmission factor (or tunneling coefficient) and is given by the following expression:

$$T(\epsilon, V, d) = \exp\left\{-\frac{2d}{\hbar}\sqrt{2m\left(\frac{\Phi_T + \Phi_S}{2} + \frac{eV}{2} - \epsilon\right)}\right\} \tag{2.16}$$

where d is the tip-sample distance, ϕ is the workfunction and the term in the round brackets is the effective or apparent barrier for an electron tunneling at energy ϵ with respect to the sample Fermi level (considered as the zero of the energy scale). This expression of the transmission factor comes from the exploitation of a one-dimensional Wentzel-Kramers-Brillouin (WKB) approximation, which can be used to address the problem of a potential barrier featuring any shape (U(z)). In the considered case, the barrier existing between the tip and the sample is assumed to be a trapezoidal one (as already mentioned) and, for simplicity, the integral can be calculated by considering a rectangular barrier and an average value of the potential (see figure 2.5 for a graphic representation). Then, since in the one-dimensional barrier approximation the square modulus of the transmission matrix element is replaced by the tunneling coefficient T(ϵ, V, d), the tunneling current (Eq. (2.13)) can be written as:

$$I(V) = \frac{4\pi e}{\hbar}\int_0^{eV} \rho_T(\epsilon - eV)\rho_S(\epsilon)T(\epsilon, V, d)d\epsilon \tag{2.17}$$

This is the Bardeen's equation for a one-dimensional barrier in the limit of zero temperature – i.e. by considering the Fermi functions as step functions. This formula is suitable in order to consider the voltage-dependence of the tunneling current and hence it can be used in order to carry out the interpretation and the analysis of the STS data, as will be explained in the following section.
In conclusion, it is evident that the tunneling current and, consequently, the STM images depend not only on the surface topography but also on the sample electronic properties and these two different contributions have to be considered very carefully during the analysis of the STM data. In relation to this aspect, it is worth noting that STM measurements are affected by the value and sign of the bias voltage [48], exactly because not only the surface topography but also its electronic properties are relevant. Indeed, the tip is able to probe the occupied valence band states or the empty conduction band states of the sample depending on the fact that a negative or positive bias is applied between the tip and the sample. In order to better explain this peculiar aspect of the STM measurements, it is possible to consider the two situations depicted in figure 2.7, in which the tip is grounded and the bias is applied to the sample. For positive bias voltages V (figure 2.7(a)), the Fermi level of the sample decreases by a quantity equal to eV and the electrons tunnel from the filled valence band of the tip to the empty conduction band states of the sample in such a way that STM probes the empty energy levels of the sample. On the contrary, when a negative bias voltage is applied between the tip and the sample (figure 2.7(b)), the sample Fermi level increases by eV, the electrons tunnel from the sample valence band to the tip conduction band and hence the STM image is given by the contributions coming from the occupied sample energy levels.

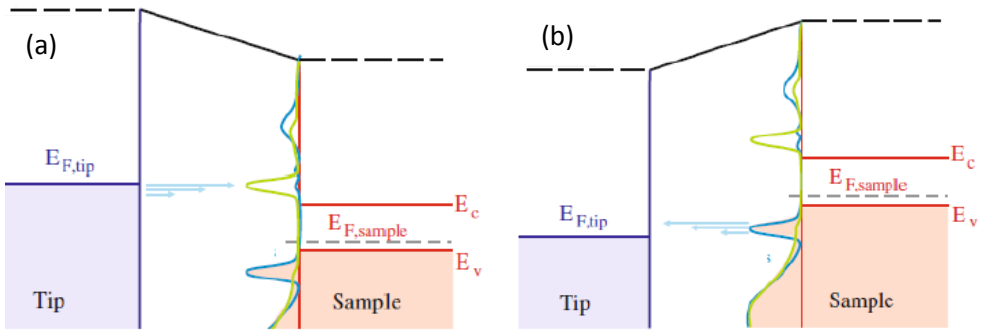

Figure 2.7: Schematic representation of the energy levels involved in tunneling as a function of the applied voltage sign. (a) For positive voltages applied between the tip and the sample, electrons tunnel from the tip valence band (VB) to the sample conduction band (CB), while (b) electrons tunnel from the sample VB to the tip CB for an applied reverse bias. Reproduced from [48].

2.2.2 Scanning tunneling spectroscopy (STS)

The main goal of STS is to obtain information about the surface electronic properties and, in particular, about the local density of states of the sample under investigation. Indeed, one of the attractive features of STS is its ability to obtain energy-resolved spectroscopic data with atomic resolution and to measure directly the spatial and energy dependence of the sample LDOS [48]. The traditional experimental approach exploited in order to obtain the sample LDOS as a function of the electron energy relies on the measurement of the differential conductivity – i.e. the derivative of the tunneling current with respect to the applied bias voltage (dI/dV). Starting from the tunneling current written as in Eq. (2.17), a very simple expression for the differential conductivity (dI/dV) can be derived:

$$\frac{dI}{dV} \approx \frac{4\pi e^2}{\hbar}\rho_T(0)\rho_S(eV)T(eV, V, d) \tag{2.18}$$

In the simplest possible approximation, the tip DOS and the transmission factor are supposed to be voltage independent and, hence, the differential conductivity can be considered to be proportional to the sample DOS, which depends on the energy [48]. In particular, the differential conductivity is approximately proportional to the sample DOS at the energy eV relative to the Fermi energy of the sample itself:

$$\frac{dI}{dV} \propto \rho_S(eV) \tag{2.19}$$

Before discussing the analytical methods for extracting the sample DOS from the acquired STS data, a brief explanation about how STS measurements are usually carried out can be useful. During STS, the tip position is fixed over one specific point of the sample surface and the feedback loop is deactivated in such a way that the tip-sample distance is maintained constant as the bias voltage is varied linearly within a certain range. During the voltage ramp, the dI/dV signal is recorded by means of a lock-in amplifier (whose schematic representation is shown in figure 2.8).

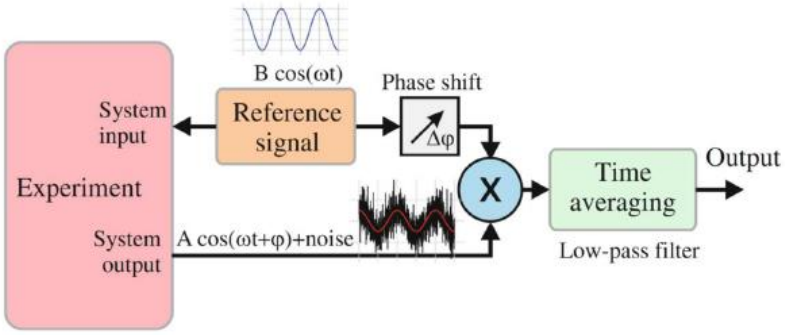

Figure 2.8: Schematic representation of the lock-in amplifier working principle. The reference signal produced by the lock-in amplifier acts as the modulation voltage in the STM system and is superimposed to the bias voltage applied between the tip and the sample. The output is the tunneling current signal, which is multiplied by the phase-shifted reference. Finally, the output filter selects only the component of interest, which is roughly proportional to dI/dV. All the other components (whose frequencies are different from the modulation frequency) are suppressed. Reproduced from [48].

The lock-in amplifier contains a reference oscillator generating a sinusoidal voltage signal that is superimposed to the bias voltage applied between the tip and the sample. The amplitude and the frequency of the oscillating signal can be properly tuned and, typically, a 43 mV_{rms} signal oscillating at a frequency of 6 kHz is used. This modulation voltage produces a tunneling current oscillating at the same frequency and that can be written as:

$$I(t) = I_0 + I_1 \sin(\omega t + \varphi) + \cdots \tag{2.20}$$

where ω is the operating frequency and higher order terms are neglected because they are not relevant for the considered lock-in measurements. Indeed, if the modulation voltage is small enough, the current-voltage relationship can be approximated as follows:

$$I(V) = I\big(V_0 + \Delta V(t)\big) \approx I(V_0) + \left(\frac{dI}{dV}\right)_{V=V_0} V_m \sin \omega t \tag{2.21}$$

where V_0 is the applied bias voltage and V_m is the modulation amplitude. Therefore, the term I_1 in Eq. (2.20) is roughly proportional to the differential conductivity dI/dV. The lock-in amplifier receives the current as input and then multiplies it by the reference signal (whose phase ψ has been properly shifted) obtaining:

$$I(t) \times \sin(\omega t + \psi) = I_0 \sin(\omega t + \psi) + I_1 \cos(\varphi - \psi) + \cdots \quad (2.22)$$

Then, a low-pass filter (with a proper time constant, for instance 1 ms) filters out all the oscillating terms, giving as output the quantity of interest containing I_1 and thus the differential conductivity.
After having briefly described the experimental procedure that allows us to obtain the differential conductivity, the problem of the extrapolation of the sample DOS from the measured dI/dV spectrum has to be addressed. First of all, it should be underlined that the expression of the differential conductivity is in general more complex than the one reported in Eq. (2.18) and can be written as:

$$\frac{dI}{dV} \approx \frac{4\pi e^2}{\hbar}\rho_T(0)\rho_S(eV)T(eV,V,d) + \frac{4\pi e}{\hbar}\int_0^{eV}\rho_S(\epsilon)\frac{d}{dV}[T(\epsilon,V,d)\rho_T(\epsilon - eV)]d\epsilon \quad (2.23)$$

where the first term contains the quantity of interest $\rho_S(eV)$ – i.e. the sample DOS as a function of the energy. However, it is worth noting that the relationship between dI/dV and $\rho_S(eV)$ is not trivial and, in addition, the influence of the tunneling coefficient and the tip DOS is generally non-negligible. In particular, the exponential dependence of the tunneling factor on the voltage usually causes the presence of a significant background that can hide the DOS features in the acquired dI/dV curve. Therefore, the extraction of the information about the sample DOS from the dI/dV curves is a relevant problem when performing STS measurements and some analytical methods have been proposed in order to address it.
The first analytical approach has been proposed by Stroscio *et al.* [52] and essentially consists in normalizing the differential conductivity dI/dV by the total conductivity I/V in order to remove the exponential increase of the tunneling coefficient with the voltage. This is possible because dI/dV and I/V feature the same exponential increasing tails at both ends of the voltage interval. The obtained dimensionless quantity (dI/dV)/(I/V) provides a convenient plot of the STS data and, in addition, it is worth noting that the normalized differential conductivity is often identified with the sample DOS. Indeed, by assuming a constant tip DOS, it can be written as:

$$\frac{dI/dV}{I/V} \approx \frac{\rho_S(eV)T(\epsilon = eV,V)}{\frac{1}{eV}\int_0^{eV}\rho_S(\epsilon)T(\epsilon,V)d\epsilon} = \frac{\rho_S(eV)}{\frac{1}{eV}\int_0^{eV}\rho_S(\epsilon)\frac{T(\epsilon,V)}{T(\epsilon = eV,V)}d\epsilon} \quad (2.24)$$

Indeed, as the ratio between the transmission factors occurs at the denominator and their dependence on the voltage and tip-sample distance is similar, the denominator can be considered as slowly varying with the voltage and thus the normalized differential conductivity can be considered as roughly proportional to the sample DOS evaluated at eV. Hence, despite lacking of a solid theoretical foundation, this type of normalization is very useful and offers several advantages (such as the suppression of effects related to a variation in the tip-sample distance during STS measurements). However, several limitations have to be considered. In particular, an obvious problem with this normalization procedure arises for semiconductors characterized by the presence of a surface band gap, where both the tunneling current and the differential conductivity can go to zero if no surface states are present in the band gap.
These numerical problems arising during the STS investigation of semiconducting surfaces may be overcome with a more refined analytical method proposed by Ukraintsev [53] and allowing to extract the sample DOS from the acquired STS data. More in detail, it consists in normalizing the differential conductivity by a proper tunneling probability function that can be written as:

$$f(V,d) \propto T(eV,V,d) + T(0,V,d) \quad (2.25)$$

where T is the transmission coefficient given by Eq. (2.16) and d is the tip-sample distance. The function f is able to approximate the behaviour of the transmission coefficient for both positive and negative voltages. Hence, normalizing the differential conductivity by the function f results in the removal of the exponentially increasing background present in the STS curves, especially when STS measurements are carried out in a quite extended voltage range – i.e. few volts.
The problem of recovering the sample DOS from the recorded STS data has been also addressed by Koslowski *et al.* [54]. Very briefly, they replace the integral term in Eq. (2.23) with its value at the middle of the bias window – i.e. at ϵ = eV/2 – and eventually they obtain the following expression for the sample DOS:

$$\rho_S(eV) = \frac{\hbar}{4\pi e^2 \rho_T T(eV,V)}\left(\frac{dI}{dV} + \frac{ed\sqrt{2m}}{2\hbar\sqrt{\Phi}} I(V)\right) \tag{2.26}$$

This relation is very useful in order to obtain the sample DOS from the dI/dV and I(V) signals recorded during STS measurements, in particular considering that I(V) can be measured simultaneously to the differential conductivity. The only limitation is related to the fact that the tip-sample distance has to be determined independently and this is a relevant problem for the methods of both Koslowski and Ukraintsev.
In reality, no normalization method has been applied to the STS spectra reported in this work. Indeed, in the framework of this experimental activity, the acquired I(V) and dI/dV curves have been simply exploited in order to investigate the surface electronic properties of the samples in terms of size of the energy gap and position of the VB and CB onsets. On the contrary, the recorded STS spectra have not been used to extrapolate the sample DOS and, hence, a normalization procedure has not been necessary.
In conclusion, it is worth mentioning another peculiar application of the lock-in technique. Indeed, the lock-in amplifier can be exploited not only in order to locally measure the dI/dV signal but also in order to obtain the so-called dI/dV maps or LDOS maps, in which the colour contrast reflects the spatial variations of the electronic properties of the surface under investigation. More in detail, these maps consist in images of the differential conductivity acquired at constant bias voltage during the STM characterization process and they represent to a first approximation maps of the sample density of states at a given energy. Thus, by acquiring some dI/dV maps at different applied bias voltage – i.e. at different electronic energies – additional electronic features of the surface can be recognized and investigated, even if they can not be properly resolved by constant-current STM images. This experimental procedure is very intriguing and has been used, for instance, in order to count the number of layers forming two-dimensional ZnO nanostructures [43, 45].

2.3 Other characterization techniques

No characterization technique is capable of supplying all the possible types of information regarding the two-dimensional system under investigation. Thus, besides using STM and STS in order to characterize the morphological, structural and electronic properties of the deposited materials and nanostructures, other characterization techniques able to provide different and complementary information are usually exploited. In particular, Auger electron spectroscopy is employed to investigate the chemical composition of the samples, obtaining for instance, information about the stoichiometry of the deposited material. In addition, Raman and photoluminescence spectroscopies are used as additional characterization tools since they are very powerful investigation techniques capable of giving information about the vibrational modes of the material, the number of layers forming the two-dimensional structures under investigation, the influence of the interaction with the substrate and so on. In the following, a brief discussion of these three characterization methods is presented and, more precisely, attention will be focused on the explanation of the involved physical phenomena, the description of the experimental apparatus and the indication of the type of information that can be obtained.

The first additional characterization technique to be considered is **Auger electron spectroscopy (AES)** [55] that is based on the excitation of the so-called Auger electrons and that can be employed in order to identify the elements present on the surface and in the first few atomic layers of the sample and, hence, to evaluate the chemical composition of the system under investigation. AES is usually carried out using primary electrons with typical energies between 3 and 30 keV and exploiting the possibility to focus the primary electron beam in the nanometer and micrometer range in order to analyse the topmost atomic layers of the sample under investigation. A schematic representation of the Auger process is shown in figure 2.9(a).
During AES measurements, primary electrons arrive at the sample surface and their energy has to be sufficiently high to extract an electron (usually defined as a secondary electron) from a core level W – i.e. K, L, M and so on – characterized by an energy E_W. Then, the empty electron position is filled by another electron coming from a level E_X closer to the Fermi level. The transition of this electron from level X to level W releases an energy equal to $E = E_X - E_W$ which is in turn transferred to a third electron of the same atom at level E_Y. If the acquired energy is enough large, this third electron is extracted from the material and its kinetic energy is related to the energy difference between the three electronic levels involved in the Auger process and to the sample workfunction ϕ – i.e. the energy necessary in order to extract an electron from a material. More in detail, the kinetic energy of an Auger electron related to a specific element with a certain atomic number Z and to a specific Auger transition (for instance, KLL, LMM or MNN) can be written as:

$$E_{WXY} = E_W(Z) - E_X(Z) - E_Y(Z) - \Phi \qquad (2.27)$$

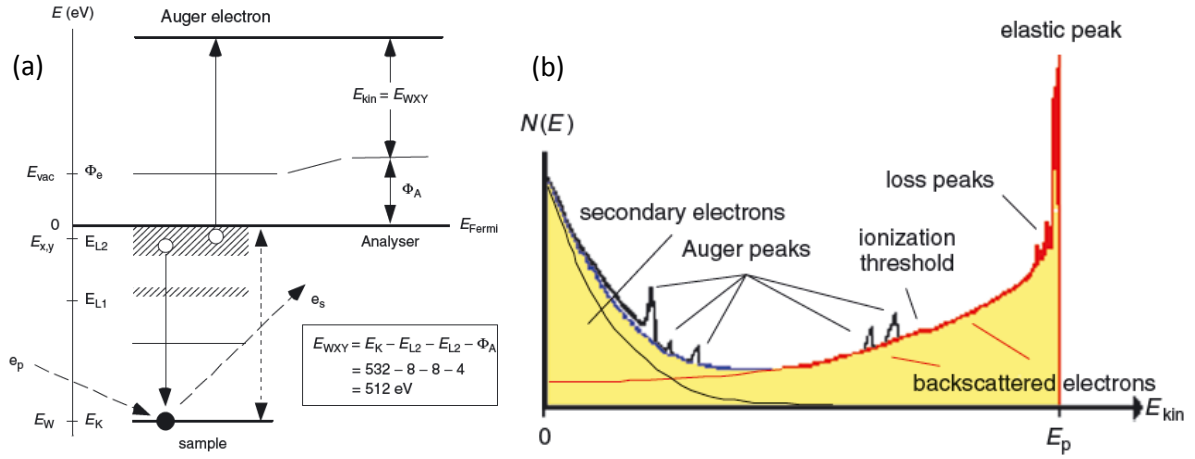

Figure 2.9: (a) Schematic representation of the Auger process in which Φ_e and Φ_A are the workfunctions of the sample and the analyser, respectively. (b) Schematic representation of an Auger spectrum. The Auger peaks are superimposed to the spectrum of the secondary electrons and the elastic peak at E_p represents the primary electrons. Reproduced from [55].

The output of this kind of spectroscopic measurements is a spectrum in which the number of detected electrons N(E) is given as a function of the kinetic energy E_{kin} (as shown in figure 2.9(b)). Usually, however, in order to make the peaks more evident, a spectrum in which dN(E)/dE is plotted as a function of the kinetic energy can be obtained by representing the peaks in their differentiated form after background subtraction. In reality, it is worth mentioning that another phenomenon can occur when focusing the primary electron beam on the sample surface: the emission of characteristic X-rays [55]. Indeed, when an electron decays from the level X to the level W, the released energy can either be transferred to another electron of the same atom (Auger process) or be emitted in the form of a photon with energy $E = h\nu = E_X - E_W$. Whether an Auger electron or a photon is emitted is determined by specific quantum mechanical selection rules. Hence, there is only a certain finite probability of having an Auger transition, which is in the order of 1 in 10^4 and which is determined by the probability of ionization of the core level W and of the de-excitation process involving the emission of an Auger electron. More specifically, the emission probability varies with the atomic number Z

of the considered element and the type of atomic levels involved (K, L, M and so on). Usually, the probability of excitation via an Auger process is very high for light elements and for transitions of the KLL type. However, even for heavy elements, it is possible to observe a relatively high probability in the case of LMM or MNN transitions [55].
As regards the experimental setup, the main components of an Auger spectrometer are the electron gun (necessary in order to produce the primary electron beam) and the energy analyser (needed for the detection of the emitted Auger electrons) [55]. Typically, they are both placed in an ultra-high vacuum chamber characterized by a base pressure of 10^{-9} - 10^{-8} mbar. Such a low pressure is essential to guarantee a contamination-free surface and to keep the rate of residual gases adsorption below 10^{-3} ML/s. The most commonly used electron source is a thermionic source in the form of a tungsten filament. In particular, the material is heated by making a certain current flow inside the material itself and in order to obtain a sufficiently high temperature to give the electrons enough energy to reach the vacuum. As for the analyser, it is necessary to count the emitted Auger electrons as a function of their kinetic energy and to generate the Auger spectrum. In order to optimize the signal intensity and to calibrate the analyser, primary electrons of known energy that are reflected from the sample surface are employed.
Finally, it is important to be aware of the kind of information that can be obtained from an AES measurement. First, the emitted Auger electrons have a characteristic energy, allowing the identification of the emitting elements and hence of the atoms present on the surface or in the first few layers of the investigated sample. In particular, Auger electrons provide information on the elemental composition of the first 2 – 10 atomic layers of the sample [55]. This because, while characteristic X-rays have a very high probability of escaping from the whole sample thickness, Auger electrons with energies up to 2000 eV have a high probability to escape only from the first few layers of the material, being therefore more suitable for a surface analysis of the sample. Second, since each element is characterized by specific Auger transitions, the presence of surface contaminants (such as carbon) can be detected, even if AES cannot be used to reveal the presence of H or He because, since for an Auger transition a minimum of three electrons is required, only elements with $Z \geq 3$ can be detected. Third, a change in the oxidation state of an element can be easily observed because it results in a shift of the binding energy of the valence band level and, in principle, each time a change in the binding energy occurs, a chemical shift of the Auger transitions is also noticed [55].
During the experimental activity presented in this thesis work, AES measurements have been performed *in situ* (under UHV conditions and a base pressure of approximately 10^{-9} mbar) before and after the exposure of the sample to ambient pressure. In particular, before extracting the sample from the UHV chamber, Auger electron spectroscopy has been carried out in order to verify the chemical composition of the deposited 2D material, while, after having reintroduced the sample into the system, AES has been exploited in order to evaluate the eventual damage and contamination of the material caused by air exposure.

Besides AES, **Raman spectroscopy** is a powerful characterization technique involving the interaction between the incoming photons and the material and the vibrational excitation of the atoms, finally resulting in the determination of the structure and chemical composition of the sample under investigation [55]. This characterization tool is based on the exploitation of the Raman effect, which is a scattering phenomenon observed for the first time by Sir C. V. Raman in 1928 and which can be explained both classically and quantum mechanically.
From the classical point of view, the Raman effect is related to the polarization of the electronic cloud describing chemical bonding due to the electric field of the incident electromagnetic radiation, which induces a dipole moment that is in turn time-dependent due to the vibration of the atoms forming the bond [55]. The combination between the frequency of the incoming radiation ν_i and the vibrational frequency ν_{vib} gives rise to inelastic scattering at frequencies $\nu_i + \nu_{vib}$ and $\nu_i - \nu_{vib}$, which are known as the anti-Stokes and the Stokes frequencies, respectively. This classical description is conceptually very simple but cannot explain the relative intensities of the Stokes and the anti-Stokes peaks in the Raman spectrum.

The quantum mechanical description of the Raman effect invokes a pseudo-absorption process in which the incident radiation is absorbed promoting the transition of the material into a virtual electronic state and the subsequent emission of a photon [55]. In particular, when crystalline structures are considered, the involved process is inelastic scattering, which involves the creation or annihilation of phonons – i.e. quanta of vibrational energy associated to the normal modes of oscillation of the crystal under investigation – and, during Raman spectroscopy, normal modes at the centre of the crystal Brillouin zone are typically measured. In reality, two different processes can occur. The first one consists in the pseudo-absorption of the incoming photons, the excitation of the material from a lower vibrational state (characterized by v = n) to a higher virtual level and the emission of other photons in order to come back to an excited vibrational state with v = n+1. As shown in figure 2.10(a), the energy difference between the incident and the emitted radiation is equal to one quantum of vibrational energy and the emitted photons (characterized by an energy lower than that of the incoming photons) are termed Stokes photons. On the contrary, the second process that can take place is described in figure 2.10(b), where the initial vibrational state is described by *v* = n+1 and, upon pseudo-absorption and re-emission, photons with energy higher than that of the exciting photons result. They are known as the anti-Stokes photons.

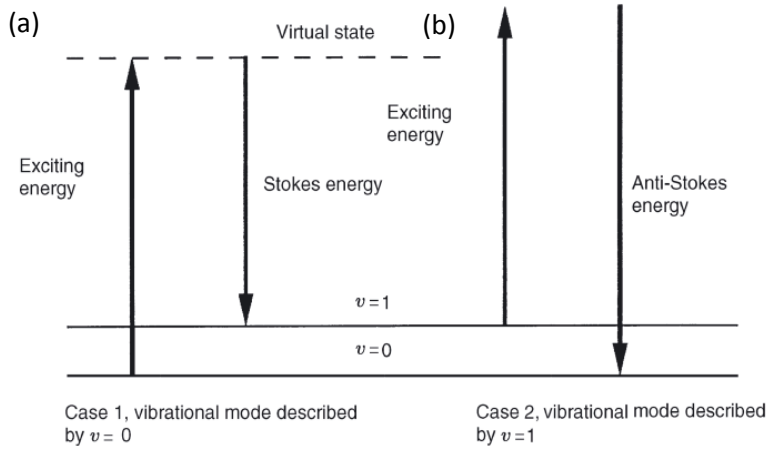

Figure 2.10: Schematic representation of the (a) Stokes and the (b) anti-Stokes processes [55].

Moreover, it is worth mentioning that, in some particular cases, the sensitivity that can be achieved with Raman spectroscopy is very high. These situations usually occur when the materials under examination are direct band gap semiconductors, capable of absorbing or emitting photons with reasonably high efficiency, and when the wavelength of the incident light is properly chosen to coincide with a particular electronic transition within either the substrate or the deposited film. Under these conditions, the virtual states displayed in Figure 2.10 become real levels and the process can be considered as resonant Raman scattering. In particular, it is important to underline that the enhancement of the Raman scattering efficiency that occurs when the resonance condition is satisfied can reach up to 10^6 times the efficiency achieved in off-resonance conditions [55].

After having briefly explained the physical phenomenon at the basis of Raman spectroscopy, it can be useful to describe the experimental apparatus needed to perform this kind of spectroscopic measurements. A schematic representation of the Raman experiment is shown in figure 2.11, in which the main components of a Raman spectrometer are shown: the laser, the monochromator and the detector. It is also worth mentioning that, in contrast with AES that has to be performed in UHV conditions due to the exploitation of a particle beam for investigating the sample, Raman spectroscopy employs the use of a light beam and, hence, is usually performed *ex situ*, under ambient conditions. This aspect is both an advantage and a limitation since it makes easier the experimental procedure but introduces the problem of the sample contamination.

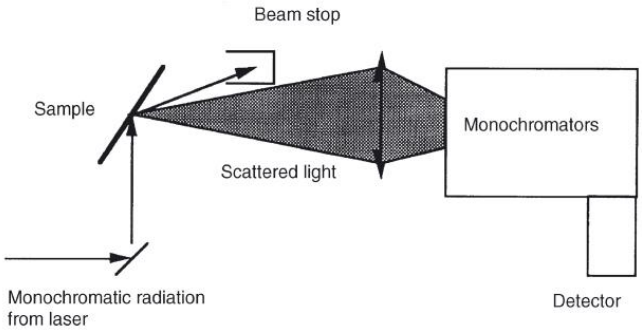

Figure 2.11: Schematic representation of Raman spectroscopic measurements [55].

Since the Raman effect is very weak (with only 1 in 10^{11} photons being inelastically scattered in a typical process [55]), the use of intense light sources – i.e. lasers - is normally required. Usually, the source providing the incident photons is an Ar laser, whose 457 nm (blue) and 514.5 nm (green) laser lines are mainly exploited, even if other light sources can be used, such as the He-Ne laser (wavelength: 632.8 nm) or the red line of the Kr laser (wavelength: 647.1 nm). When selecting the laser light to be employed in Raman spectroscopic measurements, it is necessary to be aware that the Raman scattering intensity decreases as the fourth power of the light source wavelength [55]. Therefore, it is an advantage to use the Ar laser lines (characterized by a shorter wavelength) unless other circumstances, such as sample fluorescence, sample photodecomposition or the location of the optical absorption edge in semiconductor materials, require a less energetic excitation source. The laser light is directed towards the sample surface, considering that the Raman technique may be applied to the investigation of a wide range of materials and that the use of a laser as the excitation source makes this technique suitable for the study of small areas of the sample surface. Once the light has reached the sample under investigation, it is scattered and the focusing optics is used in order to collect the scattered light and to direct it towards the monochromator and, eventually, the detector. On one hand, the most commonly used monochromator is a Czerny-Turner grating type featuring two collimating mirrors and a planar grating that is rotated to sweep the spectrum across the exit slit. Since Raman spectra are extremely weak, stray light within the monochromator must be effectively suppressed in order to provide a clean background for the Raman spectra. On the other hand, a CCD detector is usually used. Once the Raman measurements have been carried out, Raman spectrometers use computers for data collection and storage.
As regard the experimental findings that can be obtained by means of Raman spectroscopy, it is important to underline that the output of the measurements is a spectrum in which the intensity is plotted as a function of the so-called Raman shift, which is the distance in cm^{-1} of the Raman peaks from the elastic line that depends on the used laser light. Considering the positions of the peaks, several features about the investigated sample can be recognized and understood. First, since the frequencies at which the vibrational modes take place depend on the type of atoms involved and also on the kind of chemical bonding, the position of the peaks can be exploited in order to confirm the chemical composition of the material. Second, Raman spectroscopy is very useful in order to investigate the degree of order, the crystalline structure and the symmetry of the sample. For instance, in the case of two-dimensional materials deposited on top of a metallic substrate, the position and the shape of the Raman peaks can give information about the number of layers forming the 2D material, the order/disorder of the deposited film, the influence of the interaction between the overlayer and the underlying substrate (which may cause the quenching or the reduction in the Raman intensity of a particular vibrational mode) and so on.

The last characterization technique that has to be considered in the framework of this thesis work is represented by **photoluminescence (PL) spectroscopy**, a characterization technique that is typically employed in order to investigate the electronic and optical properties of the material (such as the size of its energy gap) and that can be also exploited to check the chemical composition of the system. PL is a

phenomenon including any emission of light that results from an optical stimulation [56]. The detection and analysis of the emitted light is widely used as a characterization tool due to its sensitivity, simplicity and low cost. Among these desirable features, sensitivity is one of the strengths of the PL technique, allowing very small quantities (nanograms) of material to be analysed.
In order to well understand the working principle of photoluminescence as a characterization method, it can be very useful to briefly describe the physical phenomenon at the basis of the PL process (schematically shown in figure 2.12).

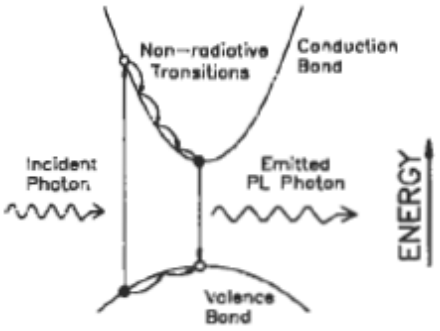

Figure 2.12: Schematic representation of the PL mechanism occurring in a semiconductor or in a crystalline system [56].

In PL a material gains energy by absorbing light at some wavelength and, as a consequence, an electron is promoted from a lower to a higher energy level. This may be described by considering a transition from the valence band to the conduction band of a semiconductor, which results in the creation of an electron-hole pair. Subsequently, the system undergoes a non-radiative internal relaxation process involving the interaction with crystalline vibrational and rotational modes and thus the excited electron moves to a more stable excited level, such as the bottom of the conduction band. Then, after a system-dependent characteristic lifetime in the excited state, which may last from picoseconds to many seconds, the system will come back to the ground state. In luminescent materials, some or all the energy involved in this final transition is released in the form of light (characterized by a wavelength longer than that of the incident light) and the relaxation is said to be radiative. Finally, this emitted light is detected as photoluminescence and the spectral dependence of its intensity is analysed to provide information about the properties of the material, such as, for instance, the presence of defect energy levels inside the band gap. The light involved in PL excitation and emission is usually in the wavelength range 200 - 2000 nm [56] and this is an important advantage since many electronic transitions of interest lie in this range and, in addition, efficient sources and detectors for these wavelengths are available. However, a wide variety of different mechanisms can participate in the PL process and influence the interpretation of the obtained spectrum. At room temperature, for instance, PL emission is thermally broadened while, as the temperature is lowered, features tend to become sharper and PL is often stronger due to the fact that fewer non-radiative processes can take place [56]. As regards PL measurements on semiconducting materials, PL is generally very useful in the case of direct band gap semiconductors, even if, especially at low temperature, localized bound states and phonon assistance allow certain PL transitions to appear even in materials with an indirect band gap, for which luminescence would normally not be expected.
PL measurements are generally non-destructive and only little sample preparation is necessary in order to clean the surface and to remove any contamination that may contribute its own luminescence during the characterization process, which can be carried out both in vacuum and in *ex situ* conditions. As regards the experimental setup, four basic components make up a PL system [56]:

1. a light source that is necessary for the excitation of the material under investigation, considering that continuous or pulsed lasers are required in order to carry out surface analysis;
2. a sample holder, including also optics for focusing the incident light and collecting the photoluminescence;

3. a dispersive element for the spectral analysis of the photoluminescence, which can be a simple filter or, more commonly, a scanning grating monochromator;
4. an optical detector (such as a photomultiplier tube) with appropriate electronics and readout.

A schematic representation of the PL apparatus is shown in figure 2.13 and, as can be seen, this system is very similar to that used in Raman spectroscopy.

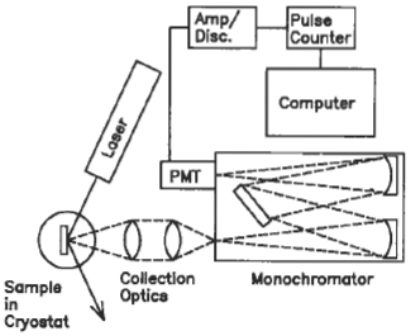

Figure 2.13: Schematic representation of a PL system incorporating a laser and photon-counting electronics [56].

Photoluminescence is a well-established and widely used tool for material and surface analysis as it is able to explore the correlation between the structure and composition of a material and its electronic states and to identify the presence and type of trace chemicals, impurities and defects [56]. The applications of PL as a characterization technique are quite various and include compositional analysis, trace impurity detection, structural determination (crystallinity, bonding and layering) and the study of energy-transfer mechanisms. Indeed, several types of information can be obtained from the analysis and interpretation of the acquired PL spectrum. For instance, the energy at which the PL peaks appear can be exploited in order to evaluate the chemical composition of the material, the size of the band gap, the presence of impurities (which give rise to spectral peaks that can sometimes be identified by considering their binding energy) or internal strain. Moreover, the peak width can give information about the structural and chemical quality of the material, while the peak intensity can be correlated to the presence of surface damage (due to sputtering, polishing and ion bombardment) and to the concentration of impurities and structural defects (arising, for instance, during the growth of the deposited film). In reality, however, a quantitative analysis based on the absolute or relative intensities of the PL peaks is difficult due to the fact that the PL intensities are strongly influenced by many factors like surface conditions, heating, photochemical reactions, oxygen incorporation and intensity, power density and wavelength of the exciting light [56]. If these factors are carefully controlled, the PL intensities can be used to study various aspects of the sample, but such control is not always possible and this is an important limitation that can affect the results of the characterization process.

In conclusion, it is worth mentioning that, during the experimental activity presented in this thesis work, Raman spectroscopy and PL measurements have been performed *ex situ* and using the same experimental apparatus. Indeed, a Renishaw InVia spectrometer, coupled with an Ar laser, has been used for the sample analysis exploiting a 1 mW excitation of 457 nm and 514.5 nm wavelength, respectively, through a 50x objective. More in detail, Raman spectroscopic measurements have been carried out employing the 457 nm excitation line, while the photoluminescence of the material has been investigated employing the excitation featuring the 514.5 nm wavelength.

Chapter 3

Experimental results

The experimental activity presented in this thesis work is essentially based on the study and investigation of semiconducting materials and nanostructures at the two-dimensional limit, which have been produced by means of PLD and characterized using STM and STS, together with other characterization tools (AES, Raman spectroscopy and PL measurements, in particular). All the experiments have been carried out in an ultra-high vacuum (UHV) system that is kept at a base pressure $<10^{-10}$ mbar, in such a way to avoid air exposure and contamination of the investigated samples.

Hence, STM, STS and AES measurements are carried out under UHV conditions and at room temperature and, in particular, the STM analysis is usually performed in constant-current mode during the experimental work reported in this thesis. On the contrary, STS measurements are carried out by fixing the position of the STM tip in correspondence of a specific point of interest of the surface under investigation in order to probe the sample LDOS in that specific point and to simultaneously record both the I(V) and the dI/dV spectra, from which information about the electronic properties of the system can be extrapolated. In the framework of this research activity, STS spectra have been acquired by applying a voltage ramp in such a way to investigate a range of few eV around the Fermi level of the material. In reality, however, It is worth mentioning that several I(V) and dI/dV curves have been acquired in correspondence of equivalent surface points, they have been averaged in order to obtain a single I(V) spectrum and a single dI/dV spectrum for each structure under investigation and the obtained dI/dV curve has been properly rescaled in order to adapt it to the numerical derivative of the corresponding I(V) curve.

In some cases, Raman and PL measurements have been carried out in order to further investigate the samples and to achieve additional information about the electronic, vibrational and optical properties of the deposited materials and of the overlayer/substrate system. Raman and PL analyses have been performed *ex situ*, under ambient conditions.

In this chapter, the obtained experimental results will be presented and discussed in detail. Section 3.1 will be devoted to the fabrication by means of PLD and the *in situ* STM/STS characterization of ZnO, MoS_2 and their heterostructures on top of Au(111). The same experimental approach will be exploited for the investigation of the MoS_2/Ag(111) system (section 3.2) and, eventually, in section 3.3 the results obtained from the preliminary experimental activity related to the growth of 2D silicon by means of PLD will be reported.

3.1 Molybdenum disulphide, zinc oxide and their heterostructures on Au(111)

This section is devoted to the study of ZnO/MoS_2 heterostructures produced by means of PLD on top of a gold substrate. The experimental procedure followed in order to fabricate the ZnO/MoS_2 heterojunctions to be investigated consists in the optimization of the PLD processes employed in order to grow 2D ZnO and 2D MoS_2 on Au(111) and in the exploitation of the optimized deposition processes to produce the desired heterostructures. In particular, it is worth underlining that the fine-tuning of the ZnO and MoS_2 deposition processes has been performed starting from the experimental results previously achieved in our laboratory by Tumino *et al.* [44, 45] and already discussed in section 1.4 and with the aim of achieving a suitable size of the deposited nanostructures, together with an appropriate coverage.

The overall deposition process for the production of the desired heterostructures is based on two subsequent phases, the first one consisting in the deposition and the annealing of the first material (ZnO or MoS_2) and the second one based on the growth and thermal treatment of the other material. Furthermore, as already anticipated, two different strategies have been explored for the production of ZnO/MoS_2 heterostructures: the first method relies on the growth of 2D ZnO on top of Au(111), followed by the deposition of MoS_2 onto the same substrate, whereas the second one consists in the opposite procedure – i.e. 2D MoS_2 growth and subsequent ZnO deposition on top of the same Au surface. These two distinct strategies have been both examined in order to understand whether the deposition of the second material may affect the 2D structures obtained from the growth of the first one. Indeed, the PLD of the second material on top of a system made up of the Au substrate and the previously deposited nanostructures can influence the structure, the morphology and the properties of the overall system because of two different reasons. First, during pulsed laser deposition, high-kinetic energy particles are ejected from the target and impinge on the substrate, thus being able to modify the already grown two-dimensional structures. Second, in order to favour the formation of crystalline and ordered 2D ZnO and 2D MoS_2 nanostructures, PLD has to be followed by a thermal treatment and the optimal annealing atmosphere and temperature are different for ZnO and MoS_2 (with the former requiring a 5 x 10^{-6} mbar O_2 pressure and a lower annealing temperature).
In order to consider all these aspects and to discuss the achieved experimental results, this section will be organized as follows. In section 3.1.1, the optimized PLD processes for the growth of 2D ZnO and 2D MoS_2 will be described and the STM characterization of the grown nanostructures will be briefly discussed. Section 3.1.2 is aimed at showing the results of the structural and morphological investigation of the ZnO/MoS_2 heterostructures produced exploiting the first experimental strategy – i.e. 2D ZnO growth followed by 2D MoS_2 deposition - and at investigating their electronic properties by means of STS. Finally, an equivalent discussion of the experimental results obtained by considering ZnO/MoS_2 heterostructures produced employing the second strategy – i.e. two-dimensional MoS_2 growth and subsequent pulsed laser deposition of 2D ZnO – will be presented in section 3.1.3.

3.1.1 Molybdenum disulphide (MoS_2) and zinc oxide (ZnO) on Au(111)

With the final aim of fabricating ZnO/MoS_2 heterostructures, preliminary experiments have been carried out in order to optimize the deposition processes employed to produce the single 2D materials. In particular, the optimization has been performed in such a way to obtain rather large MoS_2 and ZnO islands but without completely covering the Au(111) substrate and, hence, leaving some portions of the gold surface exposed. This is desirable because, in this way, not only vertical heterostructures (with ZnO on top of MoS_2 or vice versa) can be obtained, but also lateral heterojunctions (with both MoS_2 and ZnO lying on the gold surface and forming an in-plane junction one with the other) can be produced. Furthermore, this is also helpful during the STM characterization of the obtained systems, as it makes possible to evaluate the apparent height of the grown heterostructures with respect to the underlying substrate surface.
After some experiments, the optimal growth processes for both MoS_2 and ZnO at the two-dimensional limit have been established and the optimized experimental parameters have been set. However, it is worth mentioning that, before carrying out the deposition process, the gold substrate has been introduced inside the UHV system and subjected to a cleaning procedure. Usually, it is based on a cycle (consisting in 5 min sputtering performed at room temperature and in an annealing treatment at about 700 K), which is repeated until the Au(111) surface appears sufficiently clean, contamination-free and featuring a regular and ordered herringbone reconstruction (whose presence can be easily checked by means of STM). Then, the substrate can be internally transferred to the deposition chamber, where the PLD process is carried out.

As regards **MoS_2** production by means of PLD, a stoichiometric MoS_2 target has been used in order to deposit 2D MoS_2 nanostructures on top of Au(111). More in detail, the target material has been ablated by 10 laser pulses characterized by an energy of 100 mJ and a laser fluence of 2.5 J/cm^2 and using a repetition rate of 1

Hz in order to accurately control the total number of ablating pulses. Subsequently, the sample has been transferred to the preparation chamber where an annealing treatment has been carried out by keeping the MoS_2/substrate system at a temperature of approximately 730 K for 30 min. The obtained two-dimensional MoS_2 nanostructures can be observed in the STM images of figure 3.1(a)-(b). The majority of the MoS_2 islands formed on top of the gold surface are characterized by an almost triangular shape (sometimes featuring truncated corners) and an average lateral size of the order of 5 – 10 nm, while larger MoS_2 islands (indicated by white arrows in figure 3.1(a)) are found to grow attached to the steps of the Au substrate. As can be clearly seen, all the crystallites feature the hexagonal moiré pattern characteristic of 2D MoS_2 grown on top of Au(111) and characterized by a 3.3 nm periodicity. The apparent height of the considered MoS_2 nanostructures can be measured by means of STM and is ~2 Å, as can be observed from the line profile in figure 3.1(c), while the coverage – i.e. the percentage of the underlying substrate covered by the deposited islands expressed in equivalent monolayers (MLE or, simply, ML) - is approximately 0.15 ML.

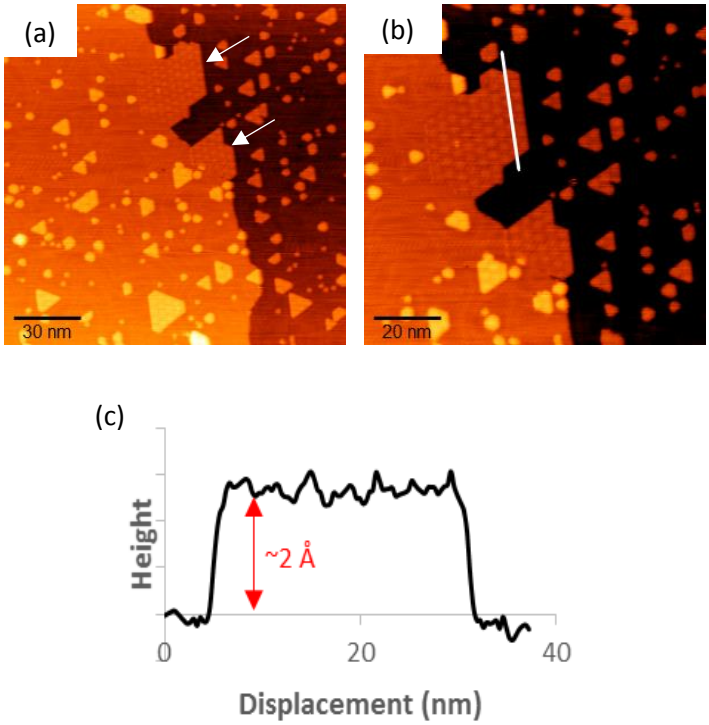

Figure 3.1: (a) STM image (150 nm x 150 nm, V=1.2 V, I=0.35 nA) of MoS_2 islands on top of Au(111). The white arrows mark the presence of large MoS_2 crystallites growing attached to the Au steps. (b) Higher magnification STM image (100 nm x 100 nm, V=1.2 V, I=0.38 nA) of the same sample as in (a). (c) Height profile along the white line in (b).

In the case of **ZnO**, the deposition of the 2D zinc oxide nanostructures has been performed by ablating a stoichiometric ZnO target by means of 20 laser pulses with an energy of 50 mJ per pulse, with a laser fluence of 1.2 J/cm^2 and with a 1 Hz repetition rate. When the PLD process has been completed, the sample has been transferred to the preparation chamber and an annealing treatment has been carried out in two successive steps. Indeed, the first part of the thermal treatment has been performed by keeping the sample at a temperature of ~510 K for 20 min under an O_2 background pressure of 5 x 10^{-6} mbar, while the second step of the annealing process has been carried out in ultra-high vacuum and by keeping the sample temperature constant and equal to ~570 K for 30 min in order to favour the desorption of the excess oxygen. The STM image in figure 3.2(a) shows the morphology of the 2D ZnO nanostructures obtained by means of the just described process. As can be clearly observed, the majority of the ZnO islands are characterized by an almost hexagonal shape and a lateral size of the order of 5 – 10 nm. However, it is worth noting that, together with this rather large ZnO islands, some smaller crystallites (indicated by the black arrows in figure 3.2(b)) can be found on top of the gold substrate: they are characterized by an edge size of 2 – 5 nm and by a less bright

colour contrast in the STM images. Indeed, the brighter hexagonal islands are characterized by an apparent height of 3.5 Å and can be thus associated to bilayer ZnO, while the smaller and darker islands feature a thickness of only 2.3 Å, hence representing monolayer ZnO (figure 3.2(c)). As can be clearly evaluated from the reported STM images, bilayer zinc oxide is surely more abundant than monolayer ZnO, being more stable than single-layer ZnO (as also reported in [42] and [45]). This is due to the fact that the interlayer energy between two ZnO layers is much larger than the interface energy between ZnO and the underlying gold surface. All the observed ZnO islands are characterized by a hexagonal moiré pattern, which is typical for 2D ZnO deposited on top of Au(111) and features the characteristic periodicity of 2.2 nm.

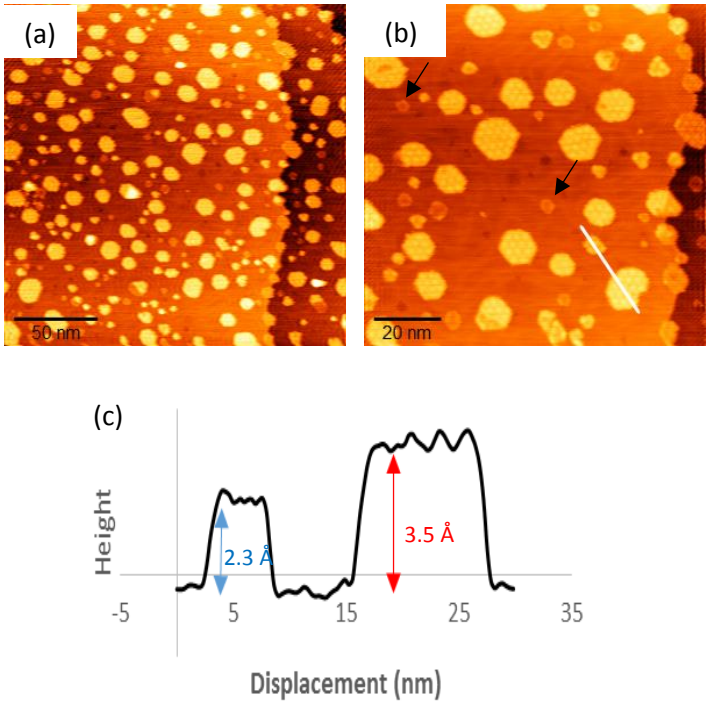

Figure 3.2: (a) STM image (200 nm x 200 nm, V=2 V, I=0.5 nA) of ZnO islands on top of an Au(111) substrate. (b) Higher magnification STM image (100 nm x 100 nm, V=1.93 V, I=0.5 nA) of the same sample shown in (a). The black arrows indicate the presence of smaller and darker islands that can be associated to monolayer ZnO. (c) Height profile along the white line in (b).

As far as the coverage estimate of this kind of system is concerned, it is necessary to consider that the projected area of a bilayer crystallite contributes twice to the calculation of the total coverage. Hence, as the fraction of the substrate area covered by ZnO islands is about 25%, a total coverage of approximately 0.5 ML can be estimated.

In reality, during the preliminary experiments that have brought to the optimization of the ZnO deposition process, other peculiar aspects of the ZnO/Au(111) system have been identified. These particular features can be observed in the STM images of figure 3.3. First, besides the formation of hexagonal and triangular ZnO islands on top of the gold substrate (figure 3.3(a)), the presence of several holes can be observed (see the green arrows in figure 3.3(b)). Second, a strong distortion of the otherwise regular Au(111) herringbone reconstruction (figure 3.3(b)) can be observed, an experimental finding that was already present in previous research activities [41, 45] and also in the case of the MoS_2/Au(111) system [38, 44]. In particular, this last aspect is a peculiarity related to the island growth process on a gold substrate and it has been observed in several systems.

Furthermore, it is worth mentioning another finding (see figure 3.4): when the ZnO deposition has been carried out using 5 laser pulses with an energy of 50 mJ (laser fluence = 0.6 J/cm^2) and the subsequent thermal treatment has been carried out as usual, a strong dishomogeneity in both the morphology and the coverage of the system has been observed while moving from left to right on the substrate surface for a distance in

the order of 1 cm. In particular, on the left side of the Au surface, rather large but isolated ZnO islands are present (figure 3.4(a)) whereas, moving towards the right side of the substrate surface, the average size of the islands increases, the islands start to coalesce (figure 3.4(b)) and finally an almost continuous bilayer ZnO film is formed (figure 3.4(c)-(d)). This morphological modification is also accompanied by a gradual increase in the coverage, ranging from ~0.8 ML (on the left) to ~1.8 ML (on the right). The reason for this gradient in the ZnO coverage (and hence morphology) may be the relative position between the plasma plume generated during the PLD process and the substrate. More in detail, if the substrate is not placed right in front of the laser spot, the ablated material may be non-uniformly distributed on top of the substrate itself, thus resulting in a larger amount of deposited material on one side and in a lower amount of material on the other side.

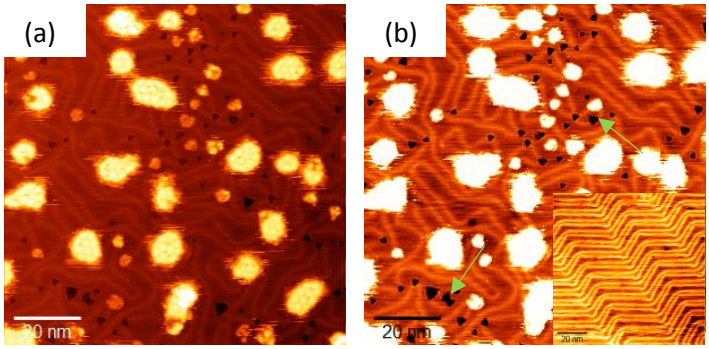

Figure 3.3: (a) STM image (100 nm x 100 nm, V=2.3 V, I=0.4 nA) of ZnO islands on top of Au(111). The PLD process has been carried out by means of 15 laser pulses (energy = 50 mJ, laser fluence = 1.2 J/cm^2), then followed by 20 min annealing in O_2 and 30 min thermal treatment under UHV conditions. (b) Same STM image as in (a), in which the colour contrast has been properly modified in order to highlight the presence of the holes in the substrate (marked by the green arrows) and the distortion of the usually regular herringbone reconstruction. The inset is an STM image (100 nm x 100 nm, V=0.5 V, I=0.5 nA) showing the ordered herringbone reconstruction that is typical of a clean Au(111) surface.

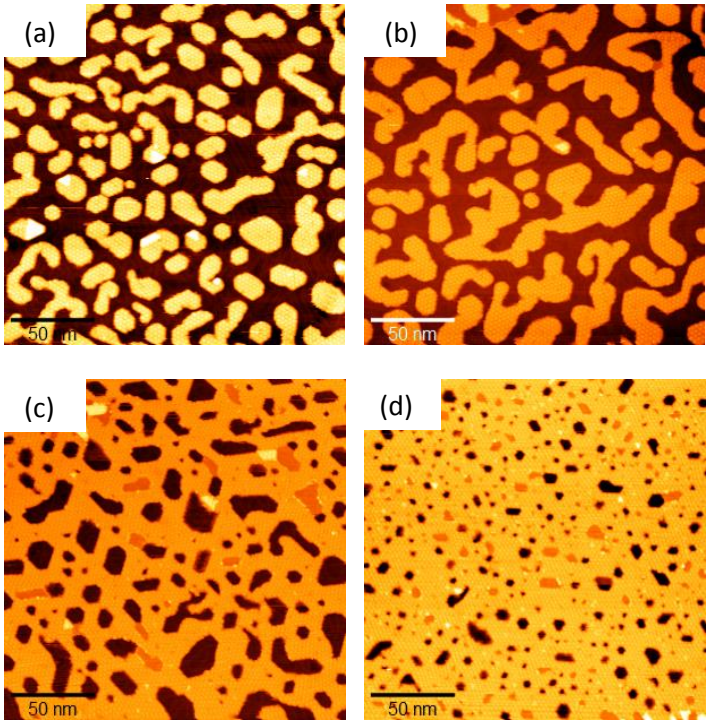

Figure 3.4: STM images (200 nm x 200 nm) of ZnO deposited on top of Au(111) and showing the gradual variation in the coverage and in the morphology occurring as you move from the left side (a) to the right side (d) of the investigated substrate. More in detail, the ZnO coverage is: ~0.8 ML in (a) (V=1.8 V, I=0.3 nA), ~1 ML in (b) (V=1.8 V, I=0.3 nA), ~1.4 ML in (c) (V=1.5 V, I=0.3 nA) and ~1.8 ML in (d) (V=1.5 V, I=0.3 nA).

In conclusion, since the final aim of this experimental activity is to build ZnO/MoS_2 heterostructures, it would be interesting to evaluate whether the annealing treatment typically performed for achieving ordered and crystalline ZnO and MoS_2 nanostructures on Au(111) produces relevant and appreciable changes on the other material.

In order to investigate the **effect of the thermal treatment** typical of ZnO on two-dimensional MoS_2, 2D MoS_2 nanostructures grown on top of Au(111) exploiting the previously described deposition procedure are subjected to a thermal treatment consisting in 20 min annealing at 510 K and under a 5 x 10^{-6} O_2 pressure and in 30 min annealing at 570 K under UHV conditions. Subsequently, the sample has been characterized by means of STM. No appreciable differences can be observed (compare the STM image of figure 3.5(a) with the one in figure 3.1(a)) and this is true even at the atomic scale (as can be appreciated by considering the atomic-resolution STM image of figure 3.5(b)). Hence, it is possible to conclude that MoS_2 deposited on top of Au(111) represents a rather inert system that is almost unaffected by the thermal treatment and the O_2 exposure. The rather good chemical stability and inertness of two-dimensional MoS_2 has been also reported in previous literature works (such as in the research activity by Grønborg *et al.* [38]), in which 2D MoS_2 has been demonstrated to be relatively stable under air exposure.

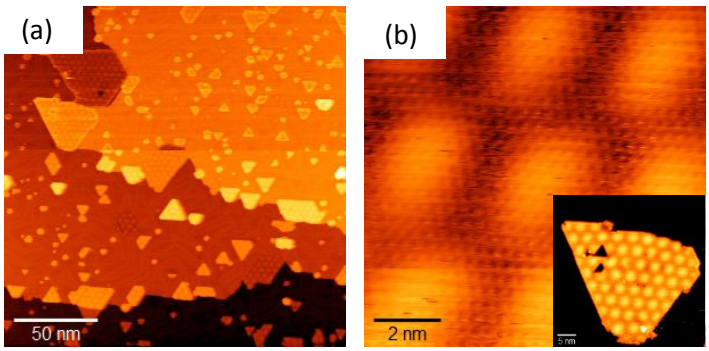

Figure 3.5: (a) STM image (200 nm x 200 nm, V=1.3 V, I=0.38 nA) of the sample shown in figure 3.1, which has been subjected to 20 min annealing at 510 K under a 5 x 10^{-6} mbar O_2 pressure, followed by 30 min annealing at approximately 570 K under UHV conditions. (b) Atomic-resolution STM image (10 nm x 10 nm, V=0.5 V, I=0.5 nA) of the MoS_2 island shown in the inset. The inset is the STM image (40 nm x 40 nm, V=1.3 V, I=0.38 nA) of a large triangular MoS_2 island growing attached to a step of the gold surface.

On the contrary, 2D ZnO nanostructures have not been subjected to the annealing treatment typically performed in the case of low-dimensional MoS_2 on Au(111). Indeed, according to some experimental studies present in the literature (such as [42]), ZnO is not very stable at high temperature and a thermal treatment at temperatures higher than 575 K can cause the desorption of the material from the substrate surface, thus resulting in a strong decrease in the coverage. Hence, it is possible to suppose that the 730 K annealing treatment typical of 2D MoS_2 will largely affect the structure and morphology of 2D zinc oxide nanostructures.

All these experimental results can be very useful in order to produce the desired ZnO/MoS_2 heterostructures. In particular, from the consideration of the effect of the thermal treatments, it is possible to assume that the most promising approach for the fabrication of ZnO/MoS_2 heterostructures is the one based on the deposition of MoS_2 followed by the growth of ZnO on top of the same Au substrate. Indeed, while ZnO is supposed to be strongly perturbed by both the PLD and the annealing treatment of MoS_2, 2D MoS_2 nanostructures have demonstrated to be practically unaffected by the thermal treatment typical of ZnO, even though the ZnO deposition process can cause a certain modification of these two-dimensional structures.

Despite this, both the approaches have been explored to build the desired heterostructures and some experimental attempts have been made, finally resulting in the deposition of ZnO/MoS_2 heterostructures on top of an Au(111) substrate. The structural and morphological characterization and the investigation of the

electronic properties of the produced heterostructures have been performed by means of a scanning tunneling microscope and will be discussed in the following sections.

3.1.2 ZnO/MoS_2 heterostuctures on Au(111) – first deposition strategy (ZnO deposition followed by MoS_2 growth)

The first and less promising experimental strategy – i.e. the one considered in this section - consists in four different steps:

1. PLD of ZnO on top of a clean Au(111) substrate, which is carried out using 20 laser pulses, an energy of 50 mJ per pulse, a laser fluence of 1.2 J/cm^2 and a 1 Hz repetition rate;
2. internal transfer of the sample to the preparation chamber and thermal treatment, consisting in keeping the temperature at ~510 K for 20 min under an O_2 background pressure of 5 x 10^{-6} mbar and then in maintaining the sample temperature at 570 K for 30 min under UHV conditions;
3. PLD of MoS_2 onto the same substrate, performed employing 10 ablating pulses, 100 mJ energy per pulse, a laser fluence of 2.5 J/cm^2 and a repetition rate of 1 Hz;
4. internal transfer of the sample to the preparation chamber and annealing treatment during which the temperature of the system is kept constant at a value of approximately 730 K for 30 min.

Subsequently, the sample is internally transferred to the analysis chamber, where STM and STS measurements are carried out.

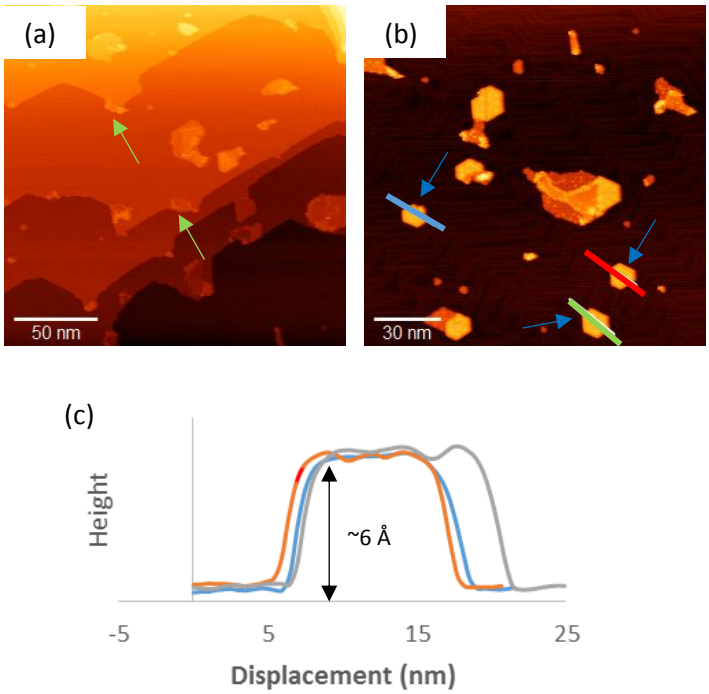

Figure 3.6: (a) STM image (200 nm x 200 nm, V=1.5V, I=0.4 nA) of the system obtained by depositing ZnO and MoS_2 on top of the same Au(111) surface. The green arrows mark the presence of very small structures growing attached to the gold step edges. (b) Higher magnification STM image (150 nm x 150 nm, V=1.5 V, I=0.4 nA) of the same sample shown in (a). The blue arrows indicate some polygonal and ordered islands that reasonably consist of one single material. (c) Height profiles along the blue, green and red lines shown in (b).

The **structure and morphology** of the obtained system can be observed in the STM images in figure 3.6(a)-(b). Indeed, it is possible to recognize the presence of large structures that seem to be made up of a mixture of the two different deposited materials (ZnO and MoS_2), smaller islands featuring a polygonal shape and even smaller structures growing attached to the step edges of the underlying gold substrate (see the green arrows in figure 3.6(a)). In the framework of this experimental activity, attention will be focused on the mixed structures investigation. However, it is worth mentioning that the smaller polygonal crystallites (such as

those marked by the blue arrows in figure 3.6(b)) seem to be made up of one single material (either ZnO or MoS_2), since both their morphology and the presence of a moiré superstructure on their surface are compatible with what has been observed when ZnO and MoS_2 have been grown individually on Au(111). Nevertheless, the apparent height measured by STM (see the line profiles in figure 3.6(c)) is approximately 6 Å – i.e. much larger than the apparent thickness measured in the case of both single-layer MoS_2 and bilayer ZnO. Hence, it is not possible to identify clearly the nature of these ordered structures and only hypothesis can be made. For instance, these rather thick islands might represent bilayer MoS_2. Nonetheless, previous literature works related to the STM investigation of the MoS_2/Au(111) system (such as [44]) reported that the thickness of a bilayer MoS_2 island is ~8 Å, resulting from the sum between the height of a MoS_2 monolayer (~2 Å) and an interlayer spacing in the order of 6 Å – i.e. in accordance with the 6.15 Å MoS_2 bulk interlayer distance. Furthermore, this hypothesis is not so plausible because MoS_2 tends to form monolayers on top of Au(111) and the growth of the material typically occurs layer-by-layer and not through the formation and coalescence of 3D islands. Another possible route that can be followed in order to identify these polygonal islands relies on the consideration of the periodicity of the moiré pattern that is clearly visible on their surface. Indeed, the moiré superstructures of ZnO and MoS_2 feature a different periodicity (which is 2.2 nm in the case of ZnO and 3.3 nm in the case of MoS_2) and thus can be used to identify the nature of these structures. In this case, it is possible to extrapolate a periodicity of the moiré pattern in the order of 3 nm, hence confirming that these small, polygonal and ordered structures may be made up of MoS_2 rather than ZnO, an interpretation that will be also supported by the acquired STS spectra.

Another very peculiar feature deserving to be mentioned is the distortion of the Au(111) herringbone reconstruction resulting as a consequence of the deposition process. This aspect can be appreciated by observing the STM images in figure 3.7(a)-(b). Indeed, the characteristic lines of the herringbone reconstruction clearly appear to be distorted in the proximity of the deposited islands, while they seem to be rather ordered and regular far from the grown structures. In particular, these lines seem to deviate in order to avoid the islands and they seem to not be present right below them. A similar situation has already been observed in other and different systems, such as in the case of MoS_2 islands deposited on top of Au(111) [38, 44] and in the ZnO/Au(111) system, as already mentioned in section 3.1.1.

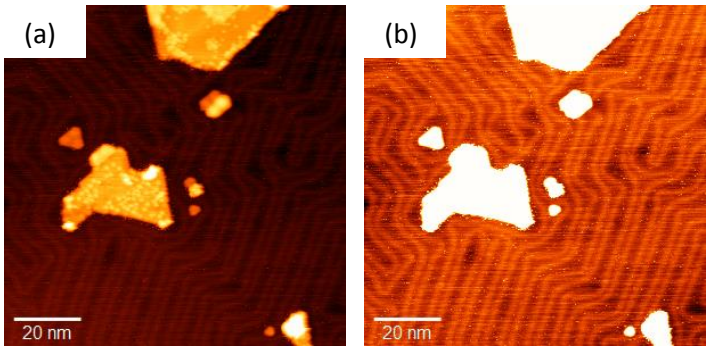

Figure 3.7: (a) STM image (100 nm x 100 nm, V=1.5 V, I=0.4 nA) of two-dimensional ZnO/MoS_2 structures deposited onto Au(111). (b) Same image as in (a), in which the colour contrast has been properly modified in order to emphasize the distortion of the usually regular herringbone reconstruction.

The STM images reported in figure 3.8(a)-(b) show two examples of mixed structures, which have been observed on top of the gold substrate after the previously described experimental procedure. Both structures are made up of three distinct regions featuring very different structural and morphological properties and, hence, it could be useful to describe a bit more in detail each of these parts separately.

The brightest regions of the two considered islands (labelled as “1” in figure 3.8(b)) are characterized by an ordered structure, whose surface features the presence of a periodic moiré pattern (even though it is not clearly visible in the STM images of figure 3.8(a)-(b)). They seem to be very similar to the isolated polygonal islands described previously in terms of both morphology and apparent height, which is approximately equal

to 6 Å (as can be evaluated from the line profile in figure 3.8(d)). Sometimes, these regions feature the presence of line defects (see the black arrow in figure 3.8(a)) that can be considered as boundaries due to the junction between two similar islands and that seem to be equivalent to the line defects observed during the study of the MoS_2/Au(111) system and due to the meeting and joining of two MoS_2 islands characterized by the same edge type [44].
On the contrary, the darkest regions (marked as "2" in figure 3.8(b)) feature a very peculiar morphology since their surface appears to be covered by very small granular structures (indicated by the white arrow in the higher resolution STM image of figure 3.8(c)). Other regions (labelled as "3" in figure 3.8(b)) are characterized by a flat and smooth surface and an apparent height of approximately 4.5 Å (see the line profile in figure 3.8(d)).

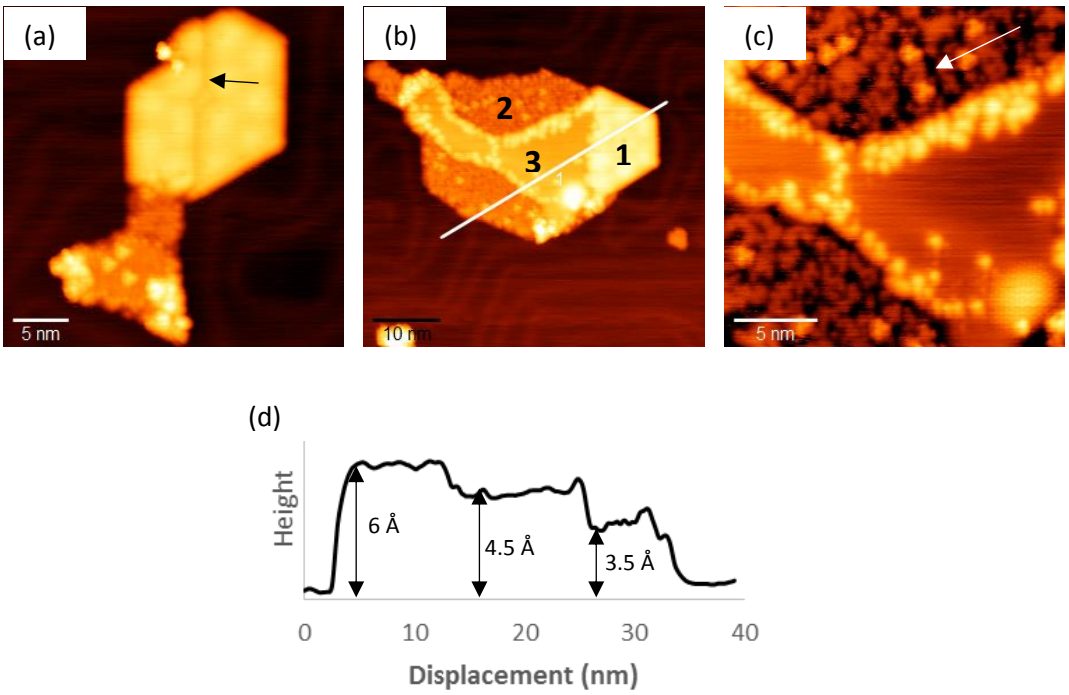

Figure 3.8: (a) STM image (30 nm x 30 nm, V=1.5 V, I=0.4 nA) of a mixed ZnO/MoS_2 structure on top of Au(111). The black arrow marks the presence of a line defect generated due to the meeting and joining of two islands of the same type. (b) STM image (50 nm x 50 nm, V=1.5V, I=0.4 nA) of another ZnO/MoS_2 island on top of a gold substrate. The labels "1", "2" and "3" indicate three distinct regions of the investigated structure. (c) Higher resolution STM image (20 nm x 20 nm, V=0.7 V, I=0.5 nA) of the same island shown in (b). The white arrow marks the presence of very small granular structures. (d) Height profile along the white line in (b).

Finally, it is worth noting that the different regions present in the same mixed structure are linked by means of some sort of in-plane junction. These junctions can be observed in figure 3.8(c): they appear very bright and in turn characterized by a particular structure formed by very small granular features.
Only relying on the topographic information extracted from the experimentally acquired STM images, it is very difficult to speculate about the chemical composition of the different island regions and to understand whether a specific region consists in ZnO or MoS_2. This because the majority of the observed morphological features have never been observed in previously reported literature works and, in addition, there is the possibility that the two ablated materials do not remain completely separated once deposited on top of the same substrate but may form an alloy or an intermixed compound. Thus, as the structural and morphological characterization of the obtained system is not so simple, STS measurements have been carried out in order to exploit the differences in the electronic properties of the different regions of the grown islands to try to identify their nature.

In the framework of this research activity, **STS measurements** have been carried out by applying a voltage ramp in the range between 2.5 V and -2.5 V (in order to investigate a range of few eV around the Fermi level) and all the different structures that can be found of top of the gold substrate have been investigated. Indeed, STS measurements and, in particular, the differential conductivity curves, provide useful information about the surface local electronic properties and, hence, they can be helpful for the investigation of the nature of the different structures and of the different regions forming the mixed islands observed onto Au(111). The resulting STS spectra are shown in figure 3.9, together with a reference STM image showing the three different regions of the mixed islands that have been investigated by means of scanning tunneling spectroscopy.

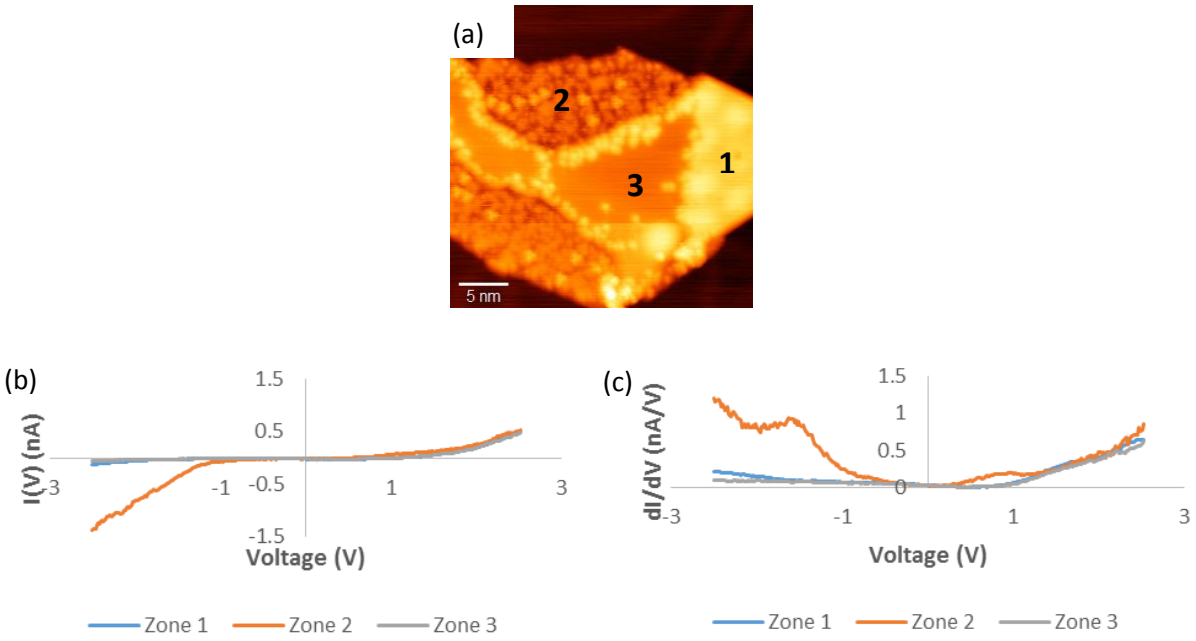

Figure 3.9: (a) Reference STM image (30 nm x 30 nm, V=0.7 V, I=0.5 nA) showing the three different structures found on top of the Au(111) substrate and investigated by means of STS. (b) I(V) curves of the regions marked as "1", "2" and "3" in (a). Acquisition set-point: V=2.5 V, I=0.5 nA. (c) Corresponding dI/dV spectra, which have been properly rescaled in order to adapt them to the numerical derivative of the related I(V) curve.

The first zone to be investigated is the bright region marked as "1" in the STM image of figure 3.9(a), which is characterized by a regular and ordered structure and features the presence of a periodic moiré pattern. From the corresponding STS spectra (blue curves in figure 3.9(b)-(c)) an electronic band gap of the order of 2 eV can be extrapolated since the valence band maximum (VBM) and the conduction band minimum (CBM) occur at -1.5 V and +0.5 V, respectively. Indeed, within the investigated voltage range, it is possible to recognize in the dI/dV spectrum (blue curve in figure 3.9(c)) the presence of a region in which the differential conductivity is zero or almost zero. The width of this region approximately corresponds to the size of the band gap of the material, while its edges occur in correspondence of the VBM and of the CBM. In reality, it would be easier to identify the VB and CB edges by considering the I(V) spectrum (blue curve in figure 3.9(b)) due to the fact that it is characterized by a slope change in correspondence of the VB and CB edges while its value is zero or very close to zero in the gap region. This experimental finding is compatible with the results of the STS measurements that have been achieved by Tumino *et al*. [44] during the research activity regarding the growth of two-dimensional MoS_2 on Au(111). Hence, it is possible to identify these bright and ordered regions found on the sample surface as small MoS_2 islands that have been formed during the second PLD process and that have grown without being affected by the presence of the previously deposited two-dimensional ZnO structures. In particular, considering both the morphological and the electronic information, it is possible to suppose that these islands represent bilayer MoS_2 structures that are laterally connected to

ZnO, while it can be excluded a situation in which 2D MoS_2 has been deposited on top of an already existing ZnO structure.
Other relevant information that can be extracted from the STS spectra acquired on region "1" are the fact that the Fermi level is closer to the CB edge rather than being right in the middle of the energy gap and that a non-zero differential conductivity is present in the gap region. The former feature can be a hint of the n-type character of 2D MoS_2 grown on top of Au(111) due to charge transfer phenomena occurring at the interface between the deposited two-dimensional material and the underlying gold substrate, while the latter one suggests a slight metallization of 2D MoS_2 onto Au(111) [44].
The second region characterized by means of STS measurements is the dark one labelled as "2" in the reference STM image of figure 3.9(a). The corresponding I(V) and dI/dV data are represented by the orange curves in figure 3.9(b) and in figure 3.9(c), respectively. By analysing the differential conductivity curve an electronic band gap of approximately 1.5 eV can be estimated. This value of the band gap results from the fact that the VB edge occurs at about -1 V, while the CBM can be identified in correspondence of a voltage value of +0.5 V. Nonetheless, only relying on this information and on the previously discussed morphological characterization, it is not possible to clearly identify the nature and chemical composition of these zones of the mixed islands. Indeed, both the morphological and the electronic properties exhibited by these regions are very peculiar and do not correspond to anything already observed by other researchers or in previous experimental activities carried out in our laboratory. Hence, a further and deeper investigation is necessary in order to definitely understand their structure and chemical composition, also because it is highly probable that these regions are characterized by a complex chemical composition due to the alloying or intermixing of the two deposited compounds (ZnO and MoS_2) or by an inhomogeneous surface structure, which can cause a modification of the DOS and, hence, of the dI/dV curve.
Finally, the last analysed region is the one marked as "3" in figure 3.9(a), which seems to be characterized by a smooth and flat surface. Similarly to the previous case, the analysis of the STS spectra acquired on these zones of the sample surface is not so simple, especially for negative voltages, because the VBM is just included in the investigated voltage range. By considering the related dI/dV curve (grey line in figure 3.9(c)), it is possible to estimate a 2.8 eV band gap, a value that is comparable with that observed during the investigation of the ZnO/Au(111) system carried out by Stavale *et al*. [41]. Another experimental finding that can support the interpretation of these apparently flat islands as 2D zinc oxide structures can be derived from the corresponding I(V) curve (grey line in figure 3.9(b)). Indeed, by considering the voltage values in correspondence of which a change in the curve slope can be observed, the VB and CB edges seem to occur at -2 V and +0.8 V, respectively, exactly as reported in [41]. Furthermore, other relevant information can be extrapolated from the acquired STS spectra: the non-zero tunneling conductivity in the gap region and the pinning of the Fermi level near the CBM. Both these features are due to the surface interaction and charge transfer occurring at the interface between the overlayer and the underlying gold substrate, thus resulting in a slight metallization and in a n-type conductance behaviour of the deposited material on top of Au(111).

3.1.3 ZnO/MoS_2 heterostuctures on Au(111) – second deposition strategy (MoS_2 deposition followed by ZnO growth)

After the detailed discussion about the STM/STS characterization of samples obtained exploiting the first experimental strategy, structures grown on top of an Au(111) substrate by means of the second and more promising experimental procedure can be considered and investigated. This second production method is based on:

1. PLD of MoS_2 on top of a clean Au(111) substrate, by means of 10 laser pulses and using an energy of 100 mJ per pulse, a laser fluence of 2.5 J/cm^2 and a 1 Hz repetition rate;
2. internal transfer of the sample to the preparation chamber and annealing treatment (carried out at 730 K for 30 min);

3. ZnO deposition onto the same substrate by means of PLD, employing 20 ablating pulses (energy per pulse: 50 mJ, laser fluence = 1.2 J/cm^2, repetition rate: 1 Hz);
4. internal transfer of the sample to the preparation chamber and two-step thermal treatment, considering that the first part of the annealing process is performed at 510 K for 20 min under an O_2 background pressure of 5 x 10^{-6} mbar while the second part is carried out by keeping the sample at a temperature of ~570 K for 30 min in UHV conditions.

The obtained structures can be observed in the STM images reported in figure 3.10. The **morphology** of the obtained system is quite different from that characteristic of the samples produced with the previously described experimental approach. Indeed, though some small islands featuring a polygonal and quite ordered structure are present (see the blue arrows in figure 3.10(b)), the majority of the 2D structures grown on the Au(111) substrate are characterized by a rather large size and by the presence of surface spherical features. A peculiar aspect is the distortion of the usually regular herringbone reconstruction (not shown), which is present also in the samples prepared using the first considered experimental procedure.

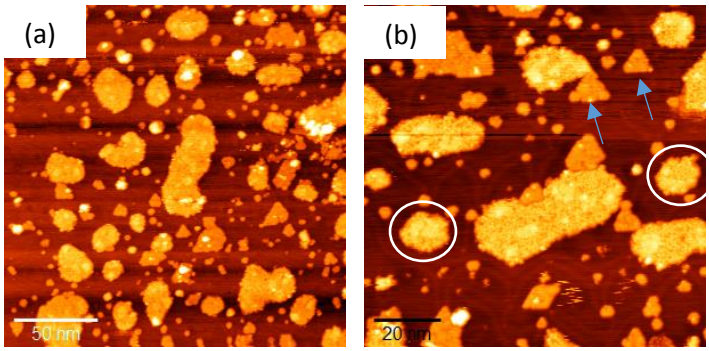

Figure 3.10: (a) STM image (200 nm x 200 nm, V=2.5 V, I=0.4 nA) of the sample obtained by depositing MoS_2 and subsequently ZnO on top of the same Au(111) substrate. (b) STM image (100 nm x 100 nm, V=2.4 V, I=0.4 nA) of the same sample shown in (a). The white circles indicate some large islands characterized by an almost hexagonal shape. The blue arrows mark the presence of small islands, mainly featuring a triangular shape and a different structure and morphology with respect to the larger and brighter ones.

Let us now consider in detail the morphology and structure of the observed islands (figure 3.11(a)-(b)).
The smaller and darker islands (indicated by blue arrows in figure 3.10(b)) feature polygonal shapes, even though most of them are characterized by an almost triangular shape. However, their structure is not so regular in the sense that their surface appears to be quite disordered (without any moiré pattern) and the same is true for the island edges. Nonetheless, they are characterized by an apparent height of the order of 3 Å (as can be evaluated by considering the line profiles in figure 3.11(c)-(d)) and this experimental finding is compatible with the thickness of a MoS_2 monolayer.
On the contrary, the larger and brighter islands are characterized by a rather irregular shape (especially at the edges), even if sometimes it is possible to recognize the presence of structures with an almost hexagonal shape (see, for instance, the white circles in figure 3.10(b)). Their surfaces are covered by ball-like features, which give a very bright contrast in the STM images and seem to be not regularly arranged on top of the surfaces themselves. The thickness of these very peculiar structures can not be easily determined due to the presence of the surface spherical protrusions and an average height of approximately 4 Å can be estimated by simply considering the line profiles in figure 3.11(c)-(d).
However, the investigated samples feature very peculiar morphological and structural characteristics, which have never been observed in previously reported literature works, thus making very difficult the identification of ZnO and MoS_2 on top of the gold substrate and the association of a specific kind of structure with one of the two deposited materials. Other characterization tools can be exploited to better understand the nature of the grown structures; in particular, STS measurements can be very useful as they can help in the identification of the materials through the consideration of their electronic properties.

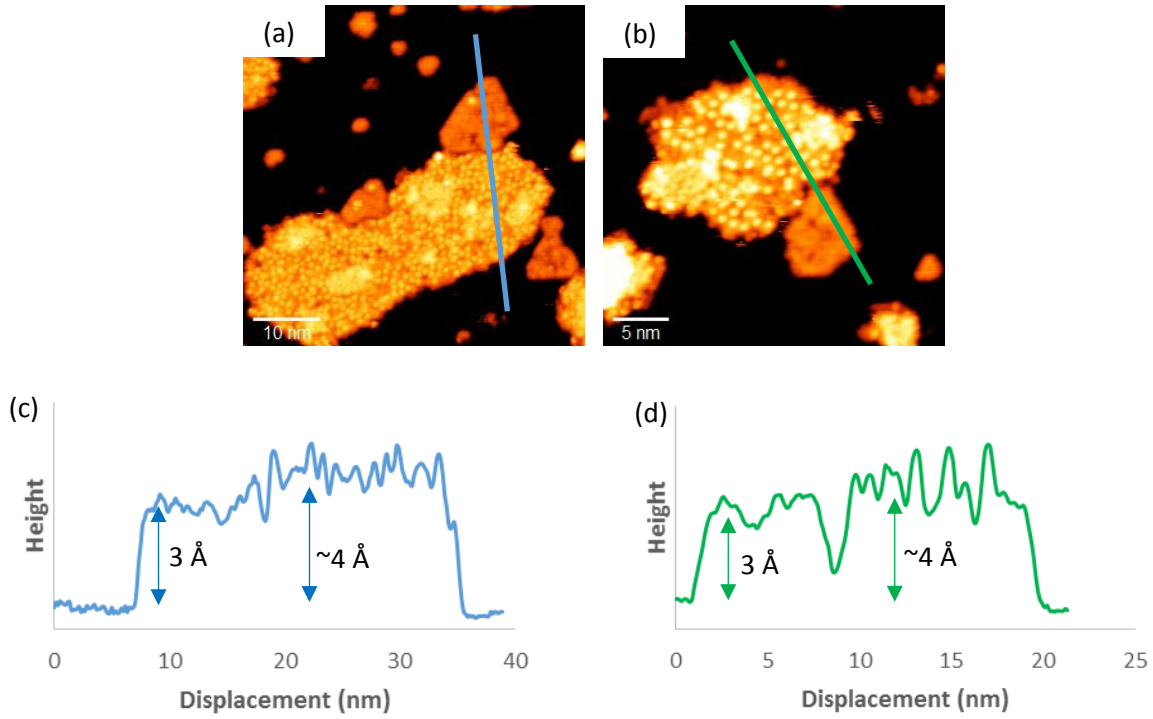

Figure 3.11: (a) STM image (50 nm x 50 nm, V=2.4 V, I=0.4 nA) of one of the structures formed on top of the Au(111) substrate after MoS_2 and ZnO deposition. (b) STM image (30 nm x 30 nm, V=2.4 V, I=0.4 nA) of another structure observed on top of the gold surface. (c) Height profile along the blue line in (a). (d) Height profile along the green line in (c).

In the framework of this research activity, **STS** spectra have been acquired by applying a voltage ramp in a range between 3 V and -2.5 V in such a way that information about the electronic properties of the samples can be extrapolated and considering that attention will be particularly focused on the size of the energy gap and on the positions of the VB and CB edges.

The STS spectra obtained for the two different types of islands that can be distinguished onto Au(111) are shown in figure 3.12, together with a reference STM image in which the two investigated zones are marked as “1” and “2”, respectively.

The I(V) and dI/dV curves shown in blue in figure 3.12(b)-(c) have been acquired on the bright islands characterized by the presence of small spherical features on their surface and labelled as “1” in figure 3.12(a). An electronic band gap value of the order of 3.5 eV can be estimated from the differential conductivity curve plotted in blue in figure 3.12(c) and this band gap size can be also confirmed by identifying the position of the VB and CB edges from the corresponding I(V) curve in figure 3.12(b). Indeed, the VBM is found to occur at approximately -2 V, while the CBM seems to take place at +1.5 V. These experimental findings can be compared to the experimental results achieved by Tumino *et al.* [45] during the STM/STS investigation of the ZnO/Au(111) system. Indeed, a band gap of the order of 3.5 eV is very similar to the energy gap value that is usually found either in the case of multilayer ZnO nanostructures (and, in particular, starting from the 4^{th} layer) or in the case of bulk ZnO. However, the apparent height of these islands – i.e. ~4 Å – is compatible with a bilayer situation. Thus, it is possible to conclude that these structures are made up of bilayer ZnO, even though their surfaces are characterized by the presence of possible contaminations or structural modifications (causing, for instance, the absence of a regular moiré pattern) that may also affect the energy gap of the material.

On the contrary, as regards the characterization of the electronic properties of the darker and smaller islands present on the Au(111) surface under investigation and marked as “2” in the STM image of figure 3.12(a), the I(V) and dI/dV curves plotted in orange in figure 3.12(b)-(c) have to be analysed. First of all, it is possible to notice that these STS spectra are very similar to those reported in figure 3.9(b)-(c) (blue lines), thus suggesting that the investigated islands are made up of two-dimensional MoS_2. This assumption is also

confirmed by the fact that an electronic band gap of approximately 2 eV can be evaluated from the differential conductivity spectrum of figure 3.12(c) (orange line) and, moreover, by the fact that the positions of the VBM and CBM are those typical of 2D MoS_2 – i.e. -1.5 V and +0.5 V, respectively. Furthermore, the slight metallization and the n-type conductance behaviour that are typical of 2D MoS_2 on top of Au(111) can be recognized considering the non-zero tunneling conductivity in the gap region and the pinning of the Fermi level near the conduction band edge.

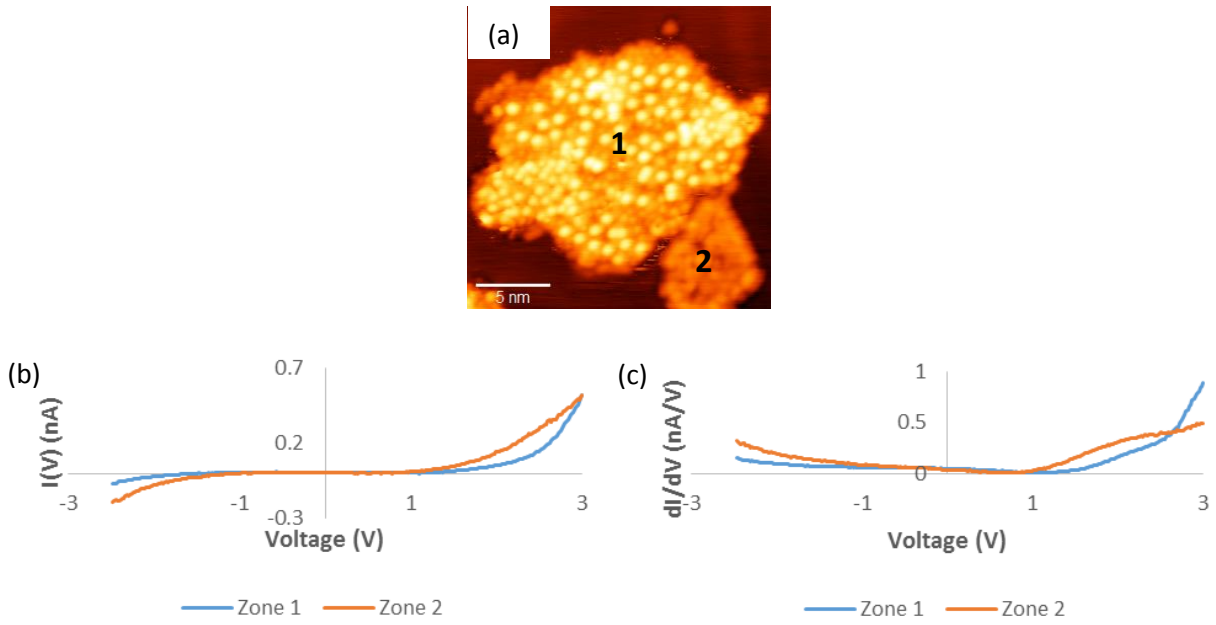

Figure 3.12: (a) Reference STM image (20 nm x 20 nm, V=1.5 V, I=0.4 nA) showing the two different regions of the ZnO/MoS_2 structures found on top of the Au(111) substrate and investigated by means of STS. (b) I(V) curves of the regions marked as "1" and "2" in (a). Acquisition set-point: V=3 V, I=0.5 nA. (c) Corresponding dI/dV spectra, which have been properly rescaled in order to adapt them to the numerical derivative of the related I(V) curves.

To summarize, both the investigated experimental strategies have demonstrated to be able of producing systems characterized by the coexistence of 2D MoS_2 and 2D ZnO on top of the same Au substrate. Furthermore, the formation of heterostructures of the two deposited materials have been observed, even though they are not characterized by an ordered and regular structure and it is not always easy to associate one single material to a specific region of the analysed samples. Nonetheless, the conducted experimental activity has brought to some relevant experimental findings, which could be taken as the starting point for a future and deeper research activity.

First, almost ordered and regular MoS_2 islands are formed onto Au(111) employing both the experimental strategies, thus confirming that MoS_2 is only little affected by the ZnO deposition. Indeed, when MoS_2 is deposited as the first material, it is influenced by the subsequent ZnO deposition in a limited way, only resulting in a scarce disordering of the MoS_2 structure and morphology and in the disappearance of the moiré pattern. On the contrary, when MoS_2 is deposited as the second material, the 2D MoS_2 nanostructures seem to grow without feeling the presence of the previously deposited zinc oxide and forming ordered and polygonal islands, either isolated on top of the gold substrate or generating an in-plane junction with ZnO.

Second, STS measurements reveal peculiar electronic features that are displayed by samples fabricated using both the experimental procedures and even by all the different structures that can be identified onto the Au substrate. Indeed, all the investigated structures are characterized by a non-zero tunneling conductivity in the gap region and by a more or less relevant pinning of the Fermi level near the CB edge, thus suggesting that the underlying Au(111) substrate is able to induce the metallization of the overlayer and the uprising of a n-type conductance behaviour of the material independently on the specific nature of the overlayer itself.

Finally, it is possible to confirm that, so far, the most promising experimental strategy remains the one based on the deposition of 2D MoS_2 followed by ZnO growth on top of the same gold surface. Indeed, this procedure allows to obtain only two different types of structures, considering that one kind of structure can be quite surely identified with two-dimensional MoS_2 islands and the other one can be associated to bilayer ZnO. Moreover, the in-plane junction between the two types of structures seems to be quite simple and easy to investigate. On the contrary, the other experimental strategy – i.e. consisting in depositing first ZnO and then MoS_2 – should be considered as the less promising one since it brings to the formation of several different structures, forming complex junctions when connected one to the other.
In conclusion, however, it is worth noting that the produced ZnO and MoS_2 structures may be subjected to relevant structural modifications due to the performed PLD processes. Hence, since the surface structures of the two deposited materials are not those obtained when depositing ZnO and MoS_2 individually, the investigation of chemical composition, morphology and structure of the fabricated samples is a non-trivial task that will require further and deeper investigation, probably exploiting other characterization tools (such as, for instance, Raman spectroscopy), able to provide additional information about the studied structures.

3.2 Two-dimensional molybdenum disulphide nanostructures on Ag(111)

This section is dedicated to the production and characterization of 2D MoS_2 nanostructures on top of an Ag(111) substrate. The starting point of this experimental activity is represented by the work done by Tumino *et al*. [44] in our laboratory and related to the pulsed laser deposition of two-dimensional MoS_2 on Au(111) and to the characterization of the obtained low-dimensional structures mainly by means of STM. Indeed, during their research activity, Tumino and co-workers have investigated both the morphology and the electronic, optical and vibrational properties of MoS_2 deposited onto a gold surface and have discovered that the interaction with the underlying substrate strongly influences the properties of the MoS_2 overlayer. This aspect can be appreciated by considering the experimental results that have been obtained during STS, Raman spectroscopy and PL measurements (see [44] for more details). Hence, it would be very interesting to deposit and characterize MoS_2 on top of other metallic substrates in such a way to deeply understand the effect of the substrate itself on the modification of the properties of the two-dimensional material, which are also affected by the quantum confinement effects arising when a material is spatially confined (at least along one direction).
In the framework of this thesis work, three depositions of two-dimensional MoS_2 on top of a silver substrate have been carried out by means of PLD in order to gradually increase the amount of deposited material and, hence, the coverage. The employed PLD processes consist in the ablation of a stoichiometric MoS_2 target (99.99% pure) by means of 10, 30 and 50 laser pulses, respectively, and using an energy of 100 mJ per pulse and, hence a laser fluence of 2.5 J/cm^2. The depositions have been performed in a UHV chamber (base pressure $<10^{-9}$ mbar) and, then, the obtained samples have been internally transferred to another chamber where a post-deposition annealing treatment has been carried out in order to favour the ordering and crystallization of the deposited material. Subsequently, STM/STS measurements have been carried out under UHV conditions to investigate the structure, morphology and electronic properties of the obtained systems (sections 3.2.1 and 3.2.2). In addition, the samples obtained by means of 30 and 50 ablating laser pulses have been extracted from the ultra-high vacuum system in order to be further studied exploiting *ex situ* Raman spectroscopy and PL measurements. The results of these analyses will be discussed in section 3.2.3, together with those of the AES measurements that have been performed both before extracting the samples from the UHV system in order to verify the chemical composition of the deposited material and after having replaced the samples inside the system in order to evaluate the presence of contaminants due to some hours air exposure.

3.2.1 Morphological characterization of MoS_2 nanostructures

Before performing PLD to produce MoS_2 at the two-dimensional limit, the Ag(111) substrate has to be introduced inside the UHV system and cleaned in order to eliminate all the contamination that may be present on its surface. The typical cleaning procedure that is performed in order to obtain a clean Ag(111) surface consists in several cycles of sputtering (using Ar^+ ions with an energy of 1 – 1.5 keV) and annealing at a temperature in the range 670 – 720 K and it is very similar to that used in the case of the Au(111) substrates. The clean Ag(111) surface can be observed in the STM images of figure 3.13(a)-(b), where it appears to be flat (without featuring the peculiar herringbone reconstruction typical of the Au(111) surface). However, the silver substrate features the presence of some steps, which are characterized by an apparent height (measured by means of STM) in the order of ~3 Å, as can be clearly evaluated from the height profile in figure 3.13(c). Furthermore, another peculiar feature deserves to be mentioned: the step edges of the Ag(111) surface seem to be fuzzy (see figure 3.13(b)) but, in reality, their aspect is simply related to the mobility of the Ag atoms forming the steps, which is rather high even at room temperature.

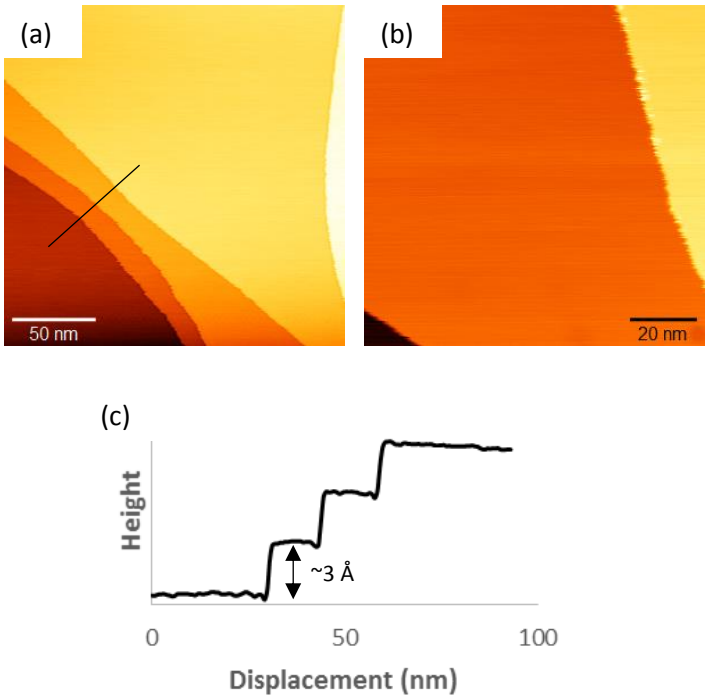

Figure 3.13: (a) STM image (200 nm x 200 nm, V=1 V, I=0.5 nA) of a clean Ag(111) surface. (b) STM image (100 nm x 100 nm, V=1 V, I=0.5 nA) of the same surface as in (a), in which attention has been focused on the fuzzy aspect of the Ag(111) step edges. (c) Height profile along the black line in (a).

The first MoS_2 deposition process has been carried out by means of **10 laser pulses** and the obtained sample has been subjected to an annealing treatment at 650 K for 30 min. Subsequently, the same PLD process has been carried out in order to deposit 2D MoS_2 on top of a clean Ag(111) surface and a different thermal treatment has been performed by keeping the sample at approximately 730 K – i.e. the same annealing temperature employed in the case of MoS_2 nanostructures deposited onto an Au(111) substrate – for 30 min. First, the structure and morphology of the MoS_2/Ag(111) system obtained after the 650 K annealing will be discussed and, then, attention will be focused on the structural and morphological modification of the sample resulting from the 730 K thermal treatment.

The morphology of the MoS_2/Ag(111) system subjected to the lower temperature annealing treatment can be observed in the STM image of figure 3.14(a). Small MoS_2 islands are formed on top of the silver substrate that, after the PLD process, features the presence of a larger number of steps. The majority of these MoS_2 structures are characterized by an almost hexagonal shape (see, for instance, the islands indicated by the

black arrows in figure 3.14(a)), even though some structures featuring a polygonal shape can be also found. The higher magnification STM image in figure 3.14(b) and the line profile of figure 3.14(c) clearly show that these MoS_2 crystallites feature a rather high apparent height (of the order of ~5 Å) and no moiré pattern.

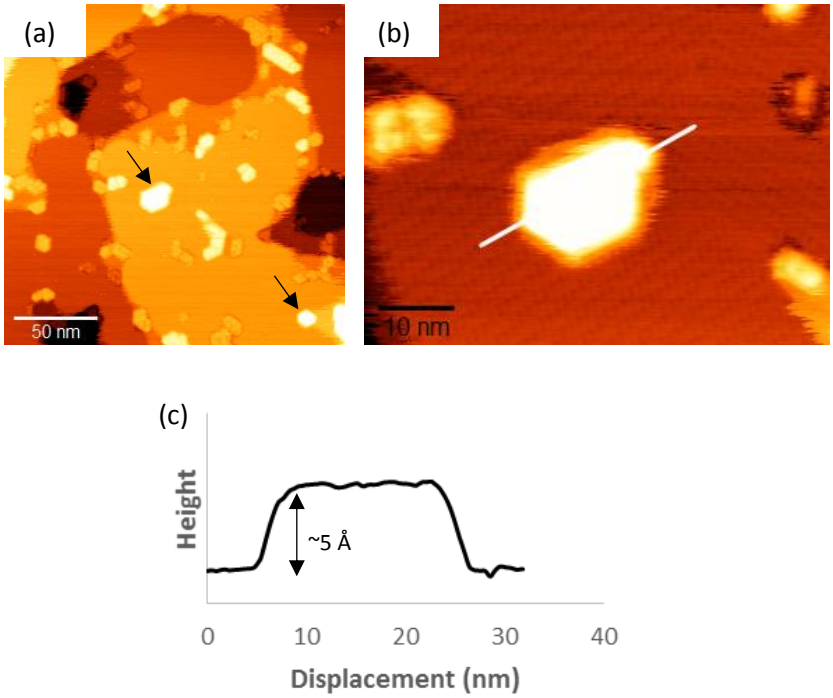

Figure 3.14: (a) STM image (200 nm x 200 nm, V=1.93 V, I=0.4 nA) of the MoS_2/Ag(111) system obtained by ablating a stoichiometric MoS_2 target with 10 laser pulses and performing an annealing treatment at 650 K for 30 min. The black arrows indicate the presence of MoS_2 crystallites featuring an almost hexagonal shape. (b) High magnification STM image (60 nm x 45 nm, V=1 V, I=0.35 nA) of a single MoS_2 island on top of Ag(111). (c) Height profile along the white line in (b).

It can be interesting to consider also the effect that the PLD process may have on the structure and properties of the silver surface used as a substrate. Indeed, the Ag(111) surface shows an ordered pattern that is different from that of clean Ag and, in particular, it seems to be covered by a peculiar phase, which can be observed in the high resolution STM images of figure 3.15.

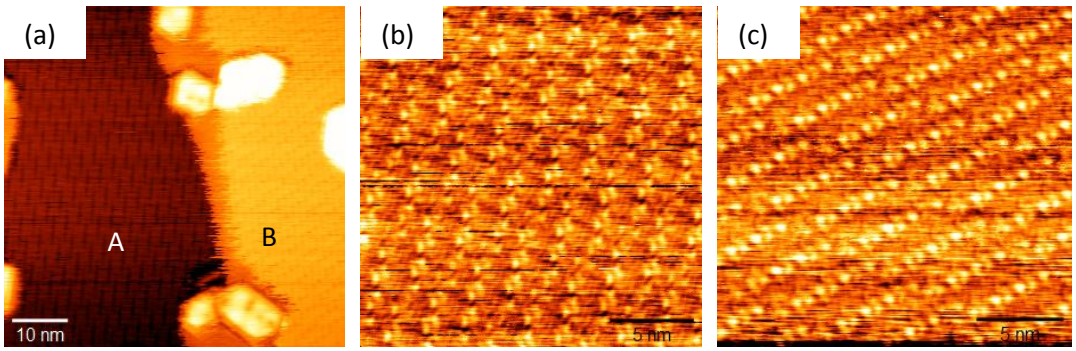

Figure 3.15: (a) STM image (60 nm x 60 nm, V=1 V, I=0.35 nA) of the MoS_2/Ag(111) system obtained by means of 10 laser pulses and annealed at 650 K for 30 min. (b) Higher resolution STM image (20 nm x 20 nm, V=1 V, I=0.3 nA) of the region marked as "A" in (a). (c) Higher resolution STM image (20 nm x 20 nm, V=0.8 V, I=1 nA) of the region labelled as "B" in (a).

Indeed, previous literature works (such as [57]) report theoretical and experimental studies according to which molecular sulphur can induce the formation of different surface reconstructions of Ag(111) and of several surface phases. For instance, this phase may probably consist in Ag_2S, a compound that has been already observed by other researchers during the growth of MoS_2 on top of silver [29] and that is formed due

to the strong chemical interaction between the Ag atoms of the substrate and the S atoms ejected from the ablated MoS_2 target. The formation of this phase might be helpful for the nucleation and growth of MoS_2 on top of the metallic substrate (as reported by Loh *et al.* in [29]) but its presence disturbs the STM measurements, thus making difficult the structural and morphological characterization of the produced sample. Indeed, some of the observed MoS_2 crystallites are partially embedded in this surface phase (see, for instance, the STM image in figure 3.16(a)), which is characterized by an apparent thickness of approximately 1.5 Å with respect to the underlying Ag surface (see the line profile in figure 3.16(c)). These MoS_2 structures feature an apparent height of ~3 Å and they seem to be characterized by a quite ordered moiré pattern, an aspect that can be appreciated by considering the STM image of figure 3.16(b).
Hence, it is possible to conclude that the pulsed laser deposition of MoS_2 by means of 10 ablating pulses and the subsequent annealing at approximately 650 K result in the formation of mainly hexagonal crystallites that can grow either on top of or partially embedded in the Ag – S surface phase.

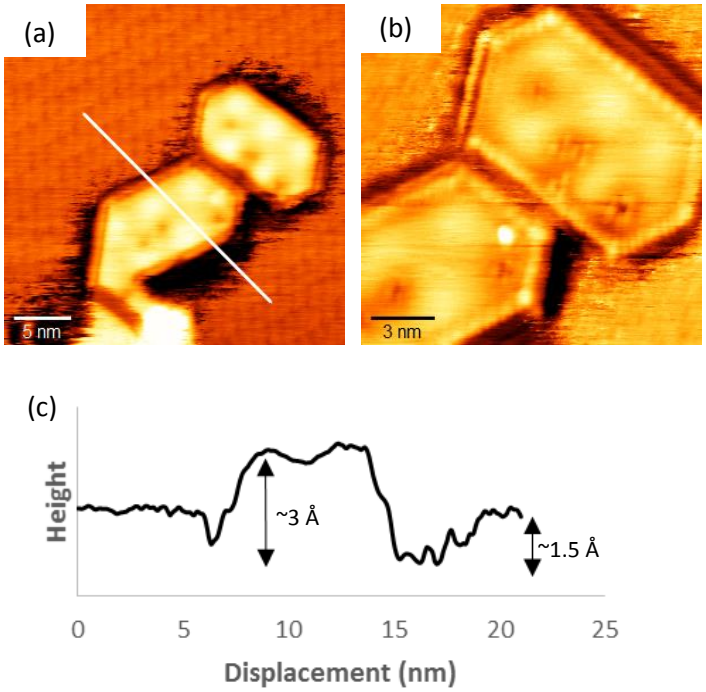

Figure 3.16: (a) STM image (29.2 nm x 29.2 nm, V=1.5 V, I=0.35 nA) of two hexagonal MoS_2 islands forming an in-plane junction on top of the Ag(111) surface. (b) Atomic-resolution STM image (15.7 nm x 15.7 nm, V=-0.35 V, I=0.9 nA) of the same structure investigated in (a). (c) Height profile along the white line in (a).

On the contrary, the morphology of the MoS_2/Ag(111) system obtained by annealing at higher temperature – i.e. around 730 K – is much more similar to the structural and morphological characteristics observed by Tumino *et al.* [44] in the case of the MoS_2/Au(111) system. Indeed, small and ordered MoS_2 islands are formed on top of the underlying silver substrate (figure 3.17(a)) and they all feature a regular shape and a surface moiré pattern due to the lattice mismatch between the underlying Ag(111) surface and the MoS_2 overlayer (as can be clearly seen in the STM image of figure 3.17(b)). In addition, they are all characterized by an apparent height (measured by means of STM) of ~2 Å – i.e. the same value of thickness found in the case of MoS_2 single-layer islands on top of Au(111) -, as can be evaluated from the line profile shown in figure 3.17(c).
High-magnification STM images have been acquired (figure 3.18(a)) and, in some cases, also atomic resolution has been achieved (see, for instance, the STM image in figure 3.18(b)). These high-quality STM images can be exploited in order to deeply investigate both the atomic structure of MoS_2 monolayer islands grown on top of Ag(111) and their characteristic moiré pattern, in order to compare these experimental findings with those of the MoS_2/Au(111) system. Indeed, it is possible to apply a 2D Fast Fourier Transform

(FFT) and to measure both the MoS_2 and the moiré reciprocal lattice vectors, from which the MoS_2 direct lattice vector and the moiré periodicity can be derived.

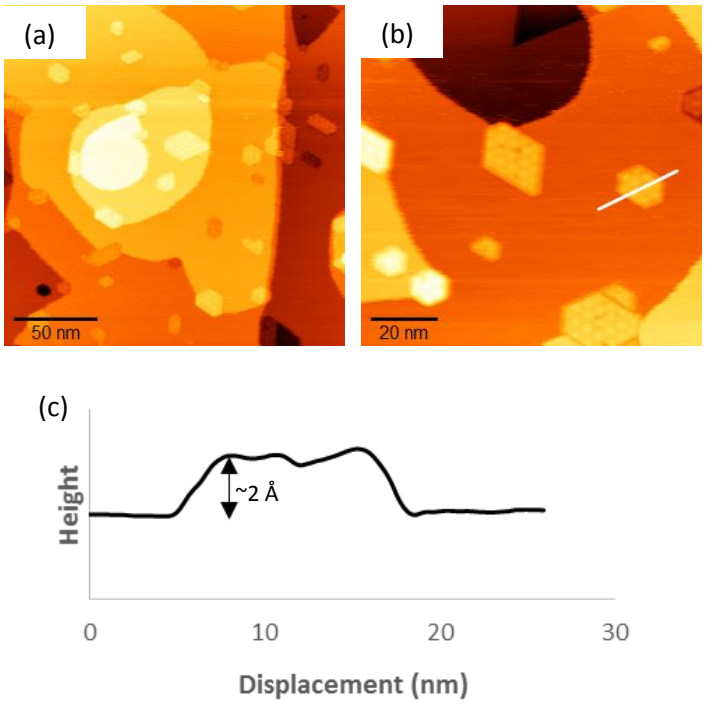

Figure 3.17: (a) Large-scale STM image (200 nm x 200 nm, V=1.3 V, I=0.3 nA) of the MoS_2/Ag(111) system fabricated by means of 10 ablating laser pulses and subjected to an annealing treatment lasting 30 min and carried out by keeping the sample at 730 K. (b) STM image (100 nm x 100 nm, V=0.8 V, I=0.3 nA) of the same sample as in (a). (c) Height profile along the white line in (b).

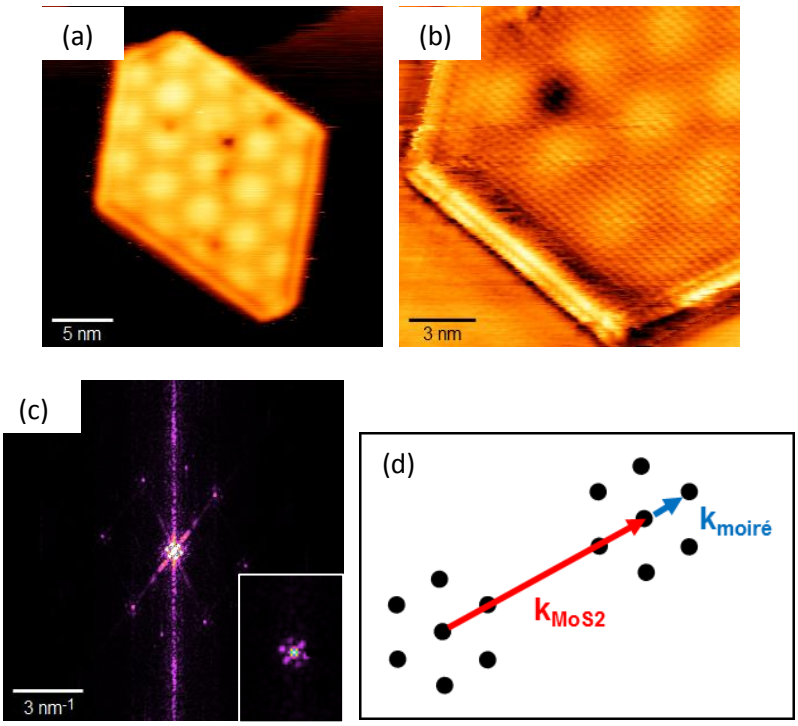

Figure 3.18: (a) High resolution STM image (27.3 nm x 27.3 nm; V=0.7 V, I=0.3 nA) of a MoS_2 island on top of Ag(111). (b) Atomic-resolution STM image (15 nm x 15 m, V=0.3 V, I=0.5 nA) of another MoS_2 island onto Ag(111). (c) 2D Fast Fourier Transform (FFT) of the STM image in (b), showing the spots of the MoS_2 hexagon, each surrounded by the moiré lattice spots. The inset shows more clearly the MoS_2 lattice spot surrounded by the spots of the moiré superstructure. (d) Schematic representation of the spots arrangement (not in scale): $\mathbf{k}_{MoS2}$ and $\mathbf{k}_{moirè}$ are the reciprocal lattice vectors of the MoS_2 and moiré lattices, respectively.

More in detail, the Fourier transform has been applied to the atomic-resolution STM image in figure 3.18(b) and the obtained result is shown in figure 3.18(c) and schematically represented in figure 3.18(d). The bright spots at the corners of the large hexagon represent the spots of the MoS_2 hexagonal lattice and, hence, the distance (in the reciprocal space) between each of these spots and the spot at the centre of the image is the MoS_2 reciprocal lattice vector – i.e. in the order of ~3 nm^{-1}. Then, by making an average among the distances between the central spot and all the six spots forming the large hexagon and by calculating the reciprocal of the obtained number, it is possible to estimate a modulus of the direct lattice vector of approximately 0.332 nm for the MoS_2 lattice – i.e. a value compatible with the atomic periodicity measured in the case of MoS_2 deposited onto an Au(111) substrate [44]. On the contrary, the periodicity of the moiré pattern can be extrapolated by considering the distance (in the reciprocal space) between each spot of the large hexagon and the six and less bright spots surrounding it (see the inset in figure 3.18(c)), which is approximately 0.3 nm^{-1}. Again, by averaging all the distances and by calculating the reciprocal of the resulting number, the periodicity of the moiré pattern can be derived, resulting equal to ~3.2 nm and, hence, similar with the value observed in the MoS_2/Au(111) system – i.e. 3.15 nm [44]. However, it is worth mentioning that in the case of MoS_2 on top of Au(111) a rotation angle θ=5.2° is present between the superstructure spots and the lines of the MoS_2 lattice [30], while in the case of the MoS_2/Ag(111) system the moiré spots and the spots related to the hexagonal MoS_2 lattice seems to be aligned, in the sense that there seems to be no misalignment between the MoS_2 lattice and the moiré pattern. As a consequence, also the MoS_2 lattice and the lattice of the Ag(111) surface are aligned.
Also, we observed localized defects on top of the otherwise regular MoS_2 surface. MoS_2 surface defects have been already observed and investigated in [44] by Tumino and co-workers, who have made a distinction between point defects and line defects, having not only a different morphology but also a different origin.

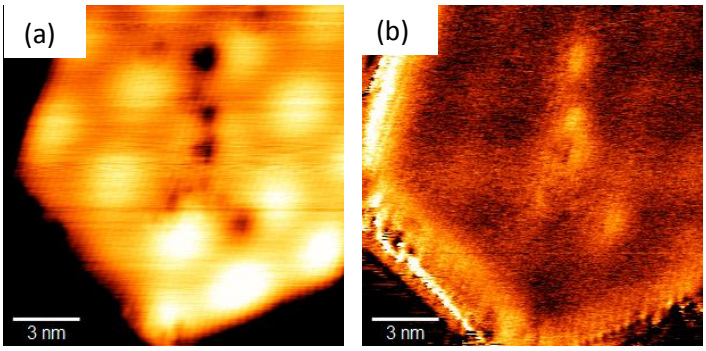

Figure 3.19: (a) High-magnification STM image (15 nm x 15 nm, V=0.6 V, I=0.5 nA) of a MoS_2 island growing on top of an Ag(111) surface and featuring the presence of point defects. (b) Corresponding differential conductivity map in which the defects appear brighter than the rest of the island surface.

Point defects can be observed in the STM image and in the corresponding dI/dV map shown in figure 3.19. As can be clearly seen in the topographic image of figure 3.19(a), this kind of defects appear as localized black spots on the otherwise ordered MoS_2 surface. However, it is worth remembering that the acquired STM images do not exactly represent the real topography of the system under investigation as also electronic effects can play a relevant role. Indeed, these dark spots on the MoS_2 surface can represent atomic vacancies but they can also be associated to the presence of an atom or a phase characterized by a lower tunneling conductivity with respect to the surrounding environment, hence giving a less bright contrast in the STM image. The differential conductivity map in figure 3.19(b) can be a bit more helpful in the study of the nature of the observed defects. Indeed, it is clearly visible that these defects are characterized by a very bright contrast in the dI/dV map with respect to the rest of the MoS_2 island surface and, since both the STM image and the corresponding differential conductivity map have been acquired by applying a positive bias of 0.6 V between the tip and the sample, they are related to the presence of empty surface electronic states. Nevertheless, a further and deeper investigation of these point defects is necessary in order to directly

compare this morphological aspect of the MoS_2/Ag(111) system with the very detailed study of this type of defects, which has been already carried out for 2D MoS_2 on top of Au(111) (see [44] for more details).
On the contrary, line defects are typically present in large MoS_2 islands, which have been formed thanks to the meeting and coalescence of two smaller crystallites (figure 3.20(a)). This kind of defects has been already observed during the investigation of the MoS_2/Au(111) system by Tumino *et al.* [44], who have also explained their origin. MoS_2 islands grown on top of Au(111) (and, hence, even onto an Ag(111) substrate) can feature two different type of edges – i.e. the so-called S-edge and Mo-edge. When two smaller MoS_2 structures coalesce in order to generate a larger island, two different situations can take place. Indeed, if two edges of different type join the generated island is characterized by an ordered surface and no line defect is formed, while if the two merging islands feature the same edge type a line defect is created (see [44] for more details).

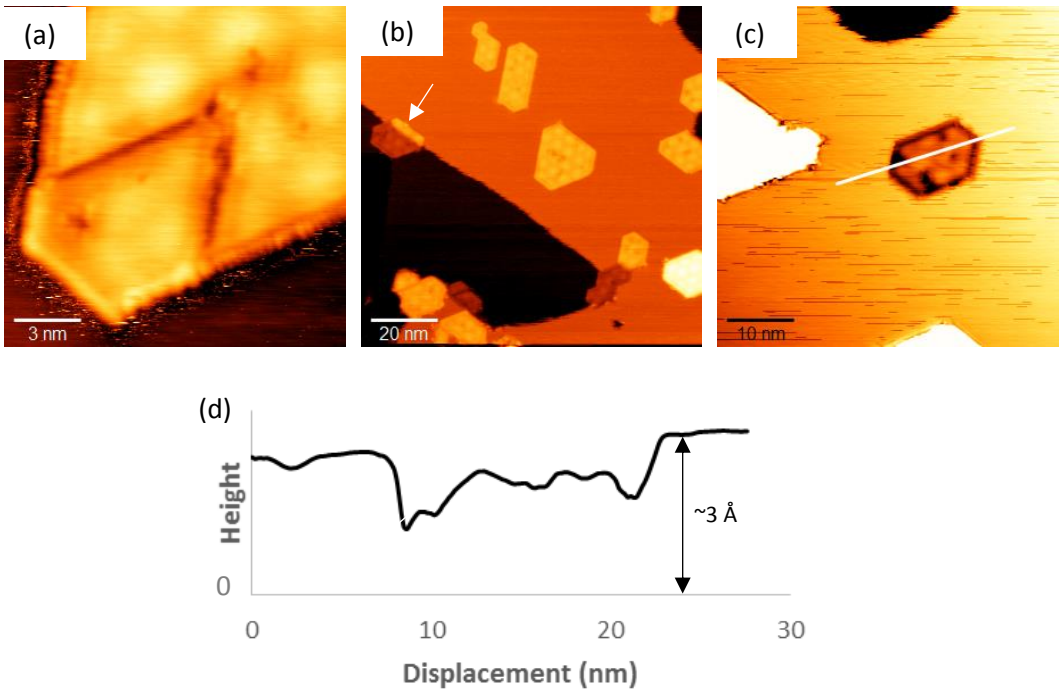

Figure 3.20: (a) High resolution STM image (15 nm x 15 nm, V=0.3 V, I=0.5 nA) of a MoS_2 island featuring the presence of line defects formed due to the joining of two islands characterized by the same edge type. (b) STM image (100 nm x 100 nm, V=1.93 V, I=0.3 nA) of the sample obtained using 10 ablating pulses and subjected to a thermal treatment at approximately 730 K for 30 min. The white arrow marks the presence of a MoS_2 island growing partially on one silver terrace and partially on the lower one. (c) STM image (50 nm x 50 nm, V=0.6 V, I=0.5 nA) of a partially embedded MoS_2 island. (d) Height profile along the white line in (c).

Finally, two other relevant characteristics can be observed in the STM images in figure 3.20(b)-(c). The first feature is related to the presence of MoS_2 islands growing partially on one silver terrace and partially on the lower one (see, for instance, the MoS_2 crystallite marked by the white arrow in figure 3.20(b)) and it may be due to the very good interaction between the overlayer and the underlying metallic substrate that allows the coherent growth of the MoS_2 monolayer even on top of different silver terraces. The second morphological characteristic is associated to the presence of the so-called partially embedded MoS_2 islands, considering that "partially embedded" means that such islands lie on top of a one-step lower Ag patch, with respect to the surrounding Ag terrace. Indeed, the line profile in figure 3.20(d) shows that the MoS_2 surface, corrugated due to the presence of the moiré pattern, is approximately at the same level of the surrounding Ag terrace. The growth of partially embedded single-layer MoS_2 islands has been observed also in the case of the MoS_2/Au(111) system [44] and causes the formation of in-plane Ag/MoS_2 interfaces of peculiar morphology, which will require a further and deeper investigation.

Attention will now be focused on the STM characterization of the sample obtained by ablating the MoS_2 target with **30 laser pulses** and then annealing the system for 30 min at ~730 K. The overall morphology of the produced sample is shown in the large-scale STM image of figure 3.21(a). As can be clearly evaluated by comparing figure 3.21(a) and figure 3.17(a), the average size of the MoS_2 islands on top of the Ag substrate has remarkably increased together with the coverage, even though an estimation of the percentage of the silver surface covered by 2D MoS_2 can not be performed due to the presence of several Ag steps in the acquired STM images. Nonetheless, it is possible to observe that increasing the number of laser pulses leads to the formation of more extended MoS_2 single-layer islands that tend to coalesce and to generate an almost continuous MoS_2 monolayer. Indeed, line defects are clearly visible on the MoS_2 surface (see, for instance, the white arrows in figure 3.21(b)) and this is a hint of the fact that smaller MoS_2 crystallites have met and joined in order to form larger islands, as discussed previously.

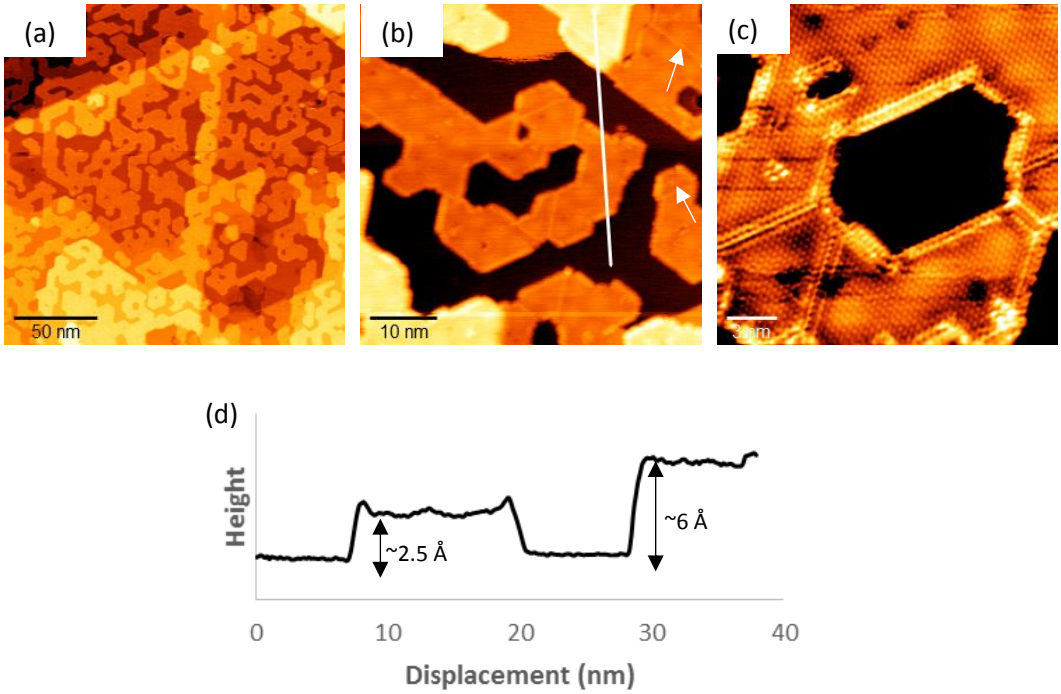

Figure 3.21: (a) Large-scale STM image (200 nm x 200 nm, V=-1.75 V, I=0.4 nA) of the MoS_2/Ag(111) sample obtained by performing a 30-pulses PLD process and an annealing treatment at a temperature of ~730 K for 30 min. (b) Higher resolution STM image (50 nm x 50 nm, V=-1.2 V, I=0.4 nA) of the same sample as in (a), in which it is clearly visible that an almost continuous MoS_2 monolayer is formed due to the coalescence of smaller islands. Indeed, the white arrows mark the presence of line defects generated by the meeting and joining of two MoS_2 islands featuring the same edge type. (c) Atomic resolution STM image (20 nm x 20 nm, V=-0.7 V, I=0.35 nA) in which the atoms forming the MoS_2 monolayer on top of Ag(111) can be clearly observed. (d) Height profile along the white line in (b).

As the structure and morphology of the single MoS_2 islands is concerned, it is possible to note that they feature a polygonal but irregular shape resulting from the coalescence of smaller crystallites and their apparent height can be determined. As can be extrapolated from the STM image in figure 3.21(b) and from the corresponding line profile in figure 3.21(d), two different types of MoS_2 structures can be recognized thanks to the fact that they show a very different colour contrast. The darker regions, which are much more abundant, feature an apparent height of approximately 2.5 Å – i.e. more or less compatible with the thickness of a MoS_2 monolayer. On the contrary, the brighter regions are quite rare, feature an apparent height of the order of 6 Å and can be thus associated to bilayer MoS_2. In reality, the thickness of a bilayer island should be approximately equal to 8 Å if the interlayer spacing between two adjacent MoS_2 layers is assumed to be in the order of 6 Å as in the bulk, but this small height difference can be due to electronic effects playing a relevant role in the STM measurements.

Finally, we observe that the obtainment of atomic-resolution STM images (figure 3.21(c)) suggests the very high crystalline quality of the deposited material and the rather high stability of the tip-sample interaction and, hence, of the STM measurements.

In addition, in order to further increase the coverage and to obtain a continuous MoS_2 film covering completely (or almost completely) the underlying silver substrate, a deposition was performed by means of **50 ablating laser pulses**, followed by the usual 30 min annealing treatment at ~730 K. The morphology of the obtained system is shown in the STM image of figure 3.22, where it is possible to observe that the Ag(111) surface is completely covered by the deposited material. However, it is worth mentioning that STM measurements can not be easily performed to investigate such a sample because the substrate surface appears to be characterized by the presence of a large number of steps and because the stability of the tip-sample interaction decreases as the amount of deposited material increases.

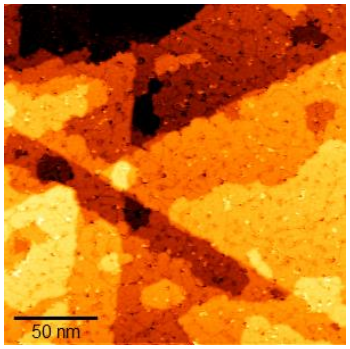

Figure 3.22: STM image (200 nm x 200 nm, V=1.5 V, I=0.5 nA) of the MoS_2/Ag(111) system produced by employing 50 ablating laser pulses in the PLD process and performing a thermal treatment at ~730 K for 30 min.

To summarize, PLD has been employed in order to deposit two-dimensional MoS_2 structures on top of Ag(111) with an increasingly high coverage and, subsequently, the structure and morphology of the obtained samples have been characterized by means of a scanning tunneling microscope and compared to the structural and morphological characteristics of the similar MoS_2/Au(111) system [44]. This comparison has been carried out in order to evaluate whether the presence of a different substrate may influence the structure and morphology of the deposited material. Indeed, it is possible to conclude that the different nature of the substrate is not so relevant in the determination of the structural and morphological features of the system, except for what concerns the moiré pattern. It is now necessary to consider the influence of the substrate on the electronic, optical and vibrational properties of the deposited material (sections 3.2.2 and 3.2.3).

3.2.2 Electronic properties of MoS_2 nanostructures on Ag(111)

The investigation of the electronic properties of two-dimensional MoS_2 nanostructures on Ag(111) has been performed by means of scanning tunneling spectroscopy. In particular, the STS measurements have been carried out by keeping the tip-sample distance constant while linearly changing the bias voltage in a range between 2 V and -2 V, in such a way to investigate a range of few eV around the Fermi level.

Before starting the discussion about the STS spectra acquired on single-layer MoS_2 grown onto Ag(111), a brief description of the I(V) and dI/dV curves characteristic of the Ag(111) substrate may be useful. For this reason, the STS spectra acquired on top of the Ag(111) surface have been reported in figure 3.23.

The most relevant peculiarities in the STS spectra of the Ag(111) surface can be appreciated by considering the voltage region around 0 – i.e. around the Fermi level. Indeed, both in the I(V) curve and, hence, also in the corresponding dI/dV spectrum, an important change in the trend of the curves can be clearly seen. Indeed, in the I(V) spectrum (figure 3.23(a)), a strong modification in the slope of the curve occurs around the Fermi level, with the slope being lower for negative voltages and larger for positive applied biases.

Accordingly, in the corresponding differential conductivity curve plotted in figure 3.23(b), a step is clearly evident in the shape of the curve, thus suggesting a sudden increase in the tunneling conductivity when a positive bias voltage is applied between the tip and the Ag(111) surface under investigation. The origin of this step in the dI/dV curve is related to the presence of a Shockley surface state – i.e. similar to the characteristic Shockley state present at V=-0.5 V in the case of the Au(111) surface – around zero and, in particular, at approximately -67 meV [58, 59].

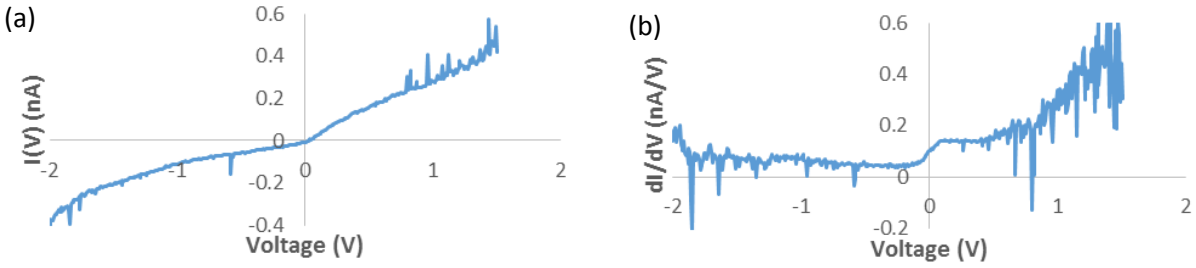

Figure 3.23: (a) I(V) spectrum of the Ag(111) substrate. Acquisition set-point: V=2 V, I=0.5 nA. (b) Corresponding dI/dV spectrum, which has been properly rescaled in order to adapt it to the numerical derivative of the related I(V) curve. Both the spectra have been acquired by scanning the voltage in a range between 1.5 V and -2 V.

As regards 2D MoS_2 nanostructures on Ag(111), the STS spectra are shown in figure 3.24 and they appear to be strongly different from the ones reported in the case of the clean metallic substrate. More in detail, while in the case of Ag(111) a non-zero value of the tunneling conductivity characterizes the whole investigated voltage range (figure 3.23(b)), in the case of 2D MoS_2 it is possible to recognize the presence of an energy gap – i.e. a region of the considered voltage range where the tunneling current and, hence, the tunneling conductivity are zero or almost equal to zero – (figure 3.24(b)). Indeed, by considering the differential conductivity curve in figure 3.24(b), an energy gap of the order of 2 eV can be estimated for the 2D MoS_2 nanostructures under investigation, thus confirming the semiconducting behaviour of molybdenum disulphide. Furthermore, from the analysis of the I(V) spectrum reported in figure 3.24(a), the approximate positions at which the VB and CB edges occur can be evaluated, resulting to be about -1.5 V and +0.5 V, respectively.

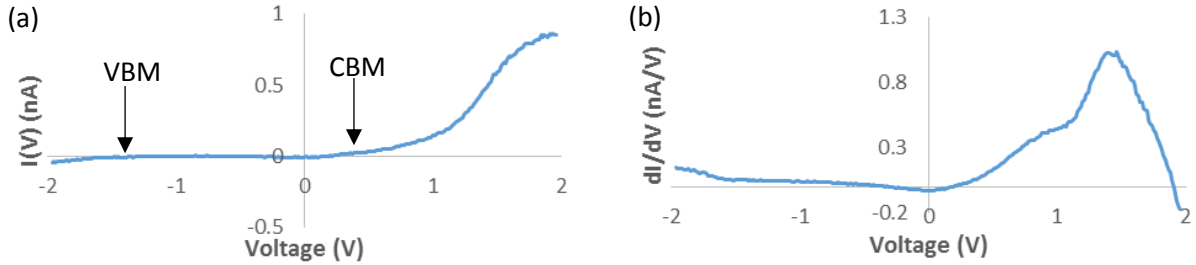

Figure 3.24. (a) I(V) spectrum of 2D MoS_2 deposited on top of an Ag(111) substrate. Acquisition set-point: V=2 V, I=0.5 nA. (b) Corresponding dI/dV spectrum, which has been properly rescaled in order to adapt it to the numerical derivative of the I(V) curve.

These experimental findings are equivalent to the STS results obtained by Tumino *et al.* [44] for the MoS_2/Au(111) system, thus suggesting that the nature of the overlayer/substrate interaction is very similar in the two cases and it affects in a similar way the electronic properties of the supported 2D material. Furthermore, other two aspects of the electronic behaviour of low-dimensional MoS_2 onto Ag(111) deserve to be mentioned, as they are present also in the MoS_2/Au(111) system [44]. The first feature is related to the fact that the MoS_2 tunneling conductivity is not exactly equal to zero in the gap region, while the second characteristic can be extrapolated by observing that the Fermi level is not right in the middle of the gap, but much closer to the CBM than to the VBM. The former aspect may be a hint of a slight metallization of the

deposited material, while the latter one indicates a n-type conductance behaviour of MoS_2 on top of Ag(111). Both these aspects are due to the interaction between the overlayer and the underlying silver substrate and to charge transfer phenomena occurring at the interface between the two materials.
In addition, a local study of the electronic properties of the fabricated nanostructures has been carried out by acquiring I(V) and dI/dV spectra in different regions of the MoS_2 islands under investigation. In particular, three different zones have been analysed: the island surface, the island edges and the grain boundaries, which may be formed due to the joining of two MoS_2 islands featuring the same edge type. The resulting STS spectra are shown in figure 3.25, together with a reference STM image.

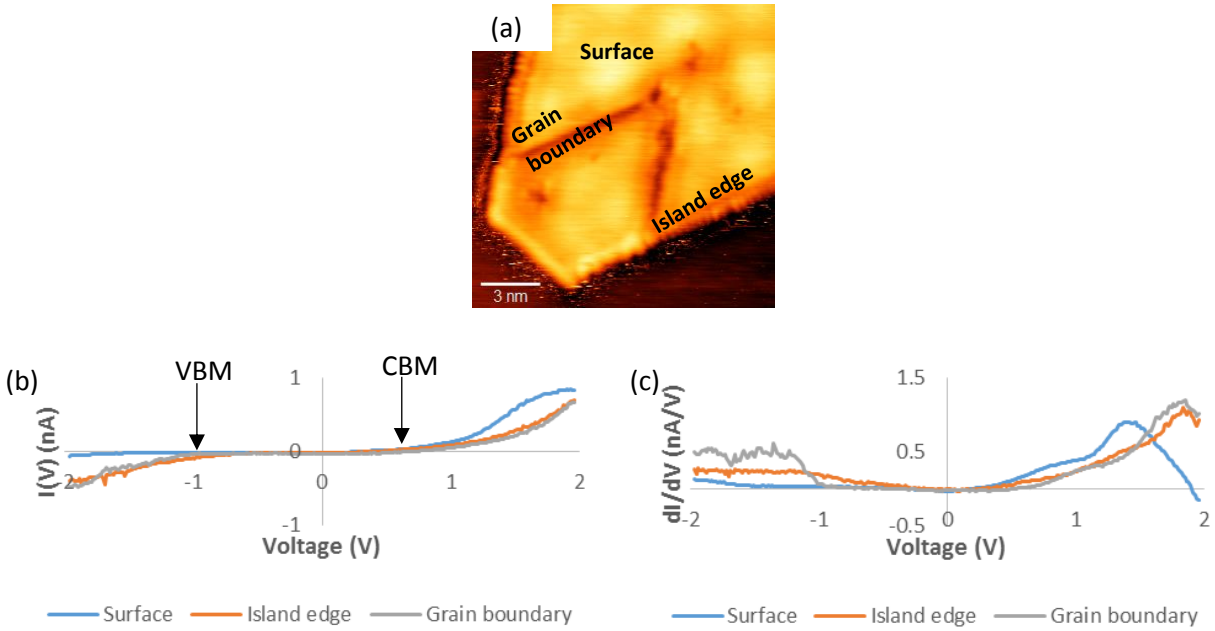

Figure 3.25: (a) Reference STM image (15 nm x 15 nm, V=0.3 V, I=0.5 nA) showing the three distinct zones of the produced MoS_2 nanostructures investigated by means of STS. (b) I(V) spectra resulting from STS measurements performed on the island surface, on the island edge and in correspondence of the island grain boundaries. Acquisition set-point: V=2 V, I=0.5 nA. (c) Corresponding differential conductivity (dI/dV) curves, which have been properly rescaled in order to adapt them to the numerical derivative of the related I(V) spectra.

By considering the I(V) spectra of the three investigated regions of the MoS_2 nanostructures (figure 3.25(b)), it is possible to note that the electronic properties of the material in correspondence of the island edges (orange curve) and of the grain boundaries (grey curve) are quite similar, despite being very different from those featured by the surface of the crystallites (blue curve). Indeed, it can be clearly seen that the VBM and the CBM occur in different positions in the case of the surface and in the case of the island edges/grain boundaries. When considering the island surface – i.e. a portion of the MoS_2 crystallite far from the edges and from grain boundaries -, the VBM and the CBM occur in correspondence of -1.5 V and +0.5 V, as previously discussed. On the contrary, in correspondence of island edges and grain boundaries, the VB maximum is at approximately -1 V and the CB minimum at +0.5 V (as indicated in figure 3.25(b)). Hence, an energy gap of ~2 eV and ~1.5 eV results for the surface and the boundary regions, respectively, as can be also evaluated from the dI/dV spectra in figure 3.25(c). Finally, the last relevant aspect can be appreciated by considering the slope of the differential conductivity curve in the positive voltage range. Indeed, the dI/dV spectrum related to the surface appears to be characterized by a larger slope at positive bias, thus suggesting that the surface tunneling conductivity increases faster than that found in correspondence of the island edges and of the grain boundaries.
It is possible to draw some conclusions. First, the electronic band gap is lower along the edges and the grain boundaries and larger in the middle of the MoS_2 islands, thus suggesting a reduction in the energy gap of the material due to the presence of edge or defect electronic states. Second, a non-zero tunneling conductivity

can be found in the gap region for all the three investigated zones of the overlayer and this may be a hint of a slight metallization of the material, which is related to the MoS_2/Ag(111) electronic interaction and to charge transfer phenomena that can take place at the interface. Third, the Fermi level is not in the middle of the gap but closer to the CB edge and this experimental finding may be again due to the interaction with the underlying Ag substrate, which causes a n-type behaviour of the material, not only on the MoS_2 island surface but even in correspondence of the boundary regions.

3.2.3 Auger electron spectroscopy, Raman spectroscopy and photoluminescence (PL) measurements

In order to further investigate the properties of two-dimensional MoS_2 deposited on top of Ag(111), AES, Raman spectroscopy and PL measurements have been employed as additional characterization tools able to provide complementary information that can integrate the experimental results achieved by means of STM and STS. Before discussing the obtained experimental findings, it is worth mentioning that all these characterization techniques have been applied to the MoS_2/Ag(111) samples produced by means of 30 and 50 ablating laser pulses because they all require a sufficiently large amount of material deposited onto the metallic substrate and, hence, an enough high coverage.

Auger electron spectroscopy has been employed in order to verify the chemical composition of the deposited material and to evaluate the presence of surface contaminants resulting from the air exposure of the MoS_2/Ag(111) samples for some hours. In particular, in the framework of this experimental activity, the presence of peaks in the Auger spectrum related to the MNN transition of Mo atoms and to the LMM transition of S atoms is relevant in order to check whether MoS_2 has been effectively deposited on top of Ag(111) by means of PLD, while Auger peaks revealing the presence of O and C – i.e. the most common contaminants deposited on top of a surface during air exposure – can be considered as hints of sample contamination.

First of all, AES measurements have been performed on MoS_2/Ag(111) samples produced by employing 30 and 50 laser pulses in order to qualitatively check the chemical composition of the deposited material. The recorded Auger spectra are shown in figure 3.26(a). As can be clearly seen, the two AES spectra are exactly equivalent and they are both characterized by the presence of only two peaks. The first peak appears in correspondence of an electron kinetic energy of approximately 140 eV and is due to the presence of S atoms in the first few layers of the investigated sample [56]. On the contrary, the second peak occurring around 350 eV is related to the presence of Mo atoms [56]. Hence, as only these two peaks are present in the Auger spectra of the two analysed MoS_2/Ag(111) systems, it is possible to conclude that only Mo and S atoms are present onto Ag(111), considering that only a qualitative analysis of the acquired spectra has been carried out and thus no precise information about the stoichiometry of the deposited material has been derived. Nonetheless, the absence of other peaks has confirmed the expected absence of contamination, being aware of the fact that the sensitivity of AES is high since it allows to detect the presence of elements with a concentration in the order of 0.1 – 1 % of a monolayer [55].

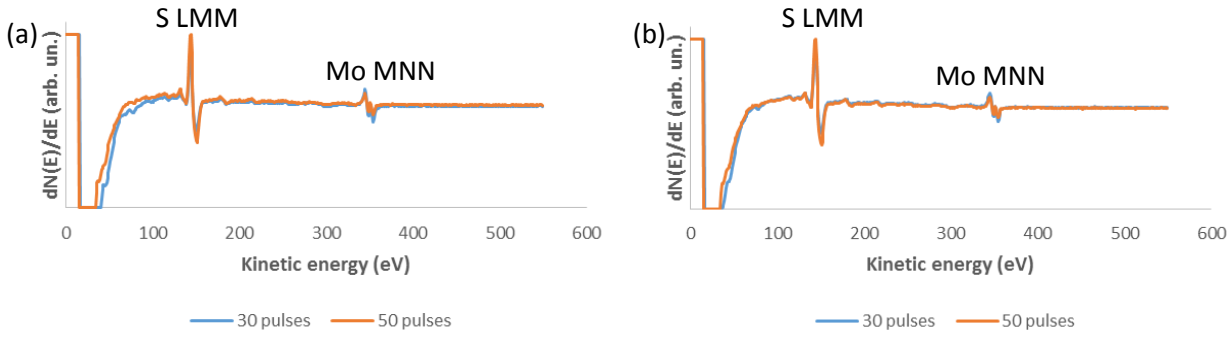

Figure 3.26: (a) AES spectra acquired on MoS_2/Ag(111) samples obtained by means of 30 laser pulses and 50 laser pulses. (b) AES spectra obtained on the same samples as in (a) after some hours air exposure.

Subsequently, the samples have been taken out of the UHV system in order to perform Raman and PL measurements and after some hours, during which the samples have been exposed to air, they have been placed back under ultra-high vacuum conditions and AES measurements have been carried out in order to evaluate the presence of surface contaminants. The resulting Auger spectra are reported in figure 3.26(b).
No appreciable modification of the Auger spectra of the two investigated samples can be observed by comparing figures 3.26(a) and 3.26(b), thus suggesting that air exposure (even for some hours) does not affect the chemical composition of the deposited material, at least not significantly. Indeed, the Auger spectra of the MoS_2/Ag(111) systems are exactly the same before and after air exposure and, moreover, it is possible to note that no peaks associated to the presence of carbon (ususally occurring at approximately 270 eV) and oxygen (typically arising at 500 eV) are present [56], thus suggesting that no contamination and oxidation of the samples have occurred.
In conclusion, AES measurements have confirmed the chemical compsition of the material deposited by means of PLD on top of an Ag(111) substrate and, moreover, they have demonstrated the chemical stability of 2D MoS_2 under ambient conditions, even for a rather long time – i.e. some hours. This last aspect is particularly relevant because it makes possible to employ *ex situ* characterization techniques without risking to contaminate the material of interest.

Raman spectroscopy has been employed in order to study the vibrational properties of 2D MoS_2 supported by Ag(111), to derive information about the structure of the deposited material (such as, for instance, the number of layers) and, finally, to investigate the nature of the overlayer-substrate interaction.

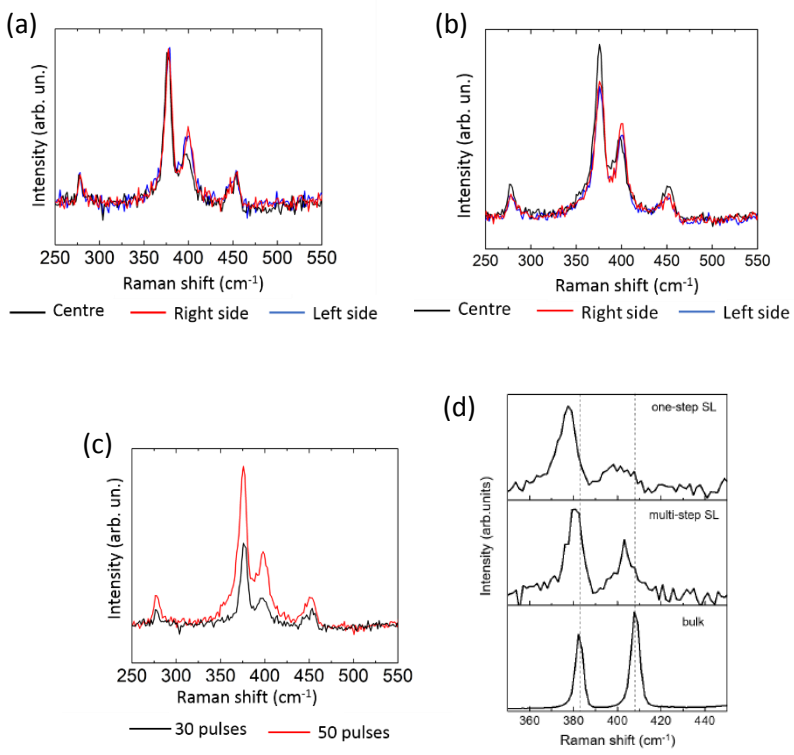

Figure 3.27: (a) Raman spectra acquired on the MoS_2/Ag(111) sample fabricated by means of 30 laser pulses. The three curves are related to different regions of the investigated system: centre (black), right side (red) and left side (blue). (b) Raman spectra acquired on the MoS_2/Ag(111) sample produced by means of 50 ablating pulses. The three curves are again related to different zones of the analysed sample: centre (black), right side (red) and left side (blue). (c) Raman spectra acquired on the 30-pulses sample (black curve) and on the 50-pulses sample (red curve). (d) Raman spectra of bulk MoS_2 (lower panel) and single-layer MoS_2 deposited on top of Au(111) by means of a multi-step deposition process (central panel) and by means of a single-step PLD process (upper panel). Reproduced from [44], for comparison reasons.

The Raman spectra acquired on the MoS_2/Ag(111) systems produced by means of 30 laser pulses (lower coverage) and 50 ablating pulses (higher coverage) are reported in figure 3.27(a) and 3.27(b), respectively, considering that the small peak at ~285 cm^{-1} is associated to the E_{1g} bulk mode (termed as E'' in the case of a monolayer) and the one at approximately 450 cm^{-1} is a second-order Raman peak and they will not be considered in the following discussion. For comparison, Raman spectra of single-layer MoS_2 films on top of an Au(111) substrate [44] are shown in figure 3.27(d), together with the spectrum acquired on a bulk crystalline MoS_2 sample.

The Raman spectrum of bulk MoS_2 (figure 3.27(d), lower panel) features the presence of two peaks at 382.6 cm^{-1} and 408.2 cm^{-1}, which are associated to the in-plane E^1_{2g} and the out-of-plane A_{1g} vibrational modes, respectively [28]. Both peaks are sharp, with a width smaller than 4 cm^{-1}, as expected for crystals. In the Raman spectra of MoS_2 deposited onto Ag(111) (figure 3.27(a)-(b)), however, both these two vibrational features appear to be significantly modified as both peaks shift to lower frequencies with respect to bulk MoS_2 and, especially for the A_{1g} mode, strong broadening and intensity attenuation can be observed, resulting in an inversion of the intensity ratio between them, as can be seen considering the data in table 1 and resulting from a numerical analysis based on Lorentzian fitting curves. The same experimental findings have been also reported by Tumino and co-workers for what concerns the MoS_2/Au(111) system [44] (figure 3.27(d)) and, in particular, the E^1_{2g} and A_{1g} peak positions result to be very similar when considering 2D MoS_2 deposited onto Ag(111) and Au(111) (see data reported in table 1).

The observed modification of the Raman spectrum when considering Ag(111)-supported and Au(111)-supported MoS_2 instead of the bulk crystalline material can be due to different mechanisms related to the interaction between the overlayer and the underlying metallic substrate, as discussed by Tumino *et al*. in [44]. Indeed, at least two distinct phenomena can modify the MoS_2 vibrational modes: the out-of-plane strain, which weakens the intralayer bond strength [36, 60, 61], and the n-type doping of the deposited material [62], an aspect whose presence has been also confirmed by the performed STS measurements. These two effects affect the E^1_{2g} and the A_{1g} vibrational modes in a different way. Indeed, the in-plane E^1_{2g} vibration is strongly influenced by strain effects [63, 64] induced, for instance, by the moirè superlattice that can influence the vibrational properties of the system and cause a softening of the peak, while it is less sensitive to doping [62]. On the contrary, the A_{1g} vibrational mode is significantly affected by the doping of the material, which is very effective in softening and broadening the A_{1g} peak due to its high sensitivity to electron-phonon coupling [62].

Table 1: Data extracted from the Raman spectra shown in figure 3.27(a)-(b) and from the Raman spectra reported by Tumino and co-workers in [44]. The table reports the position and width (both in cm^{-1}) of the E^1_{2g} and A_{1g} modes of MoS_2. The frequency difference between the two modes and the intensity ratio (A_{1g}/E^1_{2g}) are also reported.

	E^1_{2g}		A_{1g}			
	position	width	position	width	$P(A_{1g}) - P(E^1_{2g})$	$A(A_{1g})/A(E^1_{2g})$
30-pulses	377.1	9.2	399.3	11.9	22.2	0.503
50-pulses	375.6	12.8	399.9	11.7	24.3	0.511
MoS_2/Au(111)	377.1	9.1	400.9	13.4	23.8	0.45
Bulk	382.6	3.6	408.2	3.9	25.6	1.456

An important parameter that can be easily derived from the acquired Raman data is the frequency difference between the A_{1g} and the E^1_{2g} modes. In the literature, this parameter is usually used in order to assess the number of layers forming the two-dimensional MoS_2 structures under investigation since it decreases from approximately 25 cm^{-1} for bulk MoS_2 to about 18 cm^{-1} for single-layer flakes [28]. This procedure can be applied in the case of exfoliated [65] or CVD-grown [36] single-layer MoS_2 – i.e. characterized by a very weak interaction with the underlying substrate. On the contrary, the MoS_2/Ag(111) systems under investigation feature a higher interaction between the overlayer and the substrate and, in particular, the simultaneous presence of two interface effects – i.e. n-type doping and strain -, which influence the position of the two

peaks in different ways, thus making impossible to directly relate the frequency difference with the thickness of the deposited material [44]. Indeed, even though the performed STM measurements have confirmed the formation of monolayer MoS_2, the values found for the investigated MoS_2/Ag(111) systems are compatible with the value reported by Tumino *et al*. [44] for the monolayer MoS_2/Au(111) system and larger (around 23 cm^{-1}) than the one reported in previous literature works for single-layer MoS_2 – i.e. 18 cm^{-1}. On the contrary, it is worth mentioning that the value of the frequency difference between the two vibrational modes related to bulk MoS_2 – i.e. 25.6 cm^{-1} – is compatible with the one reported in the literature [28].
Furthermore, it may be useful to make a comparison between the Raman spectrum obtained during the investigation of the 30- and 50-pulses MoS_2/Ag(111) systems (black and red curves respectively in figure 3.27(c)). The intensity of both the E^1_{2g} and the A_{1g} peaks are larger in the 50-pulses case due to the fact that a larger amount of material deposited on top of the Ag substrate results in a stronger Raman signal. Nonetheless, it is worth mentioning that the peak position and width and the intensity ratio between the two peaks is very similar for the two investigated systems (as can be evaluated from the data reported in table 1). Thus, this experimental finding, together with the STM measurements, confirms the fact that both samples consist in monolayer MoS_2 and the only difference between them is the coverage.
Finally, Raman spectra have been acquired in different positions of the analysed samples: they have very similar peak position and width and only minor intensity differences can be observed between the centre and the edges of the sample surface (figure 3.27(a)-(b)). This finding is a very relevant experimental result that confirms one of the most important advantages of using PLD as a deposition process – i.e. the uniform distribution of the ablated material on top of the substrate -, consdering that the uniformity of the growth process allows the production of a 2D material with homogeneous morphology, thickness and, hence, electronic and optical properties on an area of the order of 1 cm^2.

Using the same experimental apparatus employed in order to perform Raman spectroscopy, **photoluminescence (PL) measurements** have been carried out in order to investigate the effect of the Ag substrate on the electronic and optical properties of 2D MoS_2. Indeed, the fact that the considered 2D MoS_2 structures are neither free-standing nor only weakly interacting with an insulating substrate but strongly interacting with a metal surface can affect a lot the properties of the overlayer itself. This aspect has been already demonstrated for the MoS_2/Au(111) system by Tumino and co-workers [44] and may be also present in 2D MoS_2 deposited on top of Ag(111) due to the very high similarity between these two systems.
More in detail, Mak *et al.* [6] have reported that exfoliated single-layer MoS_2 is a direct band gap semiconductor showing intense PL at 1.9 eV. However, by exciting the MoS_2/Ag(111) samples obtained by means of 30 and 50 ablating laser pulses during the PLD process with a 514.5 nm wavelength – i.e. corresponding to an energy of 2.41 eV – the obtained PL spectrum is the one shown in figure 3.28.

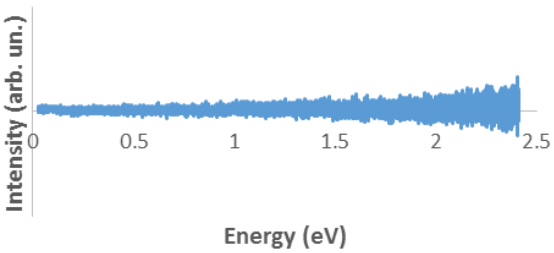

Figure 3.28: PL spectrum of two-dimensional MoS_2 on Ag(111).

The acquired PL spectrum does not show the typical emission peak of monolayer MoS_2 at approximately 1.8 – 1.9 eV, thus suggesting the total quenching of MoS_2 photoluminescence that likely occurs due to charge transfer phenomena occurring upon excitation, involving the overlayer and the underlying silver substrate and preventing the excitonic recombination in 2D MoS_2. Tumino *et al*. [44] provided this explanation for the

same phenomenon occurring in the MoS_2/Au(111) system produced by PLD. In reality, it is worth mentioning that the same effect has been also observed in CVD-grown single-layer MoS_2 on top of a gold substrate [66] but not in the case of exfoliated monolayer MoS_2 weakly interacting with gold [65].
Therefore, it is possible to conclude that the PL quenching has to be related to the nature of the metal-semiconductor junction forming at the interface between the overlayer and the underlying substrate and depending on the synthesis process of the deposited material. Nonetheless, further investigation of this effect will be necessary in order to clearly understand the role played by the growth process in determining the electronic and optical properties of the MoS_2/metal heterostructures.

3.3 Pulsed laser deposition and STM characterization of silicon on Ag(111) and Au(111)

This section is devoted to the brief analysis and discussion of the experimental results obtained from the preliminary experimental activity aimed at depositing 2D silicon structures by means of PLD and at investigating the obtained system by STM. In the framework of this thesis work, however, the experimental activity regarding the production of two-dimensional silicon exploiting PLD – a route that has never been explored by other researchers – has to be considered only as a side activity.
2D silicon has been attempted onto both Ag(111) and Au(111) substrates, considering that the silver substrate has been used as it is the typical substrate on which silicene is grown, while gold has been investigated since it represents the metallic material usually used in electronic applications – a field where 2D silicon can be very much exploited for the development or improvement of several devices. The deposition process has been carried out by ablating a Si wafer (99.99% pure) by means of a KrF excimer laser and using 100 mJ-energy laser pulses, a laser fluence of 2.5 J/cm^2 and a repetition rate of 1 Hz. The as-deposited system has been observed by means of STM and, subsequently, an annealing treatment is usually performed in order to promote the ordering/crystallization of the deposited material. However, different experimental procedures have been explored and some processing parameters have been varied in order to try to optimize the deposition process and to obtain 2D silicon with a regular and ordered structure – i.e. silicene. In particular, the experimental parameters that have been modified are the number of laser pulses (and hence the amount of ablated and deposited material), the temperature of the annealing treatment and the background pressure in the deposition chamber. More in detail, the number of ablating pulses has been varied between 1 and 30, while the investigated ranges of annealing temperature and deposition pressure are 410 – 630 K and 10^{-9} – 10^{-1} mbar, respectively. All these parameters have been found to have a great influence on the structure and morphology of the deposited material, even though the growth of something similar to silicene has not been achieved.

At first, silicon has been deposited on top of an **Ag(111)** substrate and the STM topographic images are shown in figure 3.29. The PLD process has been first carried out by ablating the Si wafer with one single laser pulse and, then, five additional laser pulses have been employed in order to increase the amount of material deposited onto the silver substrate. In both cases, the deposition process has been performed under UHV conditions (base pressure <10^{-9} mbar). Finally, an annealing treatment at approximately 410 K for 30 min has been carried out, while a thermal treatment at higher temperature (~560 K) leads to the complete desorption of silicon from the substrate surface and to the restoration of the Ag(111) equilibrium surface structure.
As can be seen in figure 3.29(a), the deposition of silicon on Ag(111) (1 laser pulse) leads to the formation of small holes (marked by blue arrows in figure 3.29(a)) on the substrate surface and no deposit seems to be present. After further Si deposition by means of 5 additional ablating pulses, the morphology of the system is that shown in the STM images of figure 3.29(b)-(c): an increase in the number and size of the holes in the substrate is distinctly visible but some silicon clusters can also be found. These clusters are very small and they tend to deposit and grow attached to the holes boundaries (see, for instance, the white circles in figure

3.29(c)). However, the most peculiar characteristic of the Si/Ag(111) system under investigation can be appreciated considering the STM image in figure 3.29(d), where attention is focused on the morphology of the silver step edges. Indeed, after Si deposition has been carried out, the step edges of the Ag(111) substrate appear to be jagged and irregular, while a clean Ag(111) surface is characterized by straight and regular step edges (see the inset of figure 3.29(d)). Finally, the morphology of the same sample after the 410 K annealing treatment is shown in figure 3.29(e). The holes present in the as-deposited sample have disappeared and a larger amount of small silicon clusters seems to be present, with some of them growing along the substrate step edges. As regards the Ag step morphology, both jagged and straight step edges can be observed: the former can be due to the PLD process and to Si nucleation, which modify and disorganize a bit the surface structure of the substrate, while the latter can derive from a relaxation of the stresses – i.e. induced inside the substrate itself by the deposition process - associated to the annealing treatment.

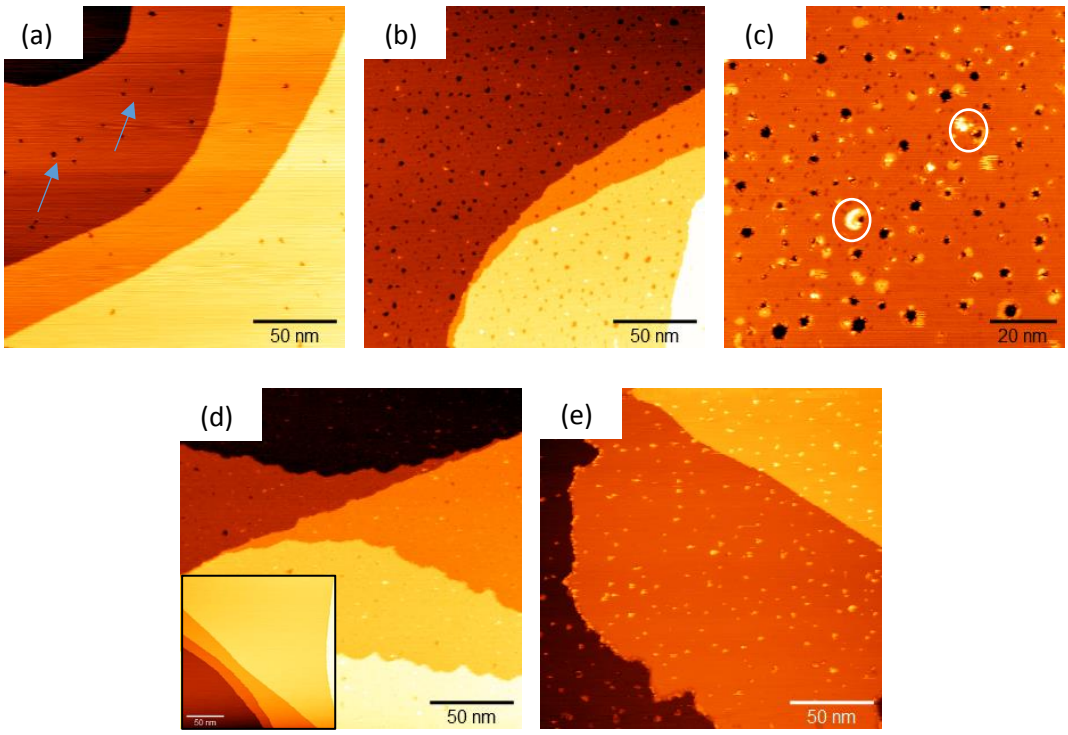

Figure 3.29: (a) STM image (200 nm x 200 nm, V=-0.7 V, I=0.4 nA) of the sample obtained after 1 pulse Si deposition on top of Ag(111). The blue arrows indicate the presence of small holes formed in the substrate. (b) STM image (200 nm x 200 nm, V=1 V, I=0.5 nA) of the sample shown in (a) after an additional silicon deposition consisting in 5 laser pulses. (c) Higher resolution STM image (100 nm x 100 nm, V=0.9 V, I=0.4 nA) of the same system as in (b). The white circles indicate some silicon clusters growing attached to the holes boundaries. (d) STM image (200 nm x 200 nm, V=0.9 V, I=0.4 nA) of the same sample as in (b) in which the presence of jagged and irregular silver step edges can be clearly observed. The inset shows the STM image (200 nm x 200 nm, V=1 V, I=0.5 nA) of a clean Ag(111) surface, in which the step edges are straight and regular, for comparison. (e) STM image (200 nm x 200 nm, V=0.9 V, I=0.45 nA) of the same sample after the 410 K annealing treatment.

In the second part of this preliminary experimental activity, attention has been focused on the deposition of 2D silicon on top of **Au(111)** and on the investigation of the obtained samples.
The first experiment that has been carried out is exactly identical to the one performed in the case of the Si/Ag(111) system, except for the fact that two intermediate annealing temperatures have been explored in order to have a more general overview of the situation. The results of the STM characterization of the obtained sample are displayed in figure 3.30 and figure 3.31.
The situation observed after one single laser pulse on the as-deposited sample is shown in figure 3.30(a). Few very small silicon clusters and holes are formed onto the gold substrate, causing almost no distortion of the regular herringbone reconstruction. The only relevant aspect to be taken into account is the appearance of the jagged step edges instead of the straight ones, a feature that has already been observed in the Si/Ag(111)

system. However, after a further deposition by means of 5 additional ablating pulses, the morphology of the system is strongly modified (figure 3.30(b)). Indeed, a larger amount of small silicon clusters can be found on top of the underlying gold surface, together with several holes featuring an average size of 1 – 2 nm or less and an apparent depth of ~2 Å – i.e. comparable with the height of a gold step (2.3 Å). Another relevant feature of the sample under investigation is the distortion of the Au(111) herringbone reconstruction, which can be clearly seen by considering the brighter lines in figure 3.30(c) and which is a peculiarity of the island growth process on Au(111).

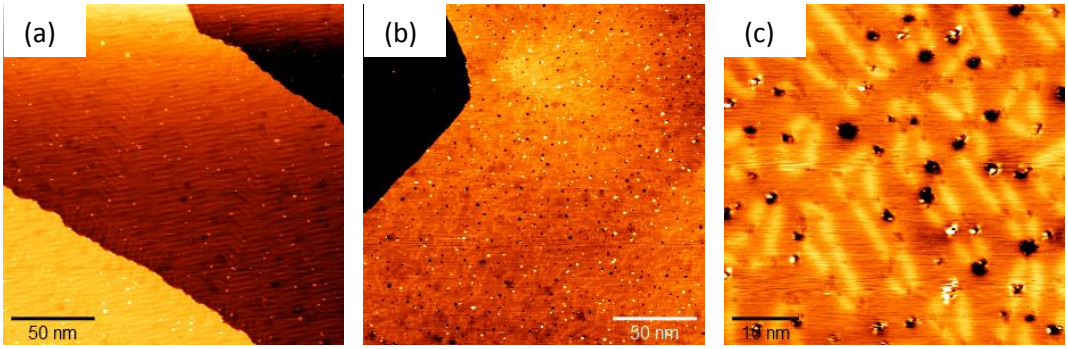

Figure 3.30: (a) STM image (200 nm x 200 nm, V=0.85 V, I=0.5 nA) of the Si/Au(111) system obtained after one single laser pulse. (b) STM image (200 nm x 200 nm, V=0.9 V, I=0.5 nA) of the same sample shown in (a) after further Si deposition by means of 5 additional ablating pulses. (c) Higher magnification STM image (50 nm x 50 nm, V=-0.37 V, I=0.5 nA) of the sample in (b), in which the colour contrast has been properly modified in order to make more visible the ridges of the Au(111) herringbone reconstruction.

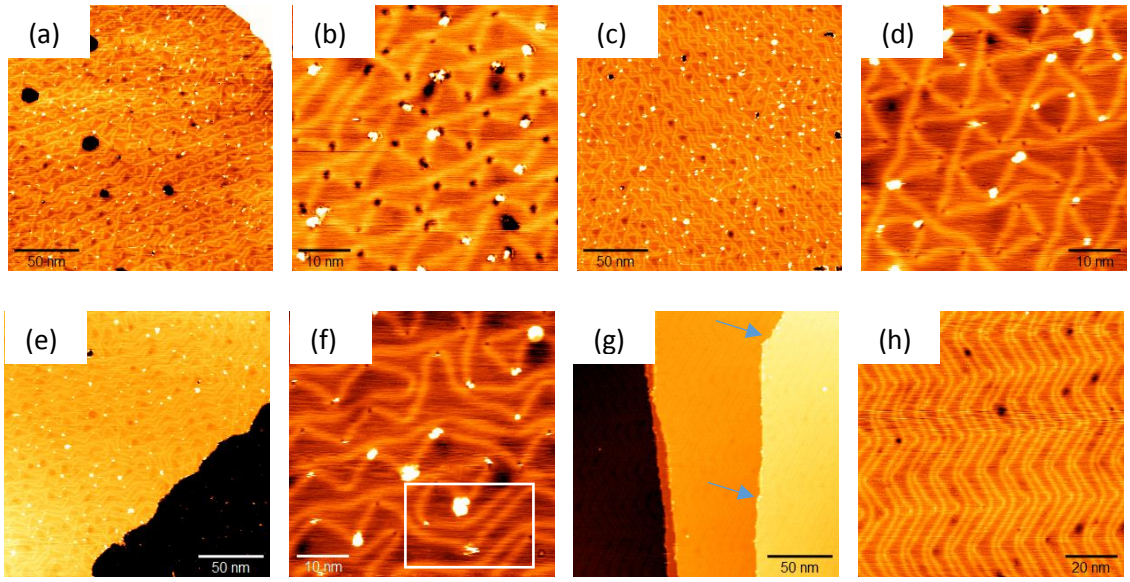

Figure 3.31: (a) STM image (200 nm x 200 nm, V=0.3 V, I=0.5 nA) of the Si/Au(111) sample obtained by using 6 laser pulses and subjected to an annealing treatment at ~410 K for 30 min. (b) Higher magnification STM image (50 nm x 50 nm, V=0.63 V, I=0.5 nA) of the sample in (a). (c) STM image (200 nm x 200 nm, V=0.82 V, I=0.5 nA) of the same Si/Au(111) sample after an annealing treatment at ~460 K for 30 min. (d) Higher magnification STM image (50 nm x 50 nm, V=0.95 V, I=0.5 nA) of the sample in (c). (e) STM image (200 nm x 200 nm, V=1 V, I=0.5 nA) of the same Si/Au(111) sample after an annealing treatment at ~510 K for 30 min. (f) Higher magnification STM image (50 nm x 50 nm, V=1 V, I=0.5 nA) of the sample in (e). The white rectangle highlights the presence of regions in which the Au(111) herringbone reconstruction is quite regular. (g) STM image (200 nm x 200 nm, V=1 V, I=0.5 nA) of the same Si/Au(111) sample after an additional annealing treatment at ~560 K for 30 min. The blue arrows mark the presence of some small Si clusters attached to the Au step edges. (h) Higher magnification STM image (100 nm x 100 nm, V=1 V, I=0.5 nA) of the sample in (g).

Subsequently, the same sample has been subjected to four different annealing treatments at increasingly high temperature and with a duration of 30 min each. The first thermal treatment has been performed at approximately 410 K. The system has been then investigated by STM, through which topographic images of the sample surface have been acquired (figure 3.31(a)-(b)). The Au(111) herringbone reconstruction is highly

distorted, even though a different kind of order and regularity (characterized by the presence of triangular features) can be recognized. Moreover, a quite ordered distribution of small silicon clusters and holes can be found in correspondence of the elbows of the ridges of the distorted herringbone reconstruction (see figure 3.31(b)). Furthermore, some large holes can be identified in the substrate: they are characterized by an average size of 10 nm and an apparent depth of ~2.5 Å (more or less as in the as-deposited sample). The situation remains approximately the same after a 460 K annealing, as can be seen in figure 3.31(c)-(d), with the only appreciable modification being the reduction in the number and size of the holes present in the substrate. This can be related to the fact that the higher annealing temperature can favour the relaxation of the surface (which has been strongly perturbed during silicon nucleation and growth) and hence the closing of the holes.
A further annealing at even higher temperature – i.e. approximately 510 K – promotes the reordering of the surface (as can be seen considering the portion of the substrate in the white rectangle in figure 3.31(f)) and the reduction in the number of clusters present on top of the gold substrate (figure 3.31(e)). Finally, a 30 min annealing treatment at ~560 K results in the almost complete desorption of silicon from the gold surface, except for the presence of very small clusters attached to the Au(111) step edges (see blue arrows in figure 3.31(g)). In addition, the regular herringbone reconstruction is completely restored and only some local defects remain visible on the substrate surface (figure 3.31(h)).

After having investigated the effect of the annealing treatment, attention can be focused on the influence that the number of laser pulses and the background pressure present inside the chamber during the PLD process have on the structure and morphology of the deposited material. In order to carry out this investigation about the effect of the processing parameters modification, the Si/Au(111) system (and not the Si/Ag(111)) has been considered as the presence of the herringbone reconstruction (characteristic of the clean Au(111) surface) can be very helpful, for instance in order to evaluate the degree of perturbation and the out-of-equilibrium condition of the investigated sample.

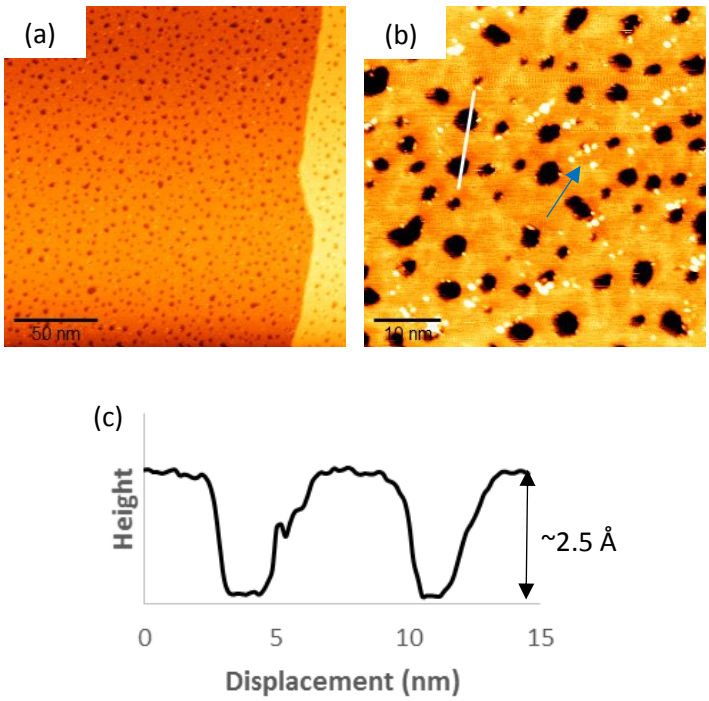

Figure 3.32: (a) STM image (200 nm x 200 nm, V=-1 V, I=0.5 nA) of the as-deposited Si/Au(111) sample obtained by means of 30 laser pulses. (b) Higher magnification STM image (50 nm x 50 nm, V=-1 V, I=0.5 nA) of the sample in (a). The blue arrow indicates the presence of small Si clusters that tend to nucleate and grow on a small portion of the gold surface. (c) Height profile along the white line in (b).

In order to explore the **effect of the number of laser pulses**, and hence of the amount of deposited material, on the structural and morphological features of the Si/Au(111) system and, in particular, in order to see what happens when a larger amount of material is ablated from the target and deposited on the substrate surface, 30 laser pulses have been used. The topography of the sample obtained employing this deposition process and characterized by means of STM in the as-deposited form is shown in figure 3.32(a)-(b). The gold surface is completely covered by small holes, characterized by an average size of the order of 2 – 3 nm and an apparent depth (measured by means of STM) of approximately 2.5 Å (see the line profile in figure 3.32(c)). Besides this, few tiny silicon precipitates can be identified on top of the Au(111) substrate under investigation. Indeed, the presence of these little clusters can be observed in the STM image of figure 3.32(b), where they are found to form and grow either attached to the boundaries of the substrate holes or gathered together in a small region of the gold surface (see, for instance, the blue arrow in figure 3.32(b)). Moreover, it is worth noting that the Au(111) herringbone reconstruction has been completely lost.

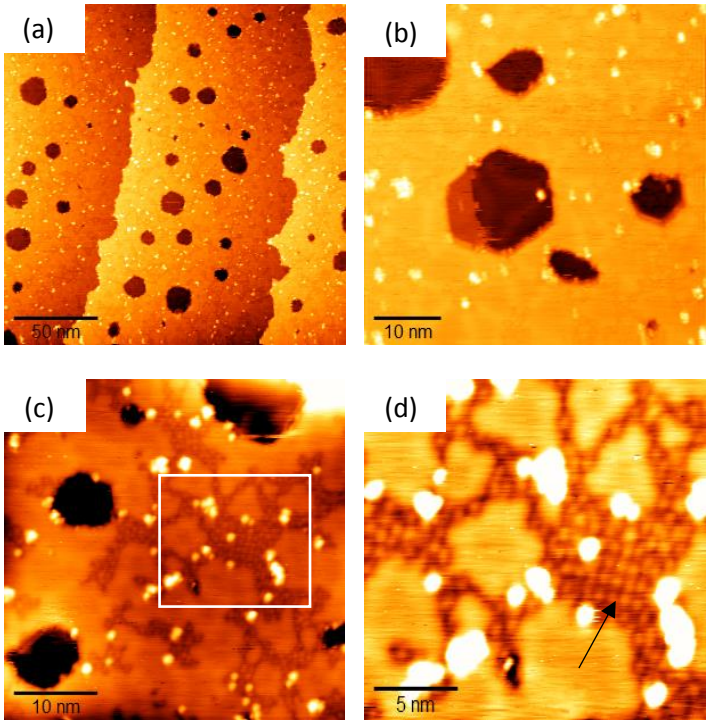

Figure 3.33: STM images of the Si/Au(111) sample obtained by means of 30 laser pulses and subjected to an annealing treatment at a temperature of ~410 K for 30 min. (a) Large-scale STM image (200 nm x 200 nm; V=1 V, I=0.5 nA) showing the morphology of the system. (b) STM image (50 nm x 50 nm, V=0.65 V, I=0.5 nA) in which the structure of the holes present in the substrate is investigated more in detail. (c) STM image (40 nm x 40 nm, V=0.65 V, I=0.4 nA) showing the peculiar morphology of the surface. (d) Higher magnification STM image (20 nm x 20 nm, V=0.9 V, I=0.5 nA) of the region marked by the white square in (c). The black arrow indicates the presence of a strange pattern present in some zones of the Au substrate.

The sample has been then subjected to three subsequent annealing treatments at increasingly high temperature – i.e. ~410 K, ~485 K and ~565 K, respectively. The morphological features of the sample after being treated at approximately 410 K for 30 min are shown in the STM images of figure 3.33. In contrast with the as-deposited situation, the substrate surface is covered by a much larger amount of small Si clusters and features the presence of a much lower number of holes. However, these holes have increased a lot their size (in the order of 10 – 15 nm) with respect to the as-deposited case, even though their apparent depth is ~2.5 Å - i.e. again compatible with the height of a step of the Au(111) surface. In order to investigate more in detail the structure and morphology of the holes, the STM image in figure 3.33(b) can be very helpful. First, it is possible to notice that the holes are characterized by an almost hexagonal shape (even if, sometimes, a more irregular shape can be recognized). Second, the presence of small silicon clusters growing attached to the holes edges can be observed (a feature that was already present in previously investigated samples, such as

in the Si/Au(111) system obtained by 6 laser pulses). Finally, a very peculiar feature can be observed on the gold substrate by acquiring high-resolution STM images (like the ones displayed in figure 3.33(c)-(d)). Indeed, it is possible to recognize a strange pattern that, in some regions of the substrate, is characterized by a certain degree of order and regularity (see the black arrow in figure 3.33(d)). However, we are currently not able to interpret this peculiar structure, its origin is unknown up to now and further experimental research will be necessary to understand the reasons of its formation.

After an additional annealing treatment, which has been performed by maintaining the sample at approximately 485 K for 30 min, the structure and morphology of the system is that shown in figure 3.34(a). The small Si clusters are still present onto the Au(111) surface, even though the most striking feature is again represented by the holes in the substrate: their apparent depth is still in the order of 2 – 2.5 Å but their average size is much larger than before and, in particular, in the order of 25 – 30 nm. Finally, the last annealing treatment (~565 K for 30 min) results in a quite little modification of the system (figure 3.34(b)), the most relevant change being the desorption of a very large amount of Si from the gold surface. Indeed, only a small number of silicon clusters is present and they are mainly concentrated along the step edges (see the white arrows in figure 3.34(b)) or attached to the boundaries of the substrate holes.

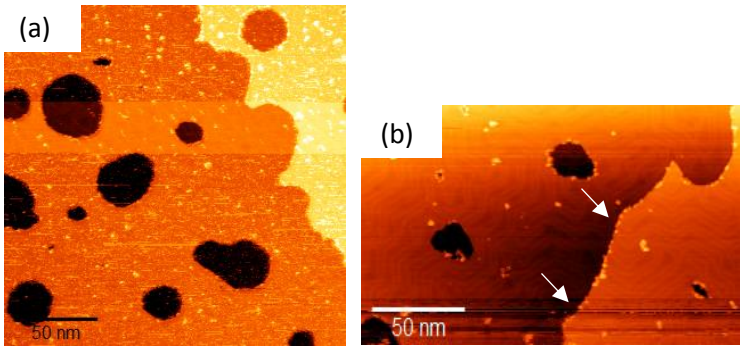

Figure 3.34: (a) STM image (200 nm x 200 nm, V=1 V, I=0.5 nA) of the Si/Au(111) sample obtained by means of 30 laser pulses and subjected to a thermal treatment that has been performed by keeping it at 485 K for 30 min. (b) STM image (200 nm x 100 nm, V=1 V, I=0.4 nA) of the same sample as in (a) after an additional annealing treatment carried out for 30 min at ~565 K. The white arrows mark the presence of very small Si clusters attached to the Au step edges.

In order to conclude this preliminary activity, a last experiment has been performed to investigate the **effect of the background pressure** on the deposition process and, thus, on the structure and morphology of the obtained system. Indeed, it is possible to assume that the formation of the holes in the substrate may be due to the high kinetic energy of the particles ablated from the Si wafer and impinging on the substrate itself. Hence, it may be possible to avoid or reduce the holes formation by decreasing the kinetic energy of the ablated species before they reach the substrate surface and this can be done by increasing the pressure of the background atmosphere present inside the deposition chamber. In particular, instead of performing the PLD process under UHV conditions, an inert gas (Ar) is introduced inside the chamber in order to create an inert atmosphere characterized by a pressure in the order of 10^{-2} – 10^{-1} mbar. In such a way, while travelling from the target to the substrate, the ablated particles suffer several collisions with the Ar atoms present in the deposition chamber and, therefore, their kinetic energy is very much reduced.

When carrying out the deposition process under a background pressure of 5 x 10^{-1} mbar, the STM characterization of the produced system reveals that no silicon has been deposited on top of the substrate and that the Au(111) surface is almost completely clean. This result can be due to the fact that this value of the background pressure is so large that the ablated species are too much slowed down and can not reach the substrate surface. Thus, a lower background pressure was employed and, in particular, 2 x 10^{-2} mbar has been the value of choice. More in detail, the Si deposition by means of PLD has been carried out in this background atmosphere using 30 laser pulses and the obtained system has been investigated by STM in the as-deposited form. As seen in figure 3.35, the performed deposition process leads to the formation of very small but numerous holes in the substrate and to a very large number of silicon clusters. In particular, the

holes feature a lateral size of ~2 nm and an apparent depth in the order of 2 – 2.5 Å, while, as regards the silicon clusters, they are characterized by an irregular shape and are mainly localized in correspondence of the holes edges (figure 3.35(b)).

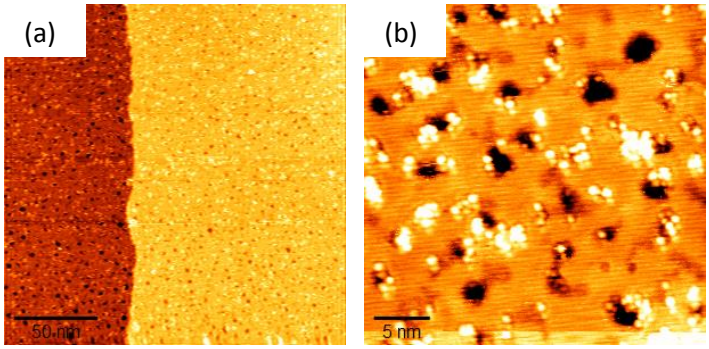

Figure 3.35: (a) STM image (200 nm x 200 nm, V=1 V, I=0.5 nA) of the Si/Au(111) sample obtained by ablating a Si wafer with 30 laser pulses and under an Ar background atmosphere of 2 x 10^{-2} mbar. (b) Higher magnification STM image (30 nm x 30 nm, V=1 V, I=0.5 nA) of the same sample as in (a).

Finally, in order to evaluate the effect of the annealing temperature on the structure and morphology of the obtained system, four subsequent thermal treatments have been carried out for a duration of 30 min each and at increasingly high temperature, ranging from ~410 K to approximately 630 K. After the first annealing treatment at 410 K, the morphology of the system is strongly modified with the formation of fewer and larger holes and the coalescence of the small Si clusters in order to form larger but still irregular structures (see figure 3.36(b)). The holes in the substrate (clearly visible in figure 3.36(a)) are characterized by a lateral size of approximately 10 nm and again an apparent depth of ~2.5 Å. Eventually, a very peculiar feature of the system under investigation is shown in the high-magnification STM image in figure 3.36(c): the ridges of the herringbone reconstruction – i.e. typical of a clean Au(111) surface – are visible (though highly distorted) and they seem to go from one Si cluster to another one.

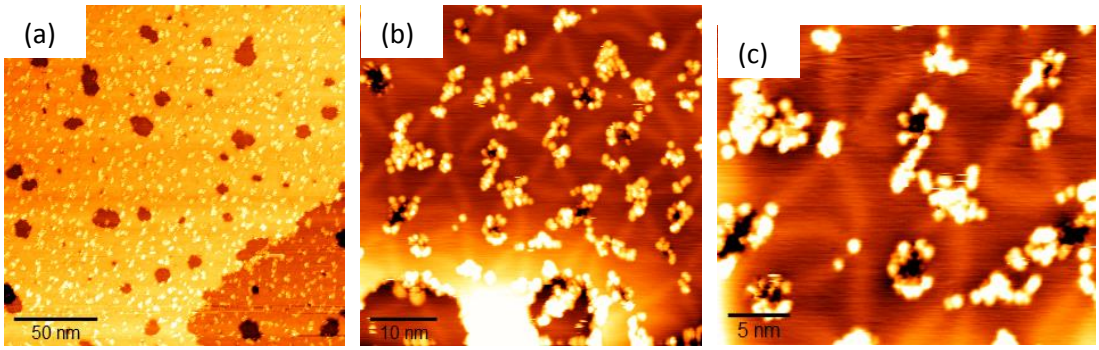

Figure 3.36: STM images of the Si/Au(111) sample under investigation after an annealing treatment carried out by keeping the sample at ~410 K for 30 min. (a) Large-scale STM image (200 nm x 200 nm, V=1 V, I=0.5 nA). (b) Higher-magnification STM image (50 nm x 50 nm, V=1 V, I=0.5 nA) of the same sample as in (a), in which the irregular shape of the Si clusters can be observed. (c) STM image (30 nm x 30 nm, V=0.6 V, I=0.5 nA) of the same sample. The colour contrast has been properly modified in order to be able to observe the ridges of the Au(111) herringbone reconstruction.

The second annealing treatment has been performed by keeping the sample at a temperature of ~485 K for 30 min, resulting in a very slight modification of the surface morphology of the analysed system (see figure 3.37). Indeed, the gold substrate is still covered by a large amount of small and disordered silicon clusters and the only relevant change that can be easily appreciated consists in an increase in the size of the holes (from 10 nm to approximately 15 – 20 nm).

A higher-temperature annealing treatment has been subsequently carried out on the same sample at ~560 K for 30 min and the resulting morphological modifications can be appreciated by considering the STM images in figure 3.38. First, a much lower number of substrate holes seems to be present and this can be due to the

fact that keeping the sample at a rather high temperature for a quite long period of time can favour the relaxation of the surface and, hence, the closing of the holes. Second, larger aggregates are formed because the high temperature of the thermal treatment can increase the mobility of the surface species and can favour their diffusion and, finally, the coalescence of the smaller clusters in order to form bigger structures. Third, the ridges of the Au(111) herringbone reconstruction are now clearly visible and a bit more ordered, a condition that may have been favoured by the high temperature promoting surface relaxation and reordering.

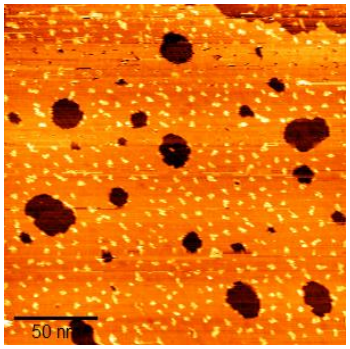

Figure 3.37: STM image (200 nm x 200 nm, V=1 V, I=0.5 nA) of the Si/Au(111) system under investigation after having performed an annealing treatment at ~485 K for 30 min.

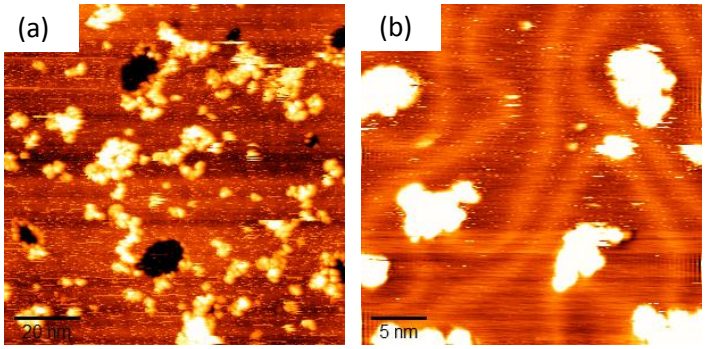

Figure 3.38: STM images of the Si/Au(111) system under investigation after an additional annealing carried out by keeping the sample at approximately 560 K for 30 min. (a) Large-scale STM image (100 nm x 100 nm, V=-1.25 V, I=0.3 nA). (b) Higher magnification STM image (30 nm x 30 nm, V=-1.5 V, I=0.3 nA) of the same sample as in (a).

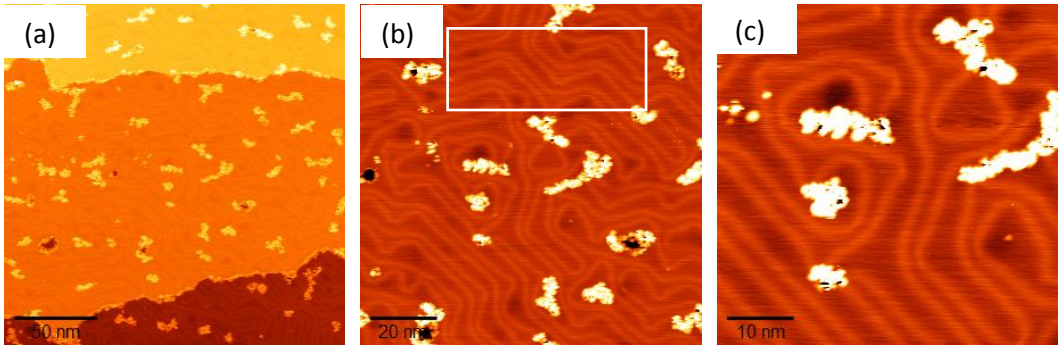

Figure 3.39: STM images (V=-1.4 V, I=0.5 nA) of the Si/Au(111) system under investigation after having performed a further annealing at 630 K for 30 min. (a) STM image (200 nm x 200 nm) showing the overall morphology of the sample. Higher-resolution STM images are shown in (b) (100 nm x 100 nm) and (c) (50 nm x 50 nm), in which the colour contrast has been properly modified in order to highlight both the irregular shape of the deposited Si clusters and the ridges of the Au(111) herringbone reconstruction. The white rectangle in (b) marks the presence of portions of the Au(111) surface where the herringbone reconstruction is quite regular.

Eventually, a last annealing treatment has been performed at 630 K for 30 min in order to evaluate the thermal stability of the deposited material and the modification of the surface morphology and also in order

to verify whether the complete desorption of Si from the Au surface takes place like in the previously discussed experiments. The results of the structural and morphological characterization of the system are shown in figure 3.39. It is possible to notice that disordered silicon clusters are still present on top of the gold substrate, even if the average size of the clusters has increased while the coverage has been strongly reduced (compare, for instance, figures 3.38(a) and 3.39(b)). Another relevant characteristic of the system is related to the Au(111) herringbone reconstruction, which is clearly visible in the STM images of both figure 3.39(b) and figure 3.39(c). In particular, the ridges of the herringbone reconstruction appear to be almost regular in some regions of the gold surface (see, for instance, the white rectangle in figure 3.39(b)), while they remain distorted close to the Si clusters.

To summarize, a first attempt of exploiting pulsed laser deposition in order to deposit 2D silicon on top of Ag(111) and Au(111) has been made. The deposition process has led to the formation of small and irregular silicon clusters and an ordered structure – i.e. similar to that of silicene – has not been observed. Nonetheless, some experiments have been carried out in order to evaluate the influence that some processing parameters and, in particular, the number of laser pulses, the annealing temperature and the background pressure in the deposition chamber can have on the structure and morphology of the deposited material. However, this experimental work is only a preliminary one and further and deeper experimental research about the exploitation of PLD for the deposition of silicon at the two-dimensional scale is needed.

Chapter 4
Conclusions and perspectives

This thesis work has been focused on the study of 2D semiconducting materials and heterostructures by means of STM and STS. In particular, an experimental investigation of MoS_2/ZnO heterostructures, low-dimensional MoS_2 structures and 2D silicon produced by means of PLD has been conducted, with the general aim to study their structural, morphological and electronic properties at the nanometer length scale.

As regards ZnO/MoS_2 heterostructures, the production of in-plane and vertical heterojunctions between these 2D semiconducting materials on top of the Au(111) surface has been studied and particular effort has been devoted to the analysis and interpretation of the structural, morphological and electronic properties featured by the obtained systems.
The desired heterostructures have been fabricated by following two different experimental strategies, both based on the exploitation of PLD as the deposition method, and they have been observed *in situ* by STM. From the analysis of both large-scale and high-resolution STM images, the mixed MoS_2/ZnO structures appear to be formed by the joining of different islands, featuring very different structures and morphologies. However, the employed experimental procedures did not allow to perfectly obtain the 2D phases of the two deposited materials, despite the fact that this is possible when ZnO and MoS_2 are individually grown on Au(111). This can be due to the fact that the synthesis conditions of the two materials are not fully compatible, not only for the PLD process itself but also for the post-deposition annealing treatment, which is usually carried out at a different temperature and in a different atmosphere in the case of ZnO and MoS_2. Nonetheless, one of the explored experimental strategies and, in particular the one based on MoS_2 growth followed by ZnO deposition onto the same substrate, appears to be the most promising one. Indeed, it led to the fabrication of quite ordered MoS_2 islands forming an apparently simple in-plane junction with the ZnO structures present onto the same substrate. On the contrary, the other experimental procedure – i.e. the one relying on the PLD of ZnO and on the subsequent MoS_2 deposition – produces very complex structures in which the different regions can hardly be associated to ZnO or MoS_2.
The electronic properties of the produced systems have been investigated by means of STS measurements. Indeed, the information extrapolated from the interpretation of the acquired I(V) and dI/dV spectra can be helpful in order to identify the single materials (MoS_2 and ZnO) on top of the Au(111) surface and also in order to evaluate the presence of alloys or intermixed compounds, which may form when two different materials are deposited onto the same substrate. In reality, however, the most striking experimental findings resulting from the STS characterization of the samples is related to the role played by the Au substrate in the modification of the electronic properties of the systems. Indeed, independently on the type of structure under investigation, a n-type conductance behaviour and a slight metallization of the overlayer can be observed, considering that both these features are related to the interaction with the underlying Au(111) substrate and to charge transfer phenomena occurring at the overlayer-substrate interface.

2D MoS_2 nanostructures on Ag(111) have been produced following an experimental approach based on PLD and a post-deposition annealing treatment, which is performed at a rather high temperature (~730 K). In order to study the growth of these structures, three different depositions have been carried out by gradually increasing the number of ablating laser pulses in the PLD process – i.e. 10, 30 and 50, respectively – and, hence, the amount of the deposited material and the coverage.
The structure and morphology of the obtained systems have been investigated by STM, which revealed the formation of well-ordered MoS_2 islands featuring a characteristic hexagonal moiré pattern with a ~3.2 nm

periodicity and tending to increase their average size and to coalesce as the number of laser pulses on the MoS_2 target is increased.
The observed nanostructures have been further investigated by means of STS measurements and the acquired spectra reveal the electronic properties of the MoS_2/Ag(111) system. In particular, Ag-supported MoS_2 exhibits an electronic band gap of the order of 2 eV, a non-vanishing DOS around the Fermi level (suggesting a partial metallization of the MoS_2 overlayer) and the pinning of the Fermi level close to the CB edge, thus being a hint of the n-type conductance behaviour of the material.
Finally, AES measurements and Raman and PL spectroscopies have been employed in order to investigate the chemical composition and the electronic, optical and vibrational properties of the samples, thus allowing to conclude that the MoS_2/Ag(111) system is very similar to the MoS_2/Au(111) one.

As far as 2D silicon is concerned, different preparation procedures have been explored, aimed at depositing low-dimensional silicon on top of both Ag(111) and Au(111) substrates by means of PLD. Several deposition conditions have been investigated by changing the number of ablating laser pulses and the pressure of the background atmosphere and, similarly, the effect of the thermal treatment has been analysed by varying the annealing temperature in the 410 K – 630 K range. This experimental activity has been carried out in order to optimize the processing parameters and in order to establish an experimental procedure for the growth of silicene.
The achieved experimental results are not comparable with those obtained by other researchers, who have produced silicene mainly by means of CVD and MBE, even if it is possible to speculate about the growth conditions that have produced the most promising results. Indeed, performing the PLD process by means of 30 laser pulses under a 2 x 10^{-2} mbar Ar pressure and annealing the as-produced sample at ~560 K for 30 min result in the formation of rather large Si structures, even though featuring an irregular morphology.

Future work could be devoted to deepen research objectives addressed only at a preliminary level.
As regards ZnO/MoS_2 heterostructures, different routes have to be explored with the final aim of depositing high-quality or more controlled ZnO/MoS_2 heterostructures. For instance, performing the pulsed laser deposition of the two materials under an inert atmosphere characterized by a quite high background pressure – i.e. in the order of 10^{-4} – 10^{-2} mbar – can be promising since it can be effective in reducing the damage of the first deposited material during the growth of the other one. Furthermore, it may be interesting to deposit a MoS_2 monolayer covering completely (or almost completely) the underlying Au substrate and to grow 2D ZnO on top of the obtained system in such a way to fabricate vertical heterostructures, which are extended over a quite large area (in the order of 1 cm^2).
As far as 2D MoS_2 is concerned, a deep investigation of the structural, morphological and electronic properties of pulsed laser deposited nanostructures on top of Au(111) [44] and Ag(111) has been performed. To conclude this experimental activity, a more detailed study of the different types of surface defects that have been observed on the deposited nanostructures is necessary, also with the aim of comparing the achieved results with those obtained during the experimental activity carried out by Tumino *et al.* [44] on the MoS_2/Au(111) system. However, deposition of low-dimensional MoS_2 on top of other substrates can be further explored in order to exhaustively evaluate the effect of the metallic substrate in modifying the properties of the MoS_2 overlayer. Furthermore, a more detailed investigation of the stability of 2D MoS_2 under ambient conditions can be carried out, even though AES measurements have already revealed that the MoS_2/Ag(111) system is rather inert and stable under some hours air exposure. Nonetheless, it may be interesting to explore the possibility to fabricate a protective capping layer or to develop a specific annealing treatment able to restore the ordered morphology of the material after exposing it to ambient conditions. These procedures may allow the employment of *ex situ* characterization techniques without risking to damage/contaminate the material to be investigated and even the exploitation of this very promising 2D material in future device applications.

Finally, as already mentioned, the fabrication of 2D silicon by means of PLD has been addressed only as a side and preliminary activity. Hence, it would be interesting to deeply explore this novel route for the growth of silicene on top of metallic substrates.

As this thesis work has shown, the experimental approach based on PLD and *in situ* STM characterization is very effective to study the properties of 2D semiconducting materials and heterostructures at the nanoscale. Therefore, among the possible future perspectives, it is worth mentioning the possibility to exploit this experimental procedure for the investigation of other materials at the two-dimensional limit. Indeed, the PLD process may offer the opportunity to fabricate high-quality 2D systems suitable for the research activity but also the possibility to synthesize 2D materials and heterostructures on rather large areas – i.e. in the order of cm^2 – and, hence, to use them for the fabrication of real and working devices. Then, *in situ* STM and STS measurements allow to investigate the nanoscale structural and electronic properties of the produced materials/heterostructures, thus providing an experimental way to probe unprecedented and possibly tunable electronic properties.

Bibliography

[1] Soldano C, Mahmood A, Dujardin E. Production, properties and potential of graphene. Carbon. 2010;48(8):2127-2150.

[2] Pacchioni G. Two-Dimensional Oxides: Multifunctional Materials for Advanced Technologies. Chemistry - A European Journal. 2012;18(33):10144-10158.

[3] Wang Q, Kalantar Zadeh K, Kis A, Coleman J, Strano M. Electronics and optoelectronics of two-dimensional transition metal dichalcogenides. Nature Nanotechnology. 2012;7(11):699-712.

[4] Butler S, Hollen S, Cao L, Cui Y, Gupta J, Gutiérrez H, et al. Progress, Challenges, and Opportunities in Two-Dimensional Materials Beyond Graphene. ACS Nano. 2013;7(4):2898-2926.

[5] Grazianetti C, Cinquanta E, Molle A. Two-dimensional silicon: the advent of silicene. 2D Materials. 2016;3(1):012001.

[6] Mak K, Lee C, Hone J, Shan J, Heinz T. Atomically Thin MoS_2: A New Direct-Gap Semiconductor. Phys Rev Lett. 2010;105(13):136805.

[7] Splendiani A, Sun L, Zhang Y, Li T, Kim J, Chim C, et al. Emerging Photoluminescence in Monolayer MoS_2. Nano Letters. 2010;10(4):1271-1275.

[8] Radisavljevic B, Radenovic A, Brivio J, Giacometti V, Kis A. Single-layer MoS_2 transistors. Nature Nanotechnology. 2011;6(3):147-150.

[9] Chianelli R, Siadati M, De la Rosa M, Berhault G, Wilcoxon J, et al. Catalytic Properties of Single Layers of Transition Metal Sulfide Catalytic Materials. Catalysis reviews. Science and engineering. 2006;48(1):1-41.

[10] Jaramillo T. Identification of Active Edge Sites for Electrochemical H_2 Evolution from MoS_2 Nanocatalysts. Science. 2007;317(5834):100-102.

[11] Freeman C, Claeyssens F, Allan N, Harding J. Graphitic Nanofilms as Precursors to Wurtzite Films: Theory. Phys Rev Lett. 2006;96(6):066102.

[12] Kang J, Zhang Y, Wen Y, Zheng J, Zhu Z. First-principles study on the structural and electronic properties of ultrathin ZnO nanofilms. Physics letters A. 2010;374(8):1054-1058.

[13] Takeda K, Shiraishi K. Theoretical possibility of stage corrugation in Si and Ge analogs of graphite. Physical Review B: Condensed Matter. 1994;50(20):14916-14922.

[14] Akturk E, Sahin H, Cahangirov S, Topsakal M, et al. Two- and One-Dimensional Honeycomb Structures of Silicon and Germanium. Phys Rev Lett. 2009;102(23):236804.

[15] Feng B, Ding Z, Meng S, Yao Y, He X, et al. Evidence of Silicene in Honeycomb Structures of Silicon on Ag(111). Nano Letters. 2012;12(7):3507-3511.

[16] Mannix A, Kiraly B, Fisher B, Hersam M, Guisinger N. Silicon Growth at the Two-Dimensional Limit on Ag(111). ACS Nano. 2014;8(7):7538-7547.

[17] Gao J, Zhao J. Initial geometries, interaction mechanism and high stability of silicene on Ag(111) surface. Scientific Reports. 2012;2(1):861.

[18] Vali M, Dideban D, Moezi N. Silicene field effect transistor with high on/off current ratio and good current saturation. Journal of Computational Electronics. 2016;15(1):138-143.

[19] Geim AK, Grigorieva IV. Van der Waals heterostructures. Nature. 2013;499(7459):419-425.

[20] Li M, Chen C, Shi Y, Li L. Heterostructures based on two-dimensional layered materials and their potential applications. Materials today (Kidlington). 2016;19(6):322-335.

[21] Gong Y, Lin J, Wang X, Shi G, Lei S, Lin Z, et al. Vertical and in-plane heterostructures from WS_2/MoS_2 monolayers. Nature Materials. 2014;13(12):1135-1142.

[22] Yang Z, Hao J. Progress in pulsed laser deposited two-dimensional layered materials for device applications. Journal of Materials Chemistry C: Materials for optical and electronic devices. 2016;4:8859-8878.

[23] Loh TAJ, Chua DHC, Wee ATS. One-step Synthesis of Few-layer WS_2 by Pulsed Laser Deposition. Scientific Reports. 2016;5(1):18116.

[24] Glavin N, Jespersen M, Check M, Hu J, Hilton A, et al. Synthesis of few-layer, large area hexagonal-boron nitride by pulsed laser deposition. Thin Solid Films. 2014;572(C):245-250.

[25] Serrao C, Diamond A, Hsu S, You L, Gadgil S, Clarkson J, et al. Highly crystalline MoS_2 thin films grown by pulsed laser deposition. Appl Phys Lett. 2015;106(5):052101.

[26] Siegel G, Venkata-Subbaiah YP, Prestgard M, Tiwari A. Growth of centimeter-scale atomically thin MoS_2 films by pulsed laser deposition. APL Materials. 2015;3(5):056103.

[27] Serna M, Yoo S, Moreno S, Xi Y, Oviedo J, Choi H, et al. Large-Area Deposition of MoS_2 by Pulsed Laser Deposition with In Situ Thickness Control. ACS Nano. 2016;10(6):6054-6061.

[28] Lee C, Yan H, Brus L, Heinz T, Hone J, Ryu S. Anomalous Lattice Vibrations of Single- and Few-Layer MoS_2. ACS Nano. 2010;4(5):2695-2700.

[29] Loh TAJ, Chua DHC. Growth Mechanism of Pulsed Laser Fabricated Few-Layer MoS_2 on Metal Substrates. ACS Applied Materials and Interfaces. 2014;6(18):15966-15971.

[30] Sørensen S, Füchtbauer H, Tuxen A, Walton A, Lauritsen J. Structure and Electronic Properties of In Situ Synthesized Single-Layer MoS_2 on a Gold Surface. ACS Nano. 2014;8(7):6788-6796.

[31] Choopun S, Vispute RD, Noch W, Balsamo A, Sharma RP, Venkatesan T, et al. Oxygen pressure-tuned epitaxy and optoelectronic properties of laser-deposited ZnO films on sapphire. Appl Phys Lett. 1999;75(25):3947-3949.

[32] Claeyssens F, Freeman C, Allan N, Sun Y, Ashfold MNR, et al. Growth of ZnO thin films - experiment and theory. Journal of materials chemistry. 2005;15(1):139-148.

[33] Tusche C, Meyerheim HL, Kirschner J. Observation of Depolarized ZnO(0001) Monolayers: Formation of Unreconstructed Planar Sheets. Phys Rev Lett. 2007;99(2):026102.

[34] Helveg S, Lauritsen JV, Lægsgaard E, Stensgaard I, Nørskov JK, Clausen BS, et al. Atomic-Scale Structure of Single-Layer MoS_2 Nanoclusters. Phys Rev Lett. 2000;84(5):951-954.

[35] Takeuchi N, Chan CT, Ho KM. Au(111): A theoretical study of the surface reconstruction and the surface electronic structure. Physical Review B: Condensed Matter. 1991;43(17):13899-13906.

[36] Yasuda S, Takahashi R, Osaka R, Kumagai R, Miyata Y, et al. Out-of-Plane Strain Induced in a Moirè Superstructure of Monolayer MoS_2 and $MoSe_2$ on Au(111). Small. 2017;13(31):1700748.

[37] Bruix A, Miwa J, Hauptmann N, Wegner D, Ulstrup S, Grønborg S, et al. Single-layer MoS_2 on Au(111): Band gap renormalization and substrate interaction. Physical Review B. 2016;93(16):165422.

[38] Grønborg S, Ulstrup S, Bianchi M, Dendzik M, Sanders C, Lauritsen J, et al. Synthesis of Epitaxial Single-Layer MoS_2 on Au(111). Langmuir. 2015;31(35):9700-9706.

[39] Ta HQ, Zhao L, Pohl D, Pang J, Trzebicka B, Rellinghaus B, et al. Graphene-Like ZnO: A Mini Review. Crystals. 2016;6(8):100.

[40] Shiotari A, Liu B, Jaekel S, Grill L, Shaikhutdinov S, Freund H, et al. Local Characterization of Ultrathin ZnO Layers on Ag(111) by Scanning Tunneling Microscopy and Atomic Force Microscopy. The Journal of Physical Chemistry C. 2014;118(47):27428-27435.

[41] Stavale F, Pascua L, Nilius N, Freund H. Morphology and Luminescence of ZnO Films Grown on a Au(111) Support. The Journal of Physical Chemistry C. 2013;117(20):10552-10557.

[42] Deng X, Yao K, Sun K, Li W, Lee J, Matranga C. Growth of Single- and Bilayer ZnO on Au(111) and Interaction with Copper. The Journal of Physical Chemistry C. 2013;117(21):11211-11218.

[43] Lee J, Sorescu D, Deng X. Tunable Lattice Constant and Band Gap of Single- and Few-Layer ZnO. The Journal of Physical Chemistry Letters. 2016;7(7):1335-1340.

[44] Tumino F, Casari CS, Passoni M, Russo V, Li Bassi A. Growth of MoS_2 on Au(111): from Nanosized Crystals to Large-Area Single-Layer Films. Nanoscale Advances. 2018.

[45] Tumino F, Casari CS, Passoni M, Bottani CE, Li Bassi A. Pulsed laser deposition of two-dimensional ZnO nanocrystals on Au(111): growth, surface structure and electronic properties. Nanotechnology. 2016;27(47):475703.

[46] Li Bassi A, Casari CS. Pulsed laser deposition of nanostructured oxides: from clusters to functional films. Advances in Laser and Optic Research. 2011;7:65-100.

[47] Willmott PR, Huber JR. Pulsed laser vaporization and deposition. Reviews of Modern Physics. 2000;72(1):315-328.

[48] Voigtlander B. *Scanning Probe Microscopy*. Springer. 2015.

[49] Bardeen J. Tunnelling from a Many-Particle Point of View. Phys Rev Lett. 1961;6(2):57-59.

[50] Tersoff J, Hamann DR. Theory and Application for the Scanning Tunneling Microscope. Phys Rev Lett. 1983;50(25):1998-2001.

[51] Chen CJ. *Introduction to Scanning Tunneling Microscopy*. Oxford University Press, Inc. 1993.

[52] Stroscio J, Feenstra RM, Fein AP. Electronic Structure of the Si(111)2 × 1 Surface by Scanning Tunneling Microscopy. Phys Rev Lett. 1986;57(20):2579-2582.

[53] Ukraintsev V. Data evaluation technique for electron-tunneling spectroscopy. Physical Review B: Condensed Matter. 1996;53(16):11176-11185.

[54] Koslowski B, Dietrich C, Tschetschetkin A, Ziemann P. Evaluation of scanning tunneling spectroscopy data: Approaching a quantitative determination of the electronic density of states. Physical Review B: Condensed Matter and Material Physics. 2007;75(3):035421.

[55] Vickerman JC, Gilmore IS. *Surface Analysis: The Principal Techniques*. John Wiley & Sons, Ltd. 2009.

[56] Brundle CR, Evans CA, Wilson S. *Encyclopedia of Materials Characterization - Surfaces, Interfaces, Thin Films*. Butterworth-Heinemann. 2013.

[57] Yu M, Woodruff DP, Satterley C, Jones R, Dhanak VR. Structural Investigation of the Interaction of Molecular Sulfur with Ag(111). The Journal of Physical Chemistry C. 2007;111(7):3152-3162.

[58] Hövel H, Grimm B, Reihl B. Modification of the Shockley-type surface state on Ag(111) by an adsorbed xenon layer. Surf Sci. 2001;477(1):43-49.

[59] Reinert F, Nicolay G, Schmidt S, Ehm D, Hüfner S. Direct measurements of the L-gap surface states on the (111) face of noble metals by photoelectron spectroscopy. Physical Review B: Condensed Matter. 2001;63(11):115415.

[60] Gong C, Colombo L, Wallace R, Cho K. The Unusual Mechanism of Partial Fermi Level Pinning at Metal-MoS_2 Interfaces. Nano Lett. 2014;14(4):1714-1720.

[61] Morales Garcia A, Kavan L, Kalbac M, Peña Álvarez M, Del Corro E, et al. Single Layer Molybdenum Disulfide under Direct Out-of-Plane Compression: Low-Stress Band-Gap Engineering. Nano Lett. 2015;15(5):3139-3146.

[62] Chakraborty B, Bera A, Muthu DVS, Bhowmick S, Waghmare UV, et al. Symmetry-dependent phonon renormalization in monolayer MoS_2 transistor. Physical Review B: Condensed Matter and Material Physics. 2012;85(16):161403.

[63] Rice C, Young RJ, Zan R, Bangert U, Wolverson D, Georgiou T, et al. Raman-scattering measurements and first-principles calculations of strain-induced phonon shifts in monolayer MoS_2. Physical Review B: Condensed Matter and Material Physics. 2013;87(8):081307.

[64] Conley H, Wang B, Ziegler J, Haglund R, Pantelides S, Bolotin K. Bandgap Engineering of Strained Monolayer and Bilayer MoS_2. Nano Letters. 2013;13(8):3626-3630.

[65] Buscema M, Steele G, van der Zant HSJ, Castellanos Gomez A. The effect of the substrate on the Raman and photoluminescence emission of single-layer MoS_2. Nano Research. 2014;7(4):561-571.

[66] Shi J, Ma D, Han G, Ji Q, Gao T, Sun J, et al. Controllable Growth and Transfer of Monolayer MoS_2 on Au Foils and Its Potential Application in Hydrogen Evolution Reaction. ACS Nano. 2014;8(10):10196-10204.